

Diffusion of Particles in Structureless Media

Fumiaki Nakai

Abstract

Diffusion of a particle is ubiquitous and has been investigated for over one hundred years. One of the well-known descriptions of the diffusion phenomenon is the Fick's law, which expresses the time evolution of the concentration field of the particles at a macroscopic scale. On the microscopic scale, diffusion can be regarded as the random motion of a particle, which is a consequence of the collisions with the fluid molecules. For a simple case where the particle exhibits normal diffusion with the Gaussian displacement distribution, the Brownian motion is described using the Langevin equation. These simple descriptions are not always valid for complex systems like glassy media, polymeric systems, and even gas systems. To express such a complex diffusion, various theoretical endeavors have been conducted, e.g., generalized Langevin equation for some viscoelastic materials, the Enskog theory for gases and liquids, mode-coupling theory for liquids and glassy media, or phenomenological descriptions like the Rouse, Zimm, and Doi-Edwards models for polymeric systems. Although these frameworks are sophisticated and useful, some systems cannot be described using the conventional frameworks. In the structureless media where the constituent particles are uniformly distributed in space, the dynamics of a constituent particle can exhibit intriguing behaviors; the constituent particle exhibits anomalous and/or non-Gaussian diffusion even in its simple nature. This dissertation numerically and theoretically investigates the dynamics of particles in simple structureless media; the constituent particles are spherical (or point masses) and distributed uniformly in space. The effects of basic parameters such as particle mass and shape on diffusion phenomena are explored. Chapters 2 to 5 correspond to the works by Nakai [1–4], that have been published, as follows:

Chapter 2 [F. Nakai, Y. Masubuchi and T. Uneyama, “Short time dynamics of a particle in an ideal gas,” *Phys. Rev. E.* **102**, 032104 (2020)]. The dynamics of a spherical particle (target particle) in a simple gas media consisting of point masses are examined using event-driven type simulations. In this gas system, the structure of the media is always an

ideal gas in any situation. The dynamics of the target particle is calculated with various target particle masses and number densities of the ideal gas. Even in such a simple nature, the target particle exhibits non-Gaussian diffusion when the target particle is lighter than that of the ideal gas particle. Further, the lightweight particle shows non-Gaussian and anomalous diffusion, which is often observed in some complex media like glass-forming liquids or polymeric systems, when the number density of gas particles is large. To clarify the origin of the observed anomalous and non-Gaussian diffusion, this chapter analyzes the dynamics of the particle, focusing on the collisions between the target and gas particles. The anomalous and non-Gaussian diffusion originates from the repeated collisions of the target particle against the same gas particle.

Chapter 3 [F. Nakai, Y. Masubuchi, Y. Doi, T. Ishida, and T. Uneyama, “Fluctuating diffusivity emerges even in binary gas mixtures,” *Phys. Rev. E* **107**, 014605 (2023)].

To clarify the non-Gaussian diffusion of a lightweight particle immersed in a dilute gas, which is observed in Chapter 2, a stochastic simulation is constructed. This simulation requires two inputs. One is the collision statistics, which details when and where the target particle collides with a gas particle; these statistics are derived from classical gas kinetics. The other input is the rule of the velocity change of the lightweight particle at the collision, which is obtained from the conservation of the energy and momentum between the two colliding particles. Using the constructed simulations, the dynamics of a lightweight particle in a dilute gas is computed with various mass ratios. It is found that, even in the simple gas system, the lightweight particle exhibits Brownian yet non-Gaussian diffusion; the mean square displacement is linear against time, while the displacement distribution obeys the non-Gaussian statistics. The Brownian yet non-Gaussian diffusion in the current system is attributed to the temporal fluctuation of the diffusion coefficient, the so-called “fluctuating diffusivity” that the lightweight particle experiences. The origin of the observed fluctuating diffusivity is clarified: the separation of the relaxation timescales for the velocity direction and speed of the lightweight particle. Namely, in the short timescale where the speed remains unchanged, the lightweight particle diffuses by changing the velocity direction. The speed of the lightweight particle fluctuates in the longer timescale, and the diffusion coefficient of the lightweight particle also fluctuates along with the speed.

Chapter 4 [F. Nakai and T. Uneyama, “Brownian yet non-Gaussian diffusion of a lightweight particle in heavy gas: Lorentz-gas-based analysis,” *Phys. Rev. E* **108**, 044129 (2023)]. The theoretical analysis is performed to represent the Brownian yet non-

Gaussian diffusion observed in a lighter particle immersed in the heavier gas particles. The lighter particle in heavier gas particles has been traditionally modeled by the Lorentz gas, comprised of a single mobile particle in fixed spherical obstacles, and this model is utilized for the current purpose. The time-correlation functions, such as a mean square displacement and non-Gaussian parameter for the Lorentz gas, are analytically calculated using the theoretical framework of the point process. These results do not exhibit the Brownian yet non-Gaussian diffusion since the speed of the mobile particle in the Lorentz gas remains unchanged. To incorporate the effect of the change in the speed of the lightweight particle over a long timescale, the ensemble averages for the time-correlation functions are analytically calculated. The averaged results successfully demonstrate the Brownian yet non-Gaussian diffusion and quantitatively agree with the data for the binary gas mixture without any *ad hoc* parameters.

Chapter 5 [F. Nakai, M. Kröger, T. Ishida, T. Uneyama, Y. Doi, and Y. Msubuchi, “Increase in rod diffusivity emerges even in Markovian nature,” *Phys. Rev. E* **107**, 044604 (2023)]. The dynamics of a rod suspended in a simple media composed of fixed spherical obstacles are numerically examined. To this end, a stochastic simulation assuming the Markovian process, which requires the collision statistics and rule of the velocity change, is constructed. These inputs are obtained from gas kinetics and classical mechanics, respectively. The dynamics of the rod is analyzed with various rod lengths and number densities of the obstacles, and the diffusion coefficient is calculated. In this system, the diffusion coefficient of the rod exhibits upturn behavior with increasing the obstacle number density when the aspect ratio of the rod is sufficiently large, even in the Markovian process. Thanks to the Markovian nature, the power exponents of the diffusion coefficient for dilute, intermediate, and concentrated density regimes are straightforwardly understood based on the collision frequency and angular velocity.

In conclusion, this dissertation investigated the dynamics of spherical and rod-shaped particles in simple structureless media where the structure of the system is just an ideal gas. Even in such a simple environment, some intriguing phenomena appear. For a spherical particle in point masses, anomalous and non-Gaussian diffusion caused by repeated collisions with the same gas particle can appear. Even for dilute cases, the numerical simulations and theoretical analysis clarified that lightweight particles exhibit non-Gaussian diffusion over the time scale with the normal diffusion, originating from the long-time persistence of the speed of the lightweight particles. For a rod-shaped particle, the counter-intuitive increase in diffusion coefficient against the obstacle density

emerges, which can be explained via the collision frequency and angular velocity. The above-mentioned observation of the interesting phenomena will not be limited to the simple structureless media investigated in this dissertation. This dissertation will provide fresh insights into the study of the complex diffusion phenomena exhibited by lightweight or long particles.

Nomenclature

variables	meanings
β	inverse temperature
\mathcal{V}	system volume
t	time
Δt	time lag
T	observation time
$t_{c,i}$	time at i th collision
τ	relaxation time
σ	radius of particle
d	diameter of particle
M	mass of target particle
m	mass of fluid particle
m_i	mass of i th fluid particle
m_t	total mass
m_r	reduced mass
N	number of fluid particles
ρ	number density of fluid particle
n	number of collisions for target particle
\mathbf{R}	position of target particle
$\mathbf{R}_{c,i}$	position of target particle at i th collision
$\Delta \mathbf{R}(\Delta t)$	displacement at time lag Δt
\mathbf{V}	velocity of target particle
$\mathbf{V}_{c,i}$	velocity of target particle after i th collision
\mathbf{P}	momentum of target particle
Ω	angular velocity of target particle

$\Omega_{c,i}$	angular velocity of target particle after i th collision
\mathbf{U}	direction vector of rod
$\mathbf{U}_{c,i}$	direction vector of rod after i th collision
\mathbf{r}	position of fluid
\mathbf{v}	velocity of fluid
\mathbf{v}_i	velocity of i th particle
\mathbf{v}_{rel}	relative velocity
\mathbf{v}_{cent}	center of mass velocity
$\mathbf{v}_{c,i}$	velocity of colliding particle at i th collision
\mathbf{p}_i	momentum of i th fluid particle
$\mathbf{u}_{c,i}$	direction vector at i th collision
\mathbf{F}_{ij}	force between i th and j th particles
G_s	self-part of van-Hove correlation function
$f(x; y)$	distribution function of variable x for given parameter y
$P(x; y)$	probability density of x for given parameter y
$\Psi(x; y)$	cumulative probability of variable τ for given y
$P_{\text{eq}}(x)$	equilibrium distribution of variable x
L	length of major axis of rod
L_e	effective length of rod defined as $L + 2\sigma$
\mathbf{I}	inertia tensor of rod
$\langle x \rangle$	ensemble average of x
$\nu(x)$	collision frequency with x
$\bar{\nu}$	total collision frequency
λ	free path
Δt_f	free time
ω	solid angle
a	differential cross section
L_b	box length
γ_n	correlation function before and after n collisions
\mathbf{k}	wave vector
s	complex frequency
α	non-Gaussian parameter
D	translational diffusion coefficient

D_{rot}	rotational diffusion coefficient
$\delta(\Delta t, T)$	time-averaged MSD
ζ	friction coefficient
ξ	stochastic noise
\mathbf{n}	normal vector
z	collision coordinate along major axis of rod
$\hat{\mathbf{x}}, \hat{\mathbf{y}}, \hat{\mathbf{z}}$	unit vectors of cartesian coordinate along x , y , and z axes, respectively
ϕ and θ	angles
H	hamiltonian
E_U	potential energy
E	total energy
ϵ	energy unit

Contents

1	General Introduction	11
1.1	Diffusion	11
1.2	BBGKY Hierarchy	13
1.3	Generalized Langevin Equation	15
1.4	Structure-Based Analyses	16
1.5	Phenomenological Models without Relying on Structures	18
1.6	Dynamics in Structureless Media	19
1.7	Subject of Dissertation	21
2	Non-Gaussian Diffusion of Particle in Ideal Gas	23
2.1	Introduction	23
2.2	Method	24
2.2.1	System Setting	24
2.2.2	Simulation Protocol	25
2.3	Results	26
2.3.1	Time Correlation Functions	26
2.3.2	Focusing on Collision Dynamics	31
2.4	Discussion	34
2.5	Summary	35
2.A	Theoretical Analysis for γ_1	35
3	Fluctuating Diffusivity of Particle in Gas Mixtures: Numerical Study	38
3.1	Introduction	38
3.2	Method	40
3.2.1	System Setting	40

<i>CONTENTS</i>	9
3.2.2 Collision Statistics	41
3.2.3 Kinetic Monte Carlo Method	42
3.3 Results	44
3.3.1 Fluctuating Diffusivity in Gas	44
3.3.2 Origin of Fluctuating Diffusivity	52
3.4 Discussion	55
3.5 Summary	56
3.A Additional Simulation Data	56
4 Fluctuating Diffusivity of Particle in Gas Mixtures: Theoretical Study	60
4.1 Introduction	60
4.2 Theoretical Analyses	62
4.2.1 Model Setting	62
4.2.2 Correlation Function of Lorentz Gas	63
4.2.3 Correlation Functions of Binary-Gas Mixture	68
4.3 Discussion	72
4.4 Summary	73
5 Increase in Diffusivity of Rod in Obstacles	74
5.1 Introduction	74
5.2 Simulation Method	76
5.2.1 System Setting	76
5.2.2 Simulation Protocol	77
5.3 Results	78
5.3.1 Increase in Diffusivity	78
5.3.2 Comparison with Molecular Dynamics Simulation	82
5.4 Discussion	83
5.5 Summary	85
5.A Kinetic Monte Carlo Method	86
5.A.1 Overview of KMC Simulation	86
5.A.2 Collision Statistics	87
5.A.3 Protocol of KMC Simulation	89
5.B Empirical Expression for Diffusion Coefficient	92
5.C Additional KMC Simulation Data	93

<i>CONTENTS</i>	10
5.D Protocol of Simulation	95
6 Conclusion	99
Acknowledgements	100
References	104

Chapter 1

General Introduction

Abstract

In this chapter, the diffusion phenomena and their descriptions are presented. The diffusion equation and the Langevin equation are introduced as basic models. The discussion then moves to the BBGKY hierarchy, serving as a formal theoretical framework, while it is generally unsolvable. The chapter progresses to discuss frameworks beneficial for analyzing complex dynamics. The generalized Langevin equation is presented as a model which describes a particle in viscoelastic media. Subsequently, sophisticated models based on liquid structures and phenomenological models without relying on structures are explained. Afterward, unresolved diffusion phenomena that change qualitatively in response to variations in a system parameter without a qualitative change in the structure are highlighted, and the subject of this dissertation is presented.

1.1 Diffusion

Small objects, such as molecules and/or nano-particles, situated in a fluid exhibit random motions as if they were alive. This motion was first discovered by Robert Brown [5] in 1827. Subsequent theories by Einstein [6,7] and experiments by Perrin [8] revealed that the random motion of particles originates from collisions with solvent molecules. This discovery served as proof of the existence of molecules. The random motions of molecules/nano-particles are universal phenomena at small length scales, transcending the realm of physics into important areas of chemistry, engineering, and biology. The statistics of random motion strongly depend on the nature of the molecules/nano-particles and the solvent, which leads to diverse diffusion phenomena like gas [9–12], polymer

[13–15], liquid crystals [14, 16], glass [14, 17], and biological systems [18]. Understanding the physics of such diffusion at microscopic scales has been crucial in diverse fields.

Macroscopically, random motions of particles can be observed as the time development of the distribution function of the particle, $f(\mathbf{R}; t)$, with \mathbf{R} and t being the position of the particle and time. Fick's second law roughly predicts the time-development of $f(\mathbf{R}; t)$ as follows:

$$\frac{\partial f(\mathbf{R}; t)}{\partial t} = D \frac{\partial^2 f(\mathbf{R}; t)}{\partial \mathbf{R}^2} \quad (1.1)$$

Equation (1.1) expresses the simplest diffusion process. Microscopically, this time-development of the distribution function is attributed to random motions of particles. If a single particle (hereafter called a target particle) is traced, the motion is phenomenologically described using the Langevin equation [13, 19–21] for simple media, expressed as follows:

$$M \frac{d^2 \mathbf{R}(t)}{dt^2} = -\zeta \frac{d\mathbf{R}(t)}{dt} + \boldsymbol{\xi}(t), \quad (1.2)$$

where ζ is the friction coefficient, and $\boldsymbol{\xi}$ denotes the Gaussian white noise. To satisfy the fluctuation-dissipation theorem, the first and second moments of $\boldsymbol{\xi}$ are given as follows:

$$\langle \boldsymbol{\xi}(t) \rangle = \mathbf{0} \quad (1.3)$$

$$\langle \boldsymbol{\xi}(t) \boldsymbol{\xi}(t') \rangle = 2\beta^{-1} \zeta \delta(t - t') \mathbf{1}, \quad (1.4)$$

where β is the inverse temperature, $\langle x \rangle$ the ensemble average of a variable x , and $\mathbf{1}$ the unit tensor. The random motion of the particle can be characterized using statistical time-correlation functions. When the dynamics of the particle is described using Equation (1.2), the mean square displacement, defined as $\langle \Delta \mathbf{R}^2(\Delta t) \rangle$ with $\Delta \mathbf{R}(\Delta t)$ being the particle displacement at time-lag Δt , becomes linear against time, except for the short timescale where the particle motion is ballistic, as follows:

$$\langle \Delta \mathbf{R}^2(\Delta t) \rangle = 6D\Delta t \quad (1.5)$$

where D is the translational diffusion coefficient of the target particle, given as $D = 1/\beta\zeta$ in this case. The linear relation of the mean square displacement with time, $\langle \Delta \mathbf{R}^2(\Delta t) \rangle \propto \Delta t$, is called the normal diffusion. Further, in the linear regime, the self-part of the van-Hove correlation function, defined as $G_s(\Delta \mathbf{R}, \Delta t) = \langle \delta[\Delta \mathbf{R} - (\mathbf{R}(t + \Delta t) - \mathbf{R}(t))] \rangle$, becomes the following Gaussian distribution:

$$G_s(\Delta \mathbf{R}, \Delta t) = \left(\frac{1}{4\pi D \Delta t} \right)^{3/2} \exp \left(-\frac{\Delta \mathbf{R}^2}{4D \Delta t} \right), \quad (1.6)$$

Such a simple description is not always adequate for comprehensive analyses of the dynamics in diverse conditions, particularly with regard to particle/media characteristics and observation timescale. For instance, the constituent particles in some complex media like polymeric liquids [22] or glass-forming liquids [17, 23] can exhibit anomalous diffusion, expressed as $\langle \Delta \mathbf{R}^2(\Delta t) \rangle \propto \Delta t^\kappa$ with $\kappa \neq 1$, accompanied by the non-Gaussian statistics for $G_s(\Delta \mathbf{R}, \Delta t)$. Some systems, like polymeric liquids [24, 25] or biological media [18, 26, 27], show the linear mean square displacement $\langle \Delta \mathbf{R}^2(\Delta t) \rangle \propto \Delta t$ while $G_s(\Delta \mathbf{R}, \Delta t)$ deviates from the Gaussian distribution, called Brownian yet non-Gaussian diffusion. Some sophisticated frameworks or phenomenological modelings are required to gain an in-depth understanding of such complex diffusion of the particle.

1.2 BBGKY Hierarchy

On the microscopic scale where all the constituent molecules/particles are observable, the dynamics of the molecule/particle obey the classical mechanics at room temperature; the particle motions in the future are completely determined using the instantaneous coordinates and momenta of the particles in the system. The Hamiltonian H for the system involves all dynamical and structural information, and it is formally represented as

$$H(\{\mathbf{r}_i\}, \{\mathbf{p}_i\}) = \sum_i \frac{\mathbf{p}_i^2}{2m_i} + E_U(\{\mathbf{r}_i\}) \quad (1.7)$$

where \mathbf{r}_i and \mathbf{p}_i are the position and the velocity of the i th particle, m_i being the i th particle mass, and E_U denotes the interparticle potential energy depending on the system. For a given initial coordinates \mathbf{r}_i and momenta \mathbf{p}_i , the dynamics of the i th particle is calculated from Equation (1.7):

$$\dot{\mathbf{r}}_i = \frac{\partial H(\{\mathbf{r}_i\}, \{\mathbf{p}_i\})}{\partial \mathbf{p}_i} = \frac{\mathbf{p}_i}{m_i} \quad (1.8)$$

$$\dot{\mathbf{p}}_i = -\frac{\partial H(\{\mathbf{r}_i\}, \{\mathbf{p}_i\})}{\partial \mathbf{r}_i} = \sum_j \mathbf{F}_{ij} \quad (1.9)$$

where \dot{x} means the time-derivative of the variable x , \mathbf{F}_{ij} is the interparticle force between the i th and j th particles.

For the description of the multi-particle systems, the phase space distribution function at time t , $f(\{\mathbf{r}_i\}, \{\mathbf{p}_i\}; t)$, is useful. Since the phase points are not diminished or created, the time development of $f(\{\mathbf{r}_i\}, \{\mathbf{p}_i\}; t)$ obeys the equation of continuity called Liouville equation [11, 12,

28, 29], which is described as

$$\frac{\partial f(\{\mathbf{r}_i\}, \{\mathbf{p}_i\}; t)}{\partial t} + \sum_{i=1}^N \left(\frac{\partial f(\{\mathbf{r}_i\}, \{\mathbf{p}_i\}; t)}{\partial \mathbf{r}_i} \cdot \dot{\mathbf{r}}_i + \frac{\partial f(\{\mathbf{r}_i\}, \{\mathbf{p}_i\}; t)}{\partial \mathbf{p}_i} \cdot \dot{\mathbf{p}}_i \right) = 0 \quad (1.10)$$

Combining Equations (1.10), (1.8), and (1.9), the following relation is obtained:

$$\left(\frac{\partial}{\partial t} + \sum_{i=1}^N \frac{\mathbf{p}_i}{m_i} \cdot \frac{\partial}{\partial \mathbf{r}_i} \right) f(\{\mathbf{r}_i\}, \{\mathbf{p}_i\}; t) = - \sum_{i=1}^N \sum_{j=1}^N \left(\mathbf{F}_{ij} \cdot \frac{\partial}{\partial \mathbf{p}_i} \right) f(\{\mathbf{r}_i\}, \{\mathbf{p}_i\}; t) \quad (1.11)$$

If only the dynamics of the first particle, which can be assigned as the target particle, is observed, the distribution function for the whole variables $f(\{\mathbf{r}_i\}, \{\mathbf{p}_i\}; t)$ can be reduced. The time development of the phase space probability density on the target particle $f(\mathbf{r}_1, \mathbf{p}_1; t)$ is formally obtained straightforwardly from Equation (1.11) by integrating over variables $\mathbf{r}_2 \cdots \mathbf{r}_N \mathbf{p}_2 \cdots \mathbf{p}_N$:

$$\begin{aligned} & \int d\mathbf{r}_2 \cdots d\mathbf{r}_N d\mathbf{p}_2 \cdots d\mathbf{p}_N \left[\frac{\partial}{\partial t} + \sum_{i=1}^N \left(\frac{\mathbf{p}_i}{m_i} \cdot \frac{\partial}{\partial \mathbf{r}_i} \right) \right] f(\{\mathbf{r}_i\}, \{\mathbf{p}_i\}; t) \\ &= - \int d\mathbf{r}_2 \cdots d\mathbf{r}_N d\mathbf{p}_2 \cdots d\mathbf{p}_N \sum_{i=1}^N \sum_{j=1}^N \left(\mathbf{F}_{ij} \cdot \frac{\partial}{\partial \mathbf{p}_i} \right) f(\{\mathbf{r}_i\}, \{\mathbf{p}_i\}; t) \end{aligned} \quad (1.12)$$

Since $f(\{\mathbf{r}_i\}, \{\mathbf{p}_i\}; t)$ becomes zero when the i th particle coordinate \mathbf{r}_i is at the boundary of the system and also $f(\{\mathbf{r}_i\}, \{\mathbf{p}_i\}; t)$ approaches zero at the limit where an i th particle momentum approaches infinity, Equation (1.12) reduces to

$$\begin{aligned} \left[\frac{\partial}{\partial t} + \frac{\mathbf{p}_1}{m_1} \cdot \frac{\partial}{\partial \mathbf{r}_1} \right] f(\mathbf{r}_1, \mathbf{p}_1; t) &= - \sum_{j=1}^N \int d\mathbf{r}_j d\mathbf{p}_j \left(\mathbf{F}_{1j} \cdot \frac{\partial}{\partial \mathbf{p}_1} \right) f(\mathbf{r}_1, \mathbf{r}_j, \mathbf{p}_1, \mathbf{p}_j; t) \\ &= - N \int d\mathbf{r}_2 d\mathbf{p}_2 \left(\mathbf{F}_{12} \cdot \frac{\partial}{\partial \mathbf{p}_1} \right) f(\mathbf{r}_1, \mathbf{r}_2, \mathbf{p}_1, \mathbf{p}_2; t). \end{aligned} \quad (1.13)$$

Here, all the particles are assumed to be identical for simplicity. Equation (1.13) is not closed with respect to $f(\mathbf{r}_1, \mathbf{p}_1; t)$, and two-particle phase space distribution function $f(\mathbf{r}_1, \mathbf{r}_2, \mathbf{p}_1, \mathbf{p}_2; t)$ is required for further calculation. In the same manner, the calculation of $f(\mathbf{r}_1, \mathbf{r}_2, \mathbf{p}_1, \mathbf{p}_2; t)$ demands the three-particle phase space distribution function. Namely, to derive the equation for an n -particle phase space distribution function, the $n + 1$ -particle version is required, a relation known as the Bogoliubov-Born-Green-Kirkwood-Yvon (BBGKY) hierarchy [30–32]. In general, Equation (1.13) is analytically unsolvable, and some approximations are necessary for further computation.

When the particles are diluted like gas systems, Equation (1.13) can be further reduced [11]. In gas systems, a constituent particle moves ballistically until it collides with another particle, and the particle velocities change. In such a system, the right-hand side of Equation (1.13) phenomenologically corresponds to the change rate of $f(\mathbf{r}_1, \mathbf{p}_1; t)$ due to binary collisions:

$$\left[\frac{\partial}{\partial t} + \frac{\mathbf{p}_1}{m_1} \cdot \frac{\partial}{\partial \mathbf{r}_1} \right] f(\mathbf{r}_1, \mathbf{p}_1; t) = \Gamma_+ - \Gamma_- \quad (1.14)$$

where Γ_{\pm} means the gain and loss rates of $f(\mathbf{r}_1, \mathbf{p}_1; t)$ due to the collisions, and they are described as

$$\Gamma_+ = \frac{1}{m} \int d\omega d\mathbf{p}_2 \sigma(\omega, |\mathbf{p}_1 - \mathbf{p}_2|) f(\mathbf{r}_1, \mathbf{p}'_1; t) f(\mathbf{r}_1, \mathbf{p}'_2; t) \quad (1.15)$$

$$\Gamma_- = \frac{1}{m} \int d\omega d\mathbf{p}_2 a(\omega, |\mathbf{p}_1 - \mathbf{p}_2|) f(\mathbf{r}_1, \mathbf{p}_1; t) f(\mathbf{r}_1, \mathbf{p}_2; t), \quad (1.16)$$

where $a(\omega, |\mathbf{p}_1 - \mathbf{p}_2|)$ denotes the differential cross section with a solid angle ω , which depends on the interparticle potential. \mathbf{p}'_i and \mathbf{p}_i express the momenta of the i th particle before and after the collision, respectively. Here, Equation (1.14) is nothing but the Boltzmann transport equation. From the Boltzmann equation, various statistical quantities for gas systems, like diffusion coefficient, thermal conductivity, shear viscosity, etc., have been successfully computed [9, 11, 12]. While the Boltzmann equation is useful to express the transport phenomena, the application is limited to the gas systems where the dynamic correlations can be ignored. Namely, the Boltzmann equation can not directly address complex systems like polymeric liquids [13, 15], glass-forming liquid [17, 33], or some concentrated media [34, 35].

1.3 Generalized Langevin Equation

To account for the diffusion of a particle in concentrated media, the generalized Langevin equation [19, 28, 36–39] is helpful. This equation is the generalized version of Equation (1.2), incorporating the memory effects of fluid, expressed as follows.

$$M \frac{d\mathbf{V}(t)}{dt} = - \int_0^t dt' \zeta_G(t-t') \mathbf{V}(t') + \boldsymbol{\xi}_G(t) \quad (1.17)$$

where $\zeta_G(t)$ is the time-dependent friction coefficient reflecting the viscoelasticity of the fluid. For the generalized Langevin equation, the first and second moments of the noise term satisfy the

following relations.

$$\langle \boldsymbol{\xi}_G(t) \rangle = \mathbf{0} \quad (1.18)$$

$$\langle \boldsymbol{\xi}_G(t) \boldsymbol{\xi}_G(t') \rangle = \beta^{-1} \zeta_G(t - t') \mathbf{1}, \quad (1.19)$$

Here, if the relaxation time of the viscoelastic liquids is sufficiently small compared with the observation timescale, the memory kernel can be approximately expressed using the Dirac delta function: $\zeta_G \simeq 2\zeta\delta(t - t')$. In this case, Equation (1.17) can be reduced to Equation (1.2). The generalized Langevin equation is one of the successful descriptions for diffusion in soft matter systems [22, 40].

However, Equation (1.17) cannot always be justified. The generalized Langevin equation (1.17) can be formally provided from the Hamilton equation for the target particle velocity. This derivation employs the projection operator formalism, as detailed in literature [19, 28, 29, 36–39]. Nonetheless, the obtained formal expression does not tell us the information about the memory kernel and the statistics of the noise; the formal expression can not be practically analyzed. To avoid this difficulty, some phenomenological assumptions should be introduced into the formal expression, and that is the Gaussian noise assumption, as expressed in Equations (1.18) and (1.19). The Gaussian noise approximation can be justified when the target particle velocity slowly changes compared with the other variables; the effects of rapid variables can be regarded as the Gaussian noise due to the central limit theorem. Meanwhile, it cannot be told if the target particle velocity changes more slowly than other variables, except for simple systems, until detailed observations are conducted. Actually, in some complex soft matter media like colloidal suspension [41], glass-forming liquids [17], polymeric liquids [24, 42], rod-shaped particle [25, 43], and biological systems [26, 27], the constituent particles exhibit non-Gaussian diffusion. For such non-Gaussian diffusion, the generalized Langevin equation, which often assumes Gaussian noise, can not be employed.

1.4 Structure-Based Analyses

In general, the dynamics of a constituent particle in liquids is strongly influenced by the structure of the liquids [11, 13, 16, 44]. Therefore, in some systems, it is rational to describe the dynamics of the particle based on the characteristics of the structure under some approximations.

The transport coefficients of a fluid composed of hard spheres can be approximately described using the Boltzmann equation in the dilute limit [9, 11, 12, 45], where the correlations among particles can be ignored. However, at intermediate densities, the effects of the structure from the

multi-particle interactions cannot be neglected [11, 12]. To overcome this issue, Enskog [11, 12] incorporated the effect of the excluded volume of the particle into the Boltzmann equation. For hard spheres at intermediate densities, the collision frequency deviates from the prediction at the dilute limit, reflecting the structure of the fluid. Enskog corrected the collision frequency by introducing a part of the information of the radial distribution function into the Boltzmann equation. Additionally, Enskog modified the collision term by considering the excluded volume of the particle. Consequently, the Enskog theory, which utilizes some information on the structure of the fluid, is able to describe the transport coefficients of hard-sphere systems even for intermediate densities successfully.

Another formalism for describing the dynamics of liquids is the mode-coupling theory [29, 44, 46]. This theory uses the structure factor of the liquid as an input to describe the time correlation functions of the system variables and transport coefficients. For example, Gaskell and Miller [47] demonstrated that the mode-coupling theory can accurately predict the time correlation function of velocity in liquid rubidium. Furthermore, the mode-coupling theory is a potent theory capable of predicting the slowly relaxing dynamics of the liquid particles near the glass transition temperature based on the structure of the liquid [29, 33, 44, 46]. Vigorous studies with respect to the mode-coupling theory are being conducted [17, 44].

When a fluid undergoes a phase transition via variations in temperature or particle fraction, the dynamics of constituent particles change drastically. The dynamics in some phases can be modeled based on the symmetry in the system. For instance, fluids composed of rod-shaped particles exhibit nematic transition in response to changes in temperature and density [16, 48–51]. This transition, accompanied by directional order, alters the structure from the isotropic phase to the anisotropic phase. Along with the nematic transition, it is known that the dynamics of the constituent particles also changes from isotropic to anisotropic [13, 52, 53]. The dynamics of the constituent particles in nematic phases can be expressed using kinetic equations that incorporate the free energy of the nematic phase [13].

As has been explained, when the dynamics is significantly influenced by the structure, the dynamics of the particle can be modeled based on the characteristics of liquid structures. Meanwhile, in some liquids, the dynamics of the constituent particles qualitatively change without accompanying the qualitative variation in structures. For such liquids, the analyses of the dynamics based on the liquid structure are impossible.

1.5 Phenomenological Models without Relying on Structures

For the particle dynamics, which drastically changes without qualitative alternation in liquid structure, some phenomenological models have been constructed for each system. Such modelings incorporate characteristic dynamical properties to explain the macroscopic observables, such as diffusion coefficient, viscosity, and some relaxation functions.

In polymer melts, the dynamical behavior of the constituent polymer significantly changes against the molecular weight [54–56], although the structure almost remains unchanged. When the molecular weight of the polymer is sufficiently large, the diffusion coefficient of the constituent polymer is inversely proportional to the square of the molecular weight, and the viscosity is proportional to the 3.4 power of the molecular weight. Such behaviors for the long polymer can be phenomenologically explained by the Doi-Edwards model [13, 57–59]; the dynamics of the polymer is modeled as a worm-like object that moves along the polymer conformation. Meanwhile, if the molecular weight of the polymer is not sufficiently large, the diffusion coefficient of the polymer is inversely proportional to the molecular weight, and the viscosity is proportional to the molecular weight. These behaviors are explained via the Rouse model [13, 15, 60, 61]; the dynamics of the polymer can be modeled as just the Brownian motion of the multiple particles, which are linearly connected by springs.

Regarding solutions containing sufficiently long rod-like particles, the dynamics of the particle can qualitatively change with increasing the concentration within the isotropic phase; the positions and directions of the rods are uniformly distributed. When the rod-like particles are sufficiently dilute, their dynamics can be described by the Smoluchowski equation incorporating the hydrodynamic interaction [13, 62]. For the intermediate density regime, where the average distance between the rod-like particles becomes shorter than the particle axial length, the rotational motion of the particles becomes strongly constrained. In this situation, the rod-like particles can rotate slowly by diffusing along their major axis. For such a density, the rod particle experiences a significant decrease in the rotational diffusion coefficient compared to the dilute case. The behaviors in the intermediate density regime are explained by a phenomenological model [57, 58]. Namely, the dynamics of the rod-shaped particle is modeled as the motion where the rotational diffusion is strongly restricted while the motion along the major axis is not disturbed.

Although the above-mentioned phenomenological models successfully extract some essential features of the dynamics in the systems, they are case-specific and can not be straightforwardly

extended to different systems. So far, there is no systematic framework to express the dynamics of the particle, which does not strongly depend on the liquid structure. For a simple instance, the dynamics of the constituent particles in liquids can significantly change depending on their mass, while the mass has no influence whatsoever on structure, which is a natural consequence of statistical mechanics. Such a dynamic behavior can not be straightforwardly modeled. Muraka et al. [63] analyzed a system composed of binary spherical particles interacting via Lennard-Jones potentials with different masses through molecular dynamics simulation. They reported that varying the mass of the heavier particles causes a significant change in the displacement distribution of the lighter particles; the lightweight particle exhibits strong non-Gaussian diffusion. Fenz et al. [64] have reported that in a binary Lennard-Jones fluid, the relaxation behavior of the velocity of the constituent particles qualitatively changes depending on the mass of the particles. Similar behavior caused by the alternation of mass was also reported by Acharya et al. [65] For such a diffusion of the constituent particle, the modeling path has not been established.

1.6 Dynamics in Structureless Media

From theoretical interests, the dynamical behaviors of the constituent particle within structureless media have been investigated. In such systems, the dynamics of the particle can exhibit intriguing behaviors while the positions or directions of the particles are uniformly distributed for any situation [34, 35, 43, 66].

Frenkel and Maguire [34, 35] investigated the dynamics of fluids composed of infinitely thin hard rods using event-driven molecular dynamics simulations. As these particles have no excluded volume, their static structure always remains that of an ideal gas, and they do not undergo Nematic or Smectic transitions in any density regimes. In this system, at a small concentration, the motion of the particles can be described using the Enskog theory [11, 12], where each collision is assumed to be statistically independent. Meanwhile, when the particle concentration exceeds a certain value, a strong constraint on the rotational motion is evident. For such a concentration regime, as explained in detail in Chapter 5, a nontrivial phenomenon has been reported: the center-of-mass diffusion coefficient of the rod-shaped particle increases with an increase in particle concentration. A similar phenomenon has also been reported for rod particles in two-dimensional systems [43, 67]. The mechanism of this increase in diffusivity remains unsolved, although some phenomenological models incorporating some unclear concepts were considered [35, 43].

Kettel et al. [66] investigated the dynamics of a system containing particles, each formed by

three infinitely thin rods connected at the centers of mass of each rod, by numerical simulation. In this system, their structure is also that of an ideal gas since the particles have no excluded volume. Unlike straight rods [34,35], the diffusivity of the particles decreases monotonically with an increase in particle density. In high-density regions, the mean square displacement of the particles exhibits anomalous diffusion, $\langle \Delta \mathbf{r}^2(\Delta t) \rangle \propto \Delta t^\kappa$ with $\kappa \neq 1$, and strong non-Gaussian behavior. Although this behavior is akin to that observed in glass-forming liquids, the structure remains unchanged. Hence, the dynamics cannot be straightforwardly analyzed within the framework of the mode-coupling theory mentioned in Section 1.4.

Spherical particles immersed in fixed-point obstacles can also exhibit complex behavior while the structure is homogeneous. Höfling and Franosch [68, 69] studied the dynamics of a point particle moving among spherical obstacles, known as the Lorentz gas, using simulations. In their system, the obstacles are allowed to overlap each other, and the distribution of the center of mass is uniformly distributed. Even in the simple nature of the system, the dynamics of the mobile particle drastically changes with increasing obstacle density; the mobile particle shows simple ballistic and diffusive behavior for dilute cases, while it exhibits anomalous and non-Gaussian diffusion for concentrated regimes. Further, the dynamics of the mobile particle is completely confined by the surrounding obstacle at a sufficiently large concentration. Similar phenomena of Lorentz gas systems have been reported in many works [70, 71]. The dynamics of a spherical particle in such a simple nature can exhibit intriguing diffusion with non-Gaussianity, while it is not simply understood using the conventional frameworks as described in Sections 1.3 and 1.4.

It should be noted here that, even in structureless media, the dynamics of the particle can be analytically solvable in special cases. Jepson [72] and Lebowitz et al. [73, 74] theoretically studied the one-dimensional hard-rod systems, where constituent particles move ballistically along the line until collision with the neighboring particles. Harris [75] theoretically analyzed the Brownian version; the constituent particles move stochastically, not ballistically. Thanks to the special nature of the one-dimensionality, the time-correlation functions of the constituent particle can be exactly calculated. Although these works clarified the specialty of the dynamics of the one-dimensional systems, the employed method can not be extended to the other dimensional cases.

The dynamics of the particle in the structureless media can not be straightforwardly understood based on existing theoretical frameworks. Further, even though the investigation of such media may provide fresh views for modeling the dynamics of the particles in diverse systems, few insights have been gained except for slow glassy dynamics [66]. Specifically, the systematic analyses of the impact of the fundamental particle properties like mass and shape, which can significantly affect

the dynamics of the particle as explained in Sections 1.4 and 1.6, have not been explored.

1.7 Subject of Dissertation

In this thesis, the dynamics of a target particle situated in simple structureless media is computed using numerical and theoretical methods. In the media, the constituent particles are spherical or point masses, and the structure is always just an ideal gas; the positions are uniformly distributed in three-dimensional space. The effects of fundamental parameters such as the mass and shape of the target particle and the concentration of the media on the dynamics of the target particle are investigated. The structure of this dissertation is organized as follows.

Chapter 2: Non-Gaussian Diffusion of Particle in Ideal Gas. This chapter examines the dynamics of the target particle immersed in an ideal gas, which is comprised of point masses, using event-driven type simulations. In this system, the target particle can exhibit anomalous and non-Gaussian diffusion, which has been considered to occur in complex media. To clarify the mechanism of this type of diffusion in the examined system, analyses focusing on collisions between the target particle and point masses are performed.

Chapter 3: Fluctuating Diffusivity of Particle in Gas Mixtures: Numerical Study. The non-Gaussian diffusion of a particle can be evident even in dilute gas. To clarify the origin of the non-Gaussian diffusion, this chapter investigates the dynamics of a particle situated in a dilute gas, constructing stochastic simulations based on collision statistics. Detailed analyses for time-correlation functions revealed that the non-Gaussian diffusion is caused by fluctuating diffusivity, and its physical origin is also identified.

Chapter 4: Fluctuating Diffusivity of Particle in Gas Mixtures: Theoretical Study. To describe the non-Gaussian diffusion in the gas system, theoretical analyses are conducted. Based on the Lorentz gas model, which consists of a mobile target particle situated in fixed obstacles, the non-Gaussian diffusion in the gas system, observed in Chapter 3, is quantitatively reproduced.

Chapter 5: Increase in Diffusivity of Rod in Obstacles. The dynamics of a single rod-shaped particle moving through fixed point obstacles is numerically examined, under the Markovian process. A stochastic simulation based on the collision statistics between the rod and an obstacle

is constructed to calculate the dynamics of the rod. The dynamics of the rod are analyzed with various aspect ratios and obstacle density, and the dynamics of the rod qualitatively changes against these parameters.

Chapter 6: Conclusion. This chapter compiles the results and understandings gained in each chapter. Afterward, the conclusion of this dissertation is presented.

Chapter 2

Non-Gaussian Diffusion of Particle in Ideal Gas

Abstract

The dynamics of a target spherical particle immersed in an ideal gas, consisting of the moving point masses, are numerically examined with various mass ratios and number density of the gas. The target particle exhibits non-Gaussian anomalous diffusion when the mass of the target particle is smaller than that of the gas particle in a concentrated regime. To clarify this type of diffusion, analyses focusing on the collisions are performed. Consequently, the observed non-Gaussian anomalous diffusion is attributed to the repeated collisions between the target and gas particles.

2.1 Introduction

As mentioned in Chapter 1, particles/molecules in a fluid with sizes smaller than a micrometer undergo random motion due to the collisions with fluid molecules [6, 8]. Over time scales where particles experience a large number of collisions, their motion can be described using a Gaussian process due to the central limit theorem. For such a long timescale, the dynamics of the target particle can be easily described using the conventional diffusion equation. In contrast, for short time scales where only a few collisions occur, it is generally challenging to theoretically describe the dynamics of the particle by simple coarse-graining descriptions.

In considering the short-time dynamics of the target particle, it might be useful first to examine a simple system. A possible system is a target particle situated in gas particles with a hard-core

potential [76–81]. Generally, in gaseous systems, it is known that collisions between gas molecules correlate, leading to slow relaxation known as long-time tails [82, 83]. This chapter addresses a simple system where such a long-time tail is absent. Specifically, by treating gas molecules as point masses, a system where collisions between gas molecules do not take place is considered. Such a setup can be regarded as an approximate representation when the size of the gas particles is considerably smaller than that of the target particle and the mean distance between the gas particles.

In an equilibrium state, when the size of the target particle is sufficiently smaller compared to the mean distance between ideal gas particles, the motion of the target particle can be described using the Boltzmann equation [11, 45], as represented in Equation (1.14). Generally, analyzing the time correlation function from the Boltzmann equation is not straightforward. However, it can be easily analyzed when the mass of the target particle is significantly larger than that of the surrounding gas particles [84]. In Equation (1.14), by expanding the right-hand side in terms of the mass ratio of the target particle to the gas particle, M/m , and retaining only the leading terms for $M/m \ll 1$, a Fokker-Planck equation equivalent to the Langevin equation (1.2) can be straightforwardly obtained. Namely, the motion of the target particle becomes a simple Gaussian process when the target particle is sufficiently heavier than that of the gas particle. Meanwhile, when the target particle size is not significantly smaller than the distance between the ideal gas particles or when the mass of the target particle is not significantly larger compared with that of the gas particles, such a simple theoretical description may not be justified. In this chapter, by systematically varying the mass of the target particle and the number density of the gas particles, the motion of the target particle during time scales for several to dozens of collisions between the target particle and the gas particles is investigated through numerical simulation.

2.2 Method

2.2.1 System Setting

The system is cubic with the periodic boundary conditions and includes a single target particle and an ideal gas composed of N point masses; the gas particles do not interact with each other, whereas the target particle collides with the gas particles. The interparticle interaction between the target particle and gas particle is the hard-core repulsion potential. The target particle moves ballistically until it collides with an ideal gas particle, and the velocity of the target particle after

the collision is obtained based on the conservation laws of the momentum, energy, and angular velocity as

$$\mathbf{V}_{c,i+1} = \mathbf{V}_{c,i} + \frac{2m}{m+M}(\mathbf{v}_{v,i} - \mathbf{V}_{c,i}) \cdot \mathbf{u}_{c,i} \mathbf{u}_{c,i} \quad (2.1)$$

where M and m are the masses of the target particle and colliding gas particle, $\mathbf{V}_{c,i}$ the target particle velocity after the i th collision, $\mathbf{v}_{c,i}$ the colliding gas-particle velocity at the i th collision, and $\mathbf{u}_{c,i}$ denotes the direction unit vector connecting the target particle to the colliding gas particle at the i th collision. In the same manner, the velocity of the colliding particle after the collision is calculated as

$$\mathbf{v}_{c,i+1} = \mathbf{v}_{c,i} - \frac{2M}{M+m}(\mathbf{v}_{c,i} - \mathbf{V}_{c,i}) \cdot \mathbf{u}_{c,i} \mathbf{u}_{c,i} \quad (2.2)$$

The diameter of the target particle is d , and that of the gas particle is zero. The inverse temperature of the system is β , and the number density of the gas particle is $\rho = N/(\mathcal{V} - \pi d^3/6)$ with \mathcal{V} being the system volume. The length of the one side of the system box is $\mathcal{V}^{1/3}$. If m , d , and β are chosen to define the dimensionless units, the dynamics of the particles are qualitatively affected only by the target particle mass ratio M/m and the number density of the ideal gas ρd^3 for the dimensionless representation. The following results are displayed with the scaled forms concerning m , d , and β .

2.2.2 Simulation Protocol

In the simulation, the initial state is created to satisfy the equilibrium statistics; the target particle and gas particles are situated uniformly in the box without any overlaps, and the velocities of the particles are generated based on the Maxwell-Boltzmann distribution. To prevent the drift of the system, the velocity of the center of mass of the system is subtracted from all the velocities of the particles. Then, the velocities of the particles are scaled so that the mean of the kinetic energy per degree of freedom becomes exactly $1/2\beta$. For the initial state above, the time development of the system is numerically calculated via the established event-driven hard-sphere molecular dynamics simulations [76].

In the simulation, the handling of the image particle by the periodic boundary conditions should be carefully treated, or undesirable overlaps between the target and gas particles can occur. In order to prevent the overlap, the following steps are implemented.

1. An initial state is generated.

2. The maximum component among the relative velocities between the target particle and gas-particle $v_{\text{rel,max}} = \max(v_x - V_x, v_y - V_y, v_z - V_z)$ is obtained. From $v_{\text{rel,max}}$ the possible minimum collision time interval between the target and mirror gas particle is calculated as $\Delta t_{\text{mirror}} = (\mathcal{V}^{1/3} - d)/2v_{\text{rel,max}}$.
3. The ideal gas particles that collide with the target particle in the range $|r_x - R_x| < \mathcal{V}^{1/3}/2$, $|r_y - R_y| < \mathcal{V}^{1/3}/2$, and $|r_z - R_z| < \mathcal{V}^{1/3}/2$ are obtained, and the minimum collision time interval Δt_{min} is also computed.
4. If $\Delta t_{\text{mirror}} < \Delta t_{\text{min}}$, the positions of all the particles are updated for the time duration Δt_{mirror} , time is also updated as $t \rightarrow t + \Delta t_{\text{mirror}}$, while the velocities are not renewed. After this updates, return to step 3.
5. All the positions of the particles are updated for the time duration Δt_{min} , time is renewed as $t \rightarrow t + \Delta t_{\text{min}}$, and the velocities of the target and colliding particle are changed based on Equations (2.1) and (2.2).
6. The steps 2-5 are repeated until 10^7 collisions occur.

From this procedure, the trajectories of the target particle are numerically calculated with various target particle mass M and the number density of the ideal gas ρ . Here, in order to check the simulations, the basic statistical properties are computed, and they are reasonable; the statistics of the target particle velocity become the Maxwell-Boltzmann distribution, and the radial distribution function of the ideal gas particle around the target particle becomes zero at a distance smaller than $d/2$ and unity otherwise.

2.3 Results

2.3.1 Time Correlation Functions

Figure 2.1(a) represents the mean square displacement as a function of time lag Δt for the ideal gas density $\rho d^3 = 1$ with various mass ratios M/m . In the short time regime, the ballistic behavior, $\langle \Delta \mathbf{R}^2(\Delta t) \rangle \propto \Delta t^2$, is observed, and the MSD decreases as M increases. This behavior reflects that the mean of the kinetic energy of the target particle depends on its mass: $\langle \mathbf{V}^2(t) \rangle = 3/\beta M$. In a long-time regime, diffusive behavior $\langle \Delta \mathbf{R}^2(\Delta t) \rangle \propto \Delta t$ is observed as a consequence of the multiple collisions by the surrounding gas particles. In this long-time regime, MSD decreases as M

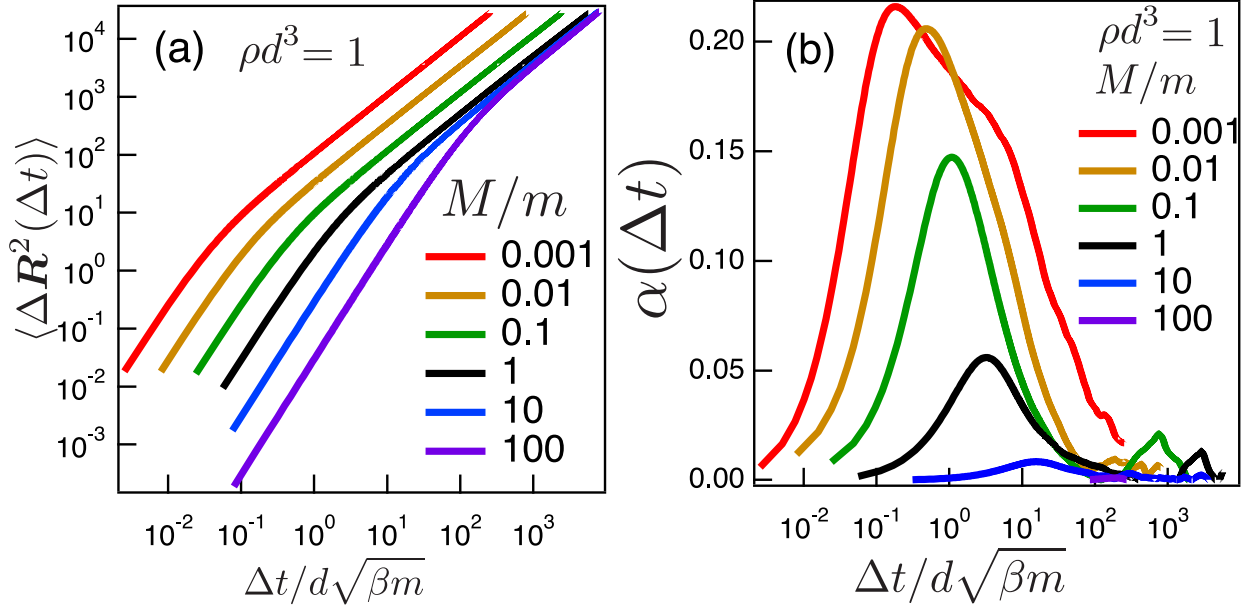


Figure 2.1: Simulation results for (a) the mean square displacement and (b) the non-Gaussian parameter at a fixed ideal gas number density $\rho d^3 = 1$ with the various target particle masses M/m .

increases for the small mass $M/m \ll 1$, while MSD converges at the large mass $M/m \gg 1$. The convergence at large M is expected behavior since the Langevin equation, which is independent of the mass in the long-timescale, is derived from the Boltzmann equation at the large mass limit $M/m \gg 1$ [84]. In contrast to this, the small mass case would not be simple, compared with the situation for the large mass case.

Figure 2.1(b) displays the non-Gaussian parameters against time lag Δt , defined as $3\langle \Delta R^4(\Delta t) \rangle / 5\langle \Delta R^2(\Delta t) \rangle^2$, at $\rho d^3 = 1$ with the various mass ratios M/m . At the initial time lag $\Delta t = 0$, NGP shows zero for any mass ratio, which reflects that the statistics of the target particle velocity follow the Maxwell-Boltzmann distribution. Also, in the long-time regime, NGP approaches zero, which is a natural consequence of the central limit theorem. Meanwhile, in the intermediate timescale, NGPs exhibit peaks, and the peak top value becomes large when the target particle mass is small $M \ll m$. Non-Gaussian diffusion is often attributed to heterogeneous environments like glass-forming liquids [17, 85] or some polymeric liquids [25]. However, the current system does not have any heterogeneous environments; the structure of the fluid is always the ideal gas. Therefore, the non-Gaussian behavior would be attributed not to the structure, but the kinetics.

Figure 2.2 shows the MSD and NGP with various ideal gas number densities ρ at the constant

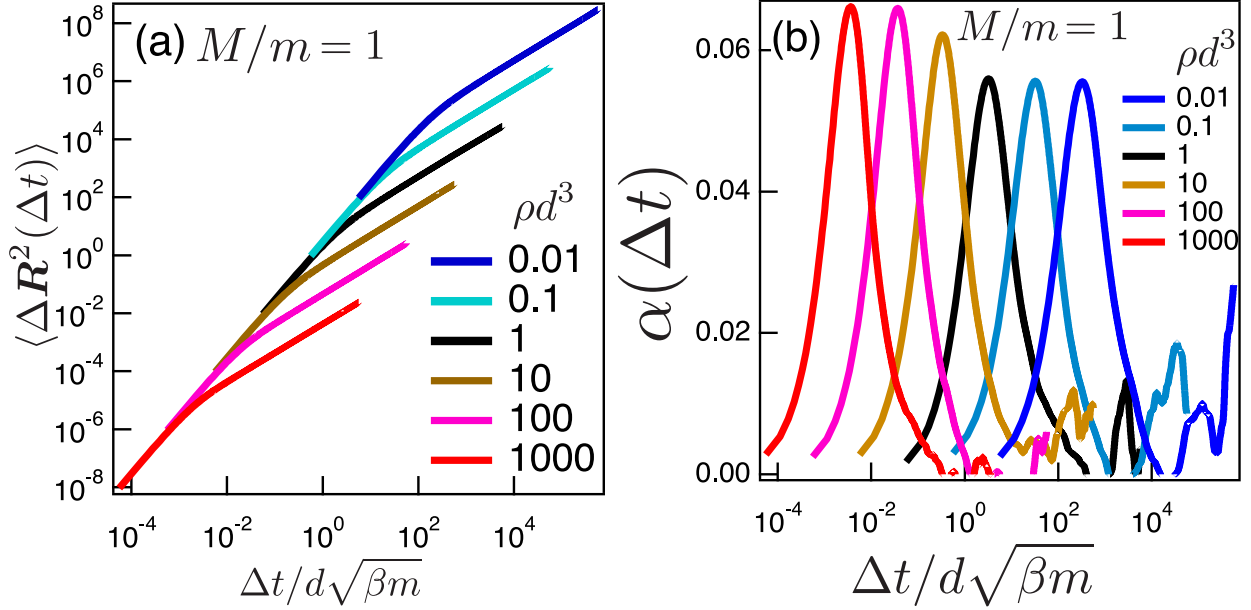


Figure 2.2: Simulation results for (a) the mean square displacement and (b) the non-Gaussian parameter at a fixed target particle mass $M/m = 1$ with the various ideal gas number density ρd^3 .

mass ratio $M/m = 1$. The MSDs show simple ballistic and diffusive behaviors at the short and long timescale, respectively. The crossover time from the ballistic motion to the diffusive motion decreases as ρ increases since the mean free time monotonically decreases with increasing ρ . In contrast to the simple behavior in MSD, NGP exhibits a non-negligible peak. Interestingly, the peak top value in NGP slightly increases as gas density increases for $\rho d^3 \gtrsim 1$, while it remains almost constant for $\rho d^3 \lesssim 1$. Although the increase in NGP with increasing matrix density has been commonly observed in some heterogeneous systems [69], the current system does not have any heterogeneities in the matrix structure.

From Figures 2.1 and 2.2, the dynamics of the target particle is qualitatively changed by the target particle mass M and the gas number density ρ . For large mass $M/m \gg 1$, the dynamics of the target particle becomes approximately the Gaussian process, and it is consistent with the fact that the dynamics of a heavier particle in light gas is approximately described using the Langevin equation [84]. When the number density is small $\rho d^3 \lesssim 1$, the dynamics of the target particle will be analyzed using the Boltzmann equation. However, for the small mass $M/m \lesssim 1$ and large gas number density $\rho d^3 \gtrsim 1$, the dynamics of the target particle would not be expressed using simple descriptions like the Langevin equation or the Boltzmann equation. Afterward, the dynamics of the target particle will be analyzed for the non-trivial parameter regime: $M/m \leq 1$ and $\rho d^3 \geq 1$.

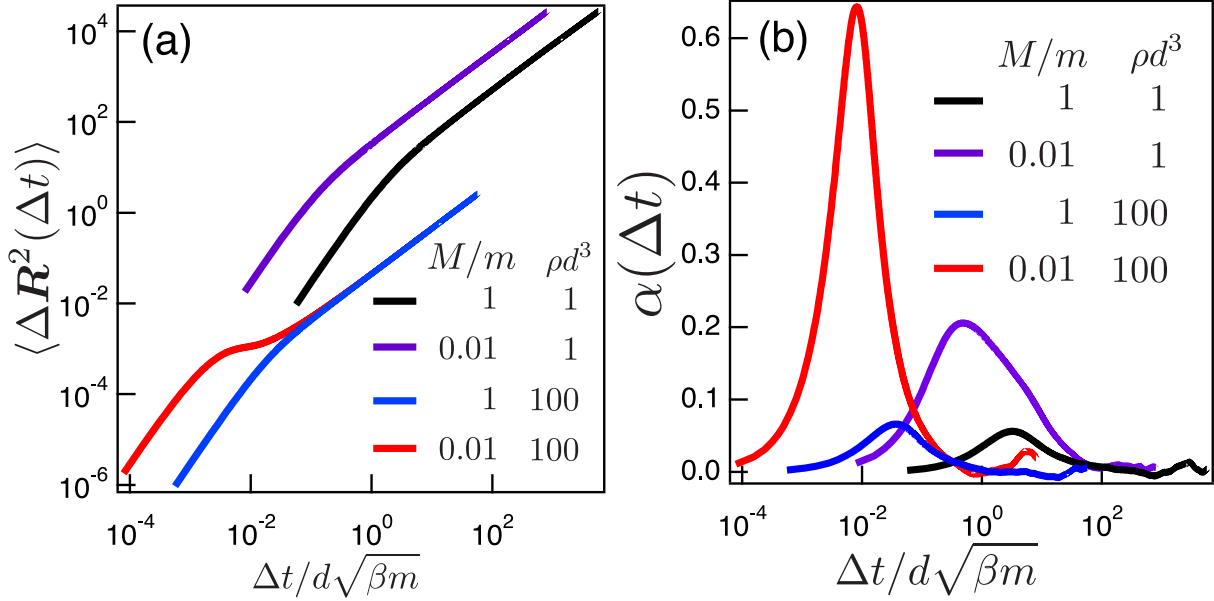


Figure 2.3: Representative simulation results for (a) the mean square displacement and (b) the non-Gaussian parameter of the target particle with the various scaled target particle mass M/m and scaled gas number density ρd^3 for the parameter regime $M/m \leq 1$ and $\rho d^3 \geq 1$.

Figure 2.3 illustrates the representative MSD and NGP for $M/m \leq 1$ and $\rho d^3 \geq 1$. When $M/m = 0.01$ and $\rho d^3 = 100$, MSD exhibits the sub-diffusive regime, $\langle \Delta R^2(\Delta t) \rangle \propto \Delta t^\kappa$ with $\kappa \neq 1$, while MSD shows simple ballistic and diffusive behavior in the other parameter sets. The sub-diffusive regime has been reported for the constituent particles in some complex systems like glass-forming liquids [17] and polymeric liquids [22]. In Figure 2.3, NGP has a significantly large peak for $M/m = 0.01$ and $\rho d^3 = 100$. The sub-diffusive behavior without the Gaussian distribution can not be straightforwardly understood based on the generalized Langevin equation and the Boltzmann equation. One question here may arise: what is the origin of the observed sub-diffusion accompanied by the non-Gaussianity in the current ideal gas system?

To investigate the dynamics in detail, the velocity autocorrelation function (VAC), defined as $\langle \mathbf{V}(\Delta t) \cdot \mathbf{V}(0) \rangle \beta M / 3$, is calculated. The representative simulation results of VAC for the parameter regime $M/m \leq 1$ and $\rho d^3 \geq 1$ are displayed in Figure 2.4. For the case of $M/m = 0.01$ and $\rho d^3 = 100$, the VAC exhibits a negative correlation at the intermediate time regime where MSD shows the sub-diffusion as displayed in Figure 2.3(a). The negative correlation means that the target particle is effectively reflected back through some number of collisions with the gas particles. Here, based on the definition, VAC is related to the MSD as $6\langle \mathbf{V}(\Delta t) \cdot \mathbf{V}(0) \rangle = \partial^2 \langle \Delta R^2(\Delta t) \rangle / \partial \Delta t^2$.

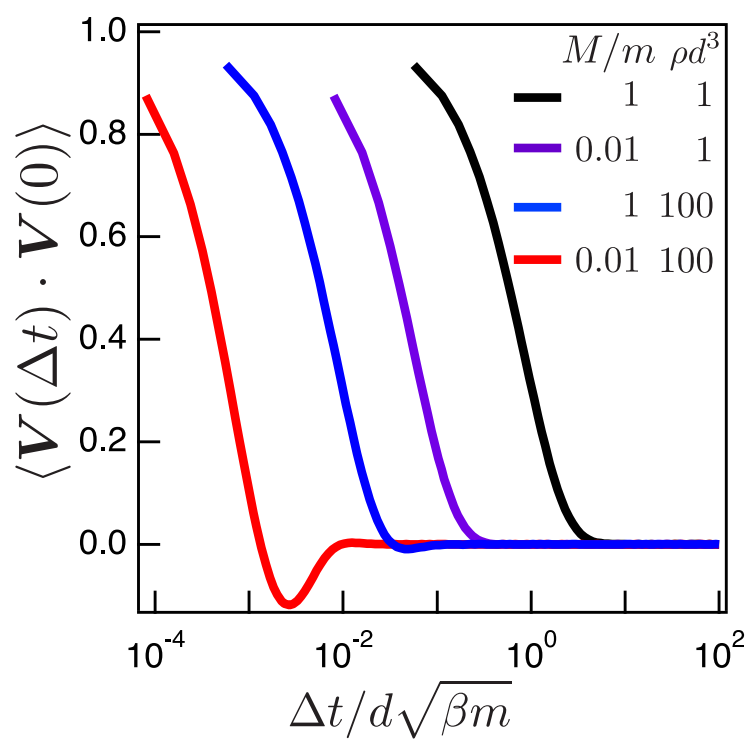


Figure 2.4: Velocity autocorrelation function of the target particle with the various M/m and $\rho\sigma^3$ within the parameter regime $M \leq 1$ and $\rho\sigma^3 \geq 1$.

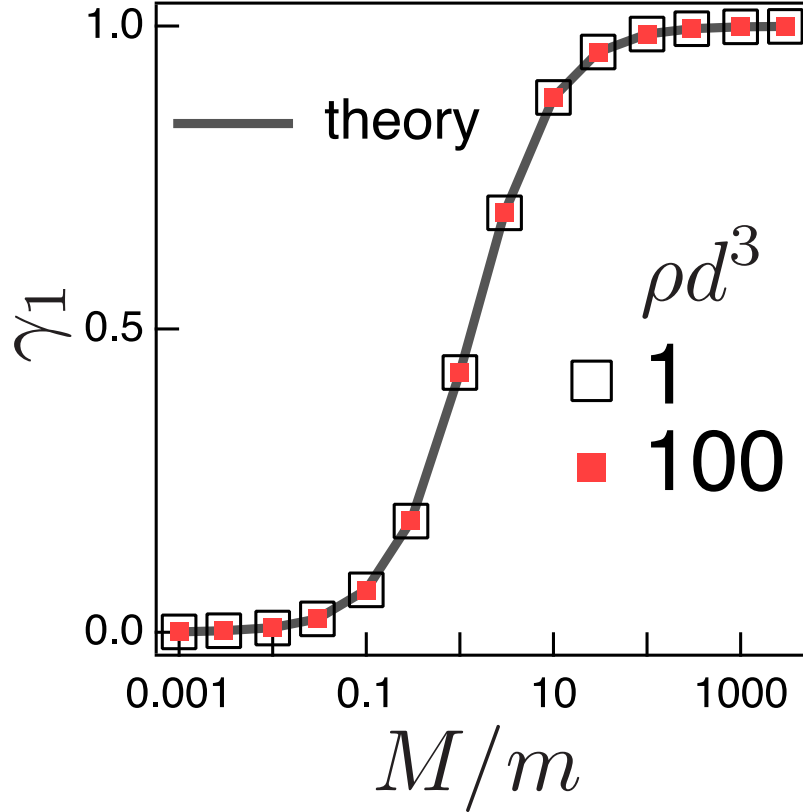


Figure 2.5: Correlation factor between the velocities before and after a single collision γ_1 , defined as Equation (2.3), as a function of the scaled mass of the target particle M/m with two different gas densities $\rho d^3 = 1$ and 100. Symbols represent the simulation results, and the theoretical result defined as Equation (2.16) is also displayed using a solid curve for comparison.

Therefore, the negative correlation in VAC corresponds to the inflection point, which corresponds to sub-diffusive behavior, in MSD. Also, from Figures 2.3(a) and (b), the sub-diffusive regime occurs at the timescale where the NGP has a significant peak. Thus, it is expected that the sub-diffusive behavior in MSD and strong peak in NGP would be attributed to the observed negative velocity correlation. The following analyses focus on the observed negative correlation in VAC.

2.3.2 Focusing on Collision Dynamics

It would be suspected that the negative velocity correlation can appear by the single collision when the target particle mass is sufficiently small compared with the surrounding gas particle since the gas particle behaves like a fixed obstacle in a short timescale where the target particle suffers a few collisions. However, this naive expectation is not valid. Here, the velocity correlation before

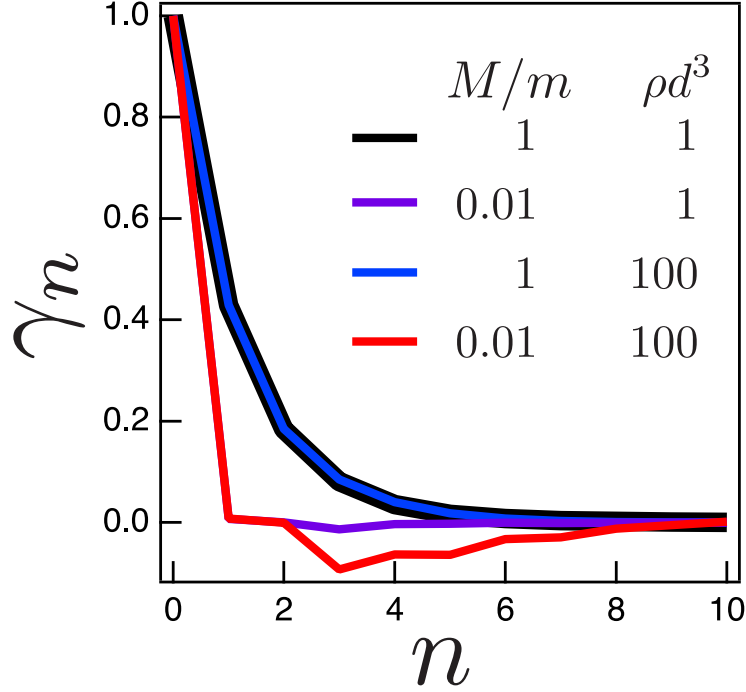


Figure 2.6: Correlation factor for the velocities before and after n th collisions of the target particle for the parameter regime $M/m \leq 1$ and $\rho d^3 \geq 1$, obtained from the simulations.

and after a single collision is defined:

$$\gamma_1 \equiv \frac{\langle \mathbf{V}_{c,i} \cdot \mathbf{V}_{c,i+1} \rangle_{\text{coll}}}{\langle \mathbf{V}_{c,i}^2 \rangle_{\text{coll}}} \quad (2.3)$$

where $\mathbf{V}_{c,i}$ denotes the velocity of the target particle before the i th collision, and $\langle x \rangle_{\text{coll}}$ the statistical average of a variable x with respect to collisions. Figure 2.5 shows the simulation results for γ_1 against scaled mass M/m with two scaled number densities $\rho d^3 = 1$ and 100, defined as Equation (2.3). γ_1 is always positive for any mass ratio, including small mass or large number density cases. This result indicates that the velocity can not be negatively correlated by a single collision. Fortunately, γ_1 can be theoretically calculated, and the theory is perfectly consistent with the simulation results. The detail of the theoretical calculation for γ_1 is given in Appendix 2.A.

The velocity of the target particle is positively correlated via a single collision for any mass ratio, while the VAC can exhibit negative correlations for the small M/m cases. This result suggests that the target particle velocity is negatively correlated through multiple collisions. The correlation factor that can describe the velocities before and after the n th collision is here defined

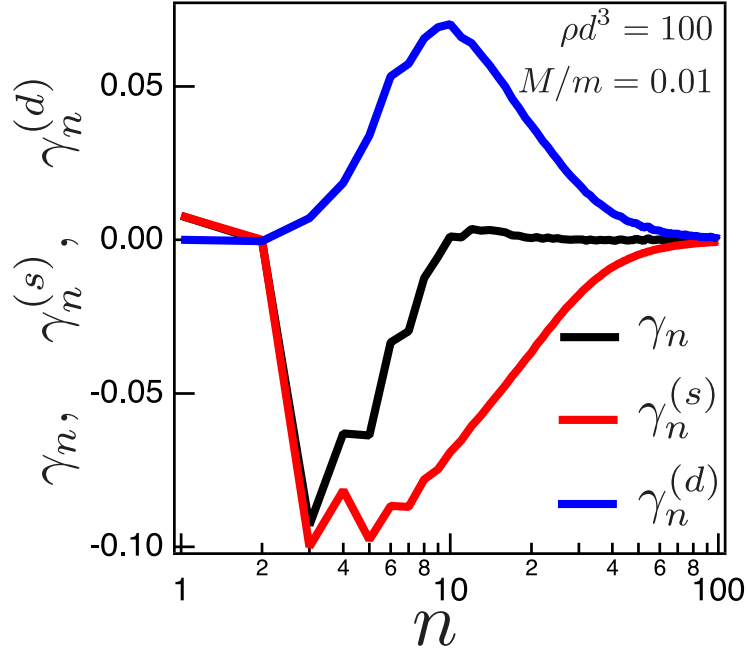


Figure 2.7: Simulation results for the self and distinct parts of the velocity correlation before and after n th collision γ_n , defined as Equations (2.6) and (2.7), at the target particle mass $M/m = 0.01$ and the gas number density $\rho d^3 = 100$.

as

$$\gamma_n \equiv \frac{\langle \mathbf{V}_{c,i} \cdot \mathbf{V}_{c,i+n} \rangle_{\text{coll}}}{\langle \mathbf{V}_{c,i}^2 \rangle_{\text{coll}}} \quad (2.4)$$

This factor has been introduced by Taloni et al. [86] to investigate the velocity correlation with respect to collision number and would be useful for the current purpose. Figure 2.6 displays the representative γ_n against the number of collisions with the parameter regime $M/m \leq 1$ and $\rho d^3 \geq 1$. From the results, γ_1 is not negatively correlated, as shown in Figure 2.5. Interestingly, γ_2 does not show the negative value for simulated M/m , while the negative correlation emerges for the number of collisions greater than or equal to 3. Taloni et al. [86] also obtained a similar result for the two-dimensional hard-sphere fluid, although the origin of the negative correlation of γ_n at $n \geq 3$ was not clarified.

The number three would relate to the collision of the target particle with the same gas particle; the process where the target particle first collides with a gas particle, leaves for the first particle due to the collision rule (Equations (2.1) and (2.2)), then collides with another particle, and go back to the first particle requires three collisions at least. To distinguish the contribution from the collision with the same particle and other particles to the negative correlation of the velocity, γ_n

is decomposed into self and distinct parts, $\gamma_n^{(s)}$ and $\gamma_n^{(d)}$, as follows.

$$\gamma_n \equiv \gamma_n^{(s)} + \gamma_n^{(d)}, \quad (2.5)$$

$$\gamma_n^{(s)} \equiv \frac{\langle \mathbf{V}_{c,i} \cdot \mathbf{V}_{c,i+n} \delta_{K_{i+1}, K_{i+n}} \rangle_{\text{coll}}}{\langle \mathbf{V}_{c,i}^2 \rangle_{\text{coll}}}, \quad (2.6)$$

$$\gamma_n^{(d)} \equiv \frac{\langle \mathbf{V}_{c,i} \cdot \mathbf{V}_{c,i+n} (1 - \delta_{K_{i+1}, K_{i+n}}) \rangle_{\text{coll}}}{\langle \mathbf{V}_{c,i}^2 \rangle_{\text{coll}}}, \quad (2.7)$$

where δ denotes the Kronecker delta, and K_i indicates the gas particle number at the i th collision. Figure 2.7 displays $\gamma_n^{(s)}$ and $\gamma_n^{(d)}$ for the parameter $M/m = 0.01$ and $\rho d^3 = 100$, and γ_n is also presented for comparison. $\gamma_n^{(d)}$ becomes 0 at $n = 1$ due to the definition of Equation (2.7), and $\gamma_n^{(s)}$ shows 0 at $n = 2$ since the target particle can not collide with the same gas particle for the second collision. Intriguingly, $\gamma_n^{(s)}$ exhibits the negative correlation for $n \geq 3$, and this result indicates that the origin of the negative velocity correlation originates from the collisions with the same gas particle.

2.4 Discussion

A similar negative value in the velocity autocorrelation function (VAC) is also observed in the hard-sphere systems [79, 87]. Alder et al. [79] studied the dynamics of a target particle situated in the hard-sphere fluids using the event-driven type algorithm [76]. They calculated the velocity autocorrelation function of the target particle with various mass ratios and presented the difference in the numerical data from the Enskog theory [11], which is a conventional theory for gas systems. The result indicated that the velocity of the target particle is negatively correlated when the mass of the target particle is smaller than that of the fluid particles, while the origin of this behavior is not clarified. Although there is a difference between the current system and that in the prior work, [79], the negative correlation of a lightweight particle in the hard-sphere fluids may be attributed to the collisions with the same fluid particle, as clarified in the current work.

This chapter clarifies the origin of the large peak observed in Figure 2.3 for small M and large ρ regime, however, NGP also exhibits non-negligible peaks even when the number density of gas is not large, as displayed in Figure 2.1. Similar behavior is also observed for the hard-sphere gas composed of identical particles [88] and Lennard-Jones liquid [89], although its origin has not been elucidated. Such a non-Gaussianity observed in dilute situations is investigated in Chapter 3 and 4.

2.5 Summary

This Chapter investigated the dynamics of the target particle immersed in the ideal gas composed of point masses, varying the target particle mass M and number density of the ideal gas ρ . For large target particle mass $M/m \geq 1$, the dynamics of the target particle can be approximately regarded as the Gaussian process; the dynamics is described using the Langevin equation. In contrast, when the target particle mass is small $M/m \leq 1$, the statistics of the displacement deviate from the Gaussian distribution as expected. Intriguingly, for $M/m \leq 1$ and $\rho d^3 > 1$, MSD exhibits the sub-diffusion, NGP shows strong non-Gaussianity, and negative velocity correlation appears in VAC. To clarify this complex diffusion, analyses focusing on collisions between the target and gas particles were conducted. As a consequence, the observed non-Gaussian and anomalous diffusion originates from repeated collisions with the same gas particle.

2.A Theretical Analysis for γ_1

In this appendix, the correlation factor γ_1 , defined as Equation (2.3), is analytically calculated. The velocities before and after a single collision are denoted as $\mathbf{V}_{c,0}$ and $\mathbf{V}_{c,1}$, respectively. The velocity of the colliding gas particle is represented as $\mathbf{v}_{c,0}$. The current system is in an equilibrium state; the ideal gas particles are uniformly distributed in space, and the velocities of target and gas particles follow the Maxwell-Boltzmann distribution. Based on this situation, γ_1 is analytically computed.

The velocity of the target particle after the collision is obtained from the conservation of the momentum and energy, as described in Equation (2.1). γ_1 is calculated as the statistical average of the inner product between the velocities before and after the collision as follows:

$$\langle \mathbf{V}_{c,1} \cdot \mathbf{V}_{c,0} \rangle_{\text{coll}} = \frac{\int d\mathbf{V}_{c,0} d\mathbf{v}_{c,0} d\mathbf{u}_{c,0} P_{\text{MB}}(\mathbf{V}_{c,0}; M) P_{\text{MB}}(\mathbf{v}_{c,0}; m) P(\mathbf{u}_{c,0}) |\mathbf{v}_{c,0} - \mathbf{V}_{c,0}| \mathbf{V}_{c,1} \cdot \mathbf{V}_{c,0}}{\int d\mathbf{V}_{c,0} d\mathbf{v}_{c,0} d\mathbf{u}_{c,0} P_{\text{MB}}(\mathbf{V}_{c,0}; M) P_{\text{MB}}(\mathbf{v}_{c,0}; m) P(\mathbf{u}_{c,0}) |\mathbf{v}_{c,0} - \mathbf{V}_{c,0}|}, \quad (2.8)$$

where $\langle x \rangle_{\text{coll}}$ denotes the statistical average of a variable x with respect to collisions. $P_{\text{MB}}(\mathbf{V}; M)$ and $P_{\text{MB}}(\mathbf{v}; m)$ are the Maxwell-Boltzmann velocity distributions:

$$P_{\text{MB}}(\mathbf{V}; M) = \left(\frac{\beta M}{2\pi} \right)^{3/2} \exp \left(-\frac{\beta M \mathbf{V}^2}{2} \right), \quad (2.9)$$

$$P_{\text{MB}}(\mathbf{v}; m) = \left(\frac{\beta m}{2\pi} \right)^{3/2} \exp \left(-\frac{\beta m \mathbf{v}^2}{2} \right). \quad (2.10)$$

$P(\mathbf{u}_{c,0})$ is the probability density of the direction vector from the target particle to the colliding gas particle at collision, and $|\mathbf{v}_{c,0} - \mathbf{V}_{c,0}|$ comes from the consequence that the collision frequency is proportional to the relative speed between the target particle and gas particle. From Equations (2.8) and (2.1), γ_1 becomes

$$\gamma_1 = 1 + \frac{2m}{M+m} \frac{\int d\mathbf{V}_{c,0} d\mathbf{v}_{c,0} d\mathbf{u}_{c,0} P_{\text{MB}}(\mathbf{V}_{c,0}; M) P_{\text{MB}}(\mathbf{v}_{c,0}; m) P(\mathbf{u}_{c,0}) |\mathbf{v}_{c,0} - \mathbf{V}_{c,0}| \mathbf{u}_{c,0} \cdot (\mathbf{v}_{c,0} - \mathbf{V}_{c,0}) \mathbf{u}_{c,0} \cdot \mathbf{V}_{c,0}}{\int d\mathbf{V}_{c,0} d\mathbf{v}_{c,0} d\mathbf{u}_{c,0} P_{\text{MB}}(\mathbf{V}_{c,0}; M) P_{\text{MB}}(\mathbf{v}_{c,0}; m) P(\mathbf{u}_{c,0}) |\mathbf{v}_{c,0} - \mathbf{V}_{c,0}| V_{c,0}^2}. \quad (2.11)$$

Introducing the total mass $m_t = M + m$, reduced mass $m_r = Mm/m_t$, relative velocity $\mathbf{v}_{\text{rel}} = \mathbf{v}_{c,0} - \mathbf{V}_{c,0}$, and center of mass velocity $\mathbf{v}_{\text{cent}} = (M\mathbf{V}_{c,0} + m\mathbf{v}_{c,0})/m_t$, Equation (2.11) reduces to

$$\gamma_1 = 1 + \frac{2m}{M+m} \frac{\int d\mathbf{v}_{\text{rel}} d\mathbf{v}_{\text{cent}} d\mathbf{u}_{c,0} P(\mathbf{u}_{c,0}) |\mathbf{v}_{\text{rel}}| (\mathbf{u}_{c,0} \cdot \mathbf{v}_{\text{rel}}) \mathbf{u}_{c,0} \cdot \left(\mathbf{v}_{\text{cent}} - \frac{m\mathbf{v}_{\text{rel}}}{m_t} \right) \exp \left[-\frac{\beta(m_t \mathbf{v}_{\text{cent}}^2 + m_r \mathbf{v}_{\text{rel}}^2)}{2} \right]}{\int d\mathbf{v}_{\text{cent}} d\mathbf{v}_{\text{rel}} d\mathbf{u}_{c,0} P(\mathbf{u}_{c,0}) |\mathbf{v}_{\text{rel}}| \left(\mathbf{v}_{\text{cent}} - \frac{m\mathbf{v}_{\text{rel}}}{m_t} \right)^2 \exp \left[-\frac{\beta(m_t \mathbf{v}_{\text{cent}}^2 + m_r \mathbf{v}_{\text{rel}}^2)}{2} \right]} \quad (2.12)$$

The integrand of the denominator of the second term on the right-hand side of Equation (2.12) is independent of $\mathbf{u}_{c,i}$. Therefore, the integration is straightforwardly performed as follows.

$$\begin{aligned} & \int d\mathbf{v}_{\text{cent}} d\mathbf{v}_{\text{rel}} d\mathbf{u}_{c,0} P(\mathbf{u}_{c,0}) |\mathbf{v}_{\text{rel}}| \left(\mathbf{v}_{\text{cent}} - \frac{m\mathbf{v}_{\text{rel}}}{m_t} \right)^2 \exp \left[-\frac{\beta(m_t \mathbf{v}_{\text{cent}}^2 + m_r \mathbf{v}_{\text{rel}}^2)}{2} \right] \\ &= \int d\mathbf{v}_{\text{cent}} d\mathbf{v}_{\text{rel}} |\mathbf{v}_{\text{rel}}| \left(\mathbf{v}_{\text{cent}} - \frac{m\mathbf{v}_{\text{rel}}}{m_t} \right)^2 \exp \left[-\frac{\beta(m_t \mathbf{v}_{\text{cent}}^2 + m_r \mathbf{v}_{\text{rel}}^2)}{2} \right] \\ &= \pi^{3/2} \left(\frac{2}{\beta} \right)^{9/2} \left(\frac{3}{m_t^{5/2} m_r^2} + \frac{4m^2}{m_t^{7/2} m_r^3} \right). \end{aligned} \quad (2.13)$$

For the calculation of the numerator of the second term on the right-hand side of Equation (2.12), an appropriate spherical coordinate is employed so that the relative velocity and direction vector are described as $\mathbf{v}_{\text{rel}} = (0, 0, v_{\text{rel}})$ and $\mathbf{u}_{c,0} = (\sin \theta \cos \phi, \sin \theta \sin \phi, \cos \theta)$, respectively. In this coordinate, the target particle is fixed at the origin, and the colliding gas particle moves along the vector parallel to $\mathbf{v}_{\text{rel}} = (0, 0, v_{\text{rel}})$, and the probability density of $\mathbf{u}_{c,0}$ is simply obtained from the geometrical considerations:

$$P(\mathbf{u}_{c,0}) \propto \sin \theta \cos \theta \Theta[\cos \theta]. \quad (2.14)$$

where Θ represents the Heaviside step function, implemented to preclude physically impossible collisions. Using $P(\mathbf{u}_{c,0})$, the numerator in Equation (2.12) is calculated as follows.

$$\begin{aligned} & \int d\mathbf{v}_{\text{cent}} d\mathbf{v}_{\text{rel}} d\mathbf{u}_{c,0} P(\mathbf{u}_{c,0}) |\mathbf{v}_{\text{rel}}| (\mathbf{u}_{c,0} \cdot \mathbf{v}_{\text{rel}}) \mathbf{u}_{c,0} \cdot \left(\mathbf{v}_{\text{cent}} - \frac{m\mathbf{v}_{\text{rel}}}{m_t} \right) \exp \left[-\frac{\beta(m_t \mathbf{v}_{\text{cent}}^2 + m_r \mathbf{v}_{\text{rel}}^2)}{2} \right] \\ &= -2\pi^{3/2} \left(\frac{2}{\beta} \right)^{9/2} \frac{m}{m_t^{5/2} m_r^3}. \end{aligned} \quad (2.15)$$

Combining Equations (2.8), (2.11), and (2.15), γ_1 is obtained as

$$\gamma_1 = \frac{3M}{3M + 4m}, \quad (2.16)$$

which does not become a negative value for any M .

Chapter 3

Fluctuating Diffusivity of Particle in Gas Mixtures: Numerical Study

Abstract

Dynamics of the binary gas mixture, where the fraction of one component is tiny, is numerically examined with various mass ratios. In this gas system, the minor particle exhibits fluctuating diffusivity, causing the Brownian yet non-Gaussian diffusion, when the minor particle is significantly lighter than that of the major particle. The observed fluctuating diffusivity originates from an origin, which has not been reported: the gap of the relaxation timescales between the velocity direction and speed.

3.1 Introduction

In 2009, a novel type of diffusion, termed Brownian yet non-Gaussian diffusion, was experimentally reported by Wang et al. [18]. Their investigations into colloidal particles moving along phospholipid bilayer tubes and diffusing within F-actin networks revealed that, although the mean squared displacement of the particles is proportional to time, the self-part of the van-Hove correlation function deviates from the Gaussian distribution. Since non-Gaussian diffusion was traditionally thought to occur with anomalous diffusion, the discovery by Wang et al. triggered the study of Brownian yet non-Gaussian diffusion from both experimental and theoretical sides. Following this discovery, Brownian yet non-Gaussian diffusion has been observed in various complex systems, including glass-forming liquids [42,90], colloidal suspensions [41,91] biological systems [18,26,27,85],

active matter [92, 93], and polymeric systems [24].

The Brownian yet non-Gaussian diffusion can be theoretically described using fluctuating diffusivity, which incorporates the effect of a diffusion coefficient that stochastically changes over time [24, 94–96]. It can be expressed through an over-damped Langevin equation with the fluctuating diffusion coefficient $D(t)$ as follows:

$$\dot{\mathbf{R}} = \sqrt{2D(t)}\boldsymbol{\xi}(t), \quad (3.1)$$

where $\mathbf{R}(t)$ is the position of the target particle, and $\boldsymbol{\xi}(t)$ the Gaussian white noise. The first and second moments of $\boldsymbol{\xi}(t)$ satisfy $\langle \boldsymbol{\xi}(t) \rangle = \mathbf{0}$ and $\langle \boldsymbol{\xi}(t) \cdot \boldsymbol{\xi}(t') \rangle = \mathbf{1}\delta(t - t')$, respectively. The stochastic process of the particle (Equation (3.1)) is determined if the stochastic process of $D(t)$ is provided [24, 42, 94, 96].

The origins of the observed fluctuating diffusivity can be classified into two mechanisms. The first pertains to the temporal/spatial environmental heterogeneity; particle mobility changes due to the heterogeneous nature of the environment. This mechanism manifests in cases where particles are immersed, for instance, in glass-forming liquids [17, 90], dense active matter [92, 93], biological systems [18, 26, 27, 85], or colloidal suspensions [41, 91]. The second origin is attributed to the internal degrees of freedom of the particles; in cases where the particle has a number of degrees of freedom, the particle conformation/orientation slowly varies, and the center of mass of particle diffusivity depends on the slow dynamics and fluctuates. This mechanism appears in entangled polymers, polymer solutions [24, 96], and rod-like particle solutions [25]. As such, it has been considered that the origins of fluctuating diffusivity are the fluctuations in the degrees of freedom related to the position of either the surrounding fluid molecules or the particles themselves.

In classical mechanics, the dynamics of particles depends not only on position but also on velocity. This raises a question: Is the fluctuating diffusivity solely attributable to the degrees of freedom concerning the position, such as temporal/spatial environmental heterogeneity or fluctuations in the internal degrees of freedom of the target particle? This chapter presents a new third origin of fluctuating diffusivity related to particle velocity by examining a simple gas system. Specifically, binary-gas mixtures where one component has a significantly small fraction are considered. All the gas particles are spherical in shape. Because the system is a gas state, there is no temporal/spatial environmental heterogeneity, and due to its spherical nature, there are no large number of internal degrees of freedom; the fluctuating diffusivity related to positional degrees of freedom cannot occur in this system. Nonetheless, this study demonstrates that the fluctuating diffusivity, which causes Brownian yet non-Gaussian diffusion, can manifest, thereby reporting a

previously undocumented origin. Further, the novel third origin is phenomenologically elucidated based on the simulation results.

3.2 Method

3.2.1 System Setting

The current system consists of a single molecule situated in the other gas molecule (hereafter called the minor and major molecule, respectively), which can be regarded as the model system for the binary gas mixture with the fraction of one component being tiny. The system is in an equilibrium state, and the inverse temperature is β . The mass of the minor molecule is M , and that of the major molecule is m . The diameter of the minor molecule is d_1 , and that of the major molecule is d_2 . The thermodynamic limit is considered: the system volume and number of particles are infinite while keeping the number density of the major molecule at ρ . The minor molecule moves ballistically until it collides with a major molecule. If the interparticle interaction between the minor and major molecule is the hard-core potential, the velocity of the minor molecule before and after a collision are related as follows:

$$\mathbf{V}_{c,i+1} = \mathbf{V}_{c,i} - \frac{2M}{m+M}(\mathbf{V}_{c,i+1} - \mathbf{v}_{c,i}) \cdot \mathbf{u}_{c,i} \mathbf{u}_{c,i}. \quad (3.2)$$

where $\mathbf{V}_{c,i}$ is the minor molecule velocity before i th collision, and $\mathbf{v}_{c,i}$ the colliding major molecule velocity at the i th collision. $\mathbf{u}_{c,i}$ means the unit vector connecting the minor molecule to the colliding major molecule.

In gas systems, the dynamics of the constituent particles can be approximately described using the Markovian stochastic process since the dynamics of the particles are not strongly correlated [11, 45]. Such an approximation is traditionally approved for the gas kinetic theory if the interest is not long-time tails in time correlation functions for some time-dependent variables. Upon the approximated description, the kinetic Monte Carlo (KMC) method can be employed to calculate the dynamics of the minor molecule situated in the major gas molecule. For implementing the KMC method, the collision statistics when and where the minor molecule collides with a major molecule is required. Such statistics, which can be the direct input into the KMC method, have not been calculated so far.

3.2.2 Collision Statistics

The required statistics is the probability density where the minor molecule for a given $\mathbf{V}_{c,i}$ collides with the major molecule having $\mathbf{v}_{c,i}$ at $\mathbf{u}_{c,i}$ with a free time $\Delta t_{c,i}$, $P(\mathbf{v}_{c,i}, \mathbf{u}_{c,i}, \Delta t_{c,i} | \mathbf{V}_{c,i})$, which is obtained based on the two assumptions;

1. The dynamics of minor molecule obey a Markovian stochastic process.
2. All the major molecule are always under an equilibrium state; the positions are uniformly distributed, and the statistics of velocity obey the Maxwell-Boltzmann distribution as follows:

$$P_{\text{MB}}(\mathbf{v}; m) = \left(\frac{\beta m}{2\pi}\right)^{3/2} \exp\left(-\frac{\beta m \mathbf{v}^2}{2}\right) \quad (3.3)$$

From the first and second assumptions, the collision frequency at which the minor molecule with $\mathbf{V}_{c,i}$ collides with a major molecule with velocity $\mathbf{v}_{c,i}$ is expressed as follows:

$$\rho d^2 (\mathbf{V}_{c,i} - \mathbf{v}_{c,i}) \cdot \mathbf{u}_{c,i} \Theta[(\mathbf{V}_{c,i} - \mathbf{v}_{c,i}) \cdot \mathbf{u}_{c,i}] \quad (3.4)$$

where $d = (d_1 + d_2)/2$ denotes the average of the diameters of the minor and major molecule, and Θ means the Heaviside step function, which can eliminate the collision at $(\mathbf{V}_{c,i} - \mathbf{v}_{c,i}) \cdot \mathbf{u}_{c,i} < 0$.

$P(\mathbf{v}_{c,i}, \mathbf{u}_{c,i}, \Delta t_{c,i}; \mathbf{V}_{c,i})$ can be interpreted as the product of the three factors; the first factor is the cumulative probability for the time interval of the target minor molecule for a given $\mathbf{V}_{c,i}$, the second factor is the probability density of the velocity of the colliding major molecule, and the third factor is the collision frequency of the minor molecule at the time interval $\Delta t_{c,i}$. For the calculation of the first factor, the probability density of $\Delta t_{c,i}$ is required:

$$P(\Delta t_{c,i} | \mathbf{V}_{c,i}) = \bar{\nu}(\mathbf{V}_{c,i}) \exp[-\bar{\nu}(\mathbf{V}_{c,i}) \Delta t_{c,i}], \quad (3.5)$$

where $\bar{\nu}(\mathbf{V}_{c,i})$ is the averaged collision rate of the minor molecule for a given $\mathbf{V}_{c,i}$ as follows:

$$\begin{aligned} \bar{\nu}(\mathbf{V}_{c,i}) &= \int d\mathbf{v}_{c,i} \int d\mathbf{u}_{c,i} \rho d^2 (\mathbf{v}_{c,i} - \mathbf{V}_{c,i}) \cdot \mathbf{u}_{c,i} \Theta[(\mathbf{v}_{c,i} - \mathbf{V}_{c,i}) \cdot \mathbf{u}_{c,i}] P_{\text{MB}}(\mathbf{v}_{c,i}; m) \\ &= \frac{\rho \pi d^2}{\sqrt{\chi}} \left[\left(\sqrt{\chi} |\mathbf{V}_{c,i}| + \frac{1}{2\sqrt{\chi} |\mathbf{V}_{c,i}|} \right) \text{erf}(\sqrt{\chi} |\mathbf{V}_{c,i}|) + \frac{1}{\sqrt{\pi}} \exp(-\chi |\mathbf{V}_{c,i}|^2) \right], \end{aligned} \quad (3.6)$$

where $\chi = \beta m/2$, and erf is the error function. The first factor is the probability that the minor molecule for a given $\mathbf{V}_{c,i}$ does not collides with any major molecule for a time interval $\Delta t_{c,i}$, which is obtained as

$$\Psi(\Delta t_{c,i} | \mathbf{V}_{c,i}) = \int_{\Delta t_{c,i}}^{\infty} d\Delta t'_{c,i} P(\Delta t'_{c,i} | \mathbf{V}_{c,i}) = \exp[-\bar{\nu}(\mathbf{V}_{c,i}) \Delta t_{c,i}] \quad (3.7)$$

The second and third factors are just described as Equations (3.3) and (3.4), respectively, due to the first and second assumptions. Combining Equations (3.4), (3.3), and (3.6), $P(\mathbf{v}_{c,i}, \mathbf{u}_{c,i}, \Delta t_{c,i} | \mathbf{V}_{c,i})$ is obtained as follows:

$$P(\mathbf{v}_{c,i}, \mathbf{u}_{c,i}, \Delta t_{c,i} | \mathbf{V}_{c,i}) = \rho d^2 (\mathbf{V}_{c,i} - \mathbf{v}_{c,i}) \cdot \mathbf{u}_{c,i} \Theta[(\mathbf{V}_{c,i} - \mathbf{v}_{c,i}) \cdot \mathbf{u}_{c,i}] \Psi(\Delta t_{c,i} | \mathbf{V}_{c,i}) P_{\text{MB}}(\mathbf{v}_{c,i}; m) \quad (3.8)$$

3.2.3 Kinetic Monte Carlo Method

In the Markovian nature, the dynamics of the minor molecule can be calculated based on Equations (3.2) and (3.8) using the kinetic Monte Carlo (KMC) method. The KMC method, initially developed for chemical reactions [97] and the Ising model [98], has since been applied to various other systems [99]. This work first extends the KMC method to treat the gas diffusion based on the collision statistics.

The initial velocity of the target particle $\mathbf{V}_{c,1}$ is sampled from the Maxwell-Boltzmann distribution:

$$P_{\text{MB}}(\mathbf{V}_{c,1}; M) = \left(\frac{\beta M}{2\pi} \right)^{3/2} \exp \left(-\frac{\beta M \mathbf{V}_{c,1}^2}{2} \right) \quad (3.9)$$

Since Equation (3.9) is just the Gaussian distribution, the initial velocity is stochastically sampled using the Box-Muller method. For the time development of the dynamics of the minor molecule, the collision time interval $\Delta t_{c,i}$, velocity of a colliding major molecule $\mathbf{v}_{c,i}$, and the direction unit vector at collision $\mathbf{u}_{c,i}$ are sampled from Equation (3.8). Meanwhile, simultaneous sampling is technically difficult, and Equation (3.8) is decomposed into several conditional probability densities as follows.

$$P(\mathbf{v}_{c,i}, \mathbf{u}_{c,i}, \Delta t_{c,i} | \mathbf{V}_{c,i}) = P(\mathbf{u}_{c,i} | \mathbf{v}_{c,i}, \Delta t_{c,i}, \mathbf{V}_{c,i}) P(\mathbf{v}_{c,i} | \Delta t_{c,i}, \mathbf{V}_{c,i}) P(\Delta t_{c,i} | \mathbf{V}_{c,i}) \quad (3.10)$$

where each $P(\mathbf{u}_{c,i} | \mathbf{v}_{c,i}, \Delta t_{c,i}, \mathbf{V}_{c,i})$, $P(\mathbf{v}_{c,i} | \Delta t_{c,i}, \mathbf{V}_{c,i})$, and $P(\Delta t_{c,i} | \mathbf{V}_{c,i})$ are obtained as follows.

$$P(\Delta t_{c,i} | \mathbf{V}_{c,i}) = \int d\mathbf{v}_{c,i} \int d\mathbf{u}_{c,i} P(\mathbf{v}_{c,i}, \mathbf{u}_{c,i}, \Delta t_{c,i} | \mathbf{V}_{c,i}) = \bar{\nu}(\mathbf{V}_{c,i}) \exp(-\bar{\nu}(\mathbf{V}_{c,i}) \Delta t_{c,i}) \quad (3.11)$$

$$P(\mathbf{v}_{c,i} | \Delta t_{c,i}, \mathbf{V}_{c,i}) = \int d\mathbf{u}_{c,i} \frac{P(\mathbf{v}_{c,i}, \mathbf{u}_{c,i}, \Delta t_{c,i} | \mathbf{V}_{c,i})}{P(\Delta t_{c,i} | \mathbf{V}_{c,i})} = \frac{\rho \pi d^2 |\mathbf{V}_{c,i} - \mathbf{v}_{c,i}| P_{\text{MB}}(\mathbf{v}_{c,i}; m)}{\bar{\nu}(\mathbf{V}_{c,i})} \quad (3.12)$$

$$\begin{aligned} P(\mathbf{u}_{c,i} | \mathbf{v}_{c,i}, \Delta t_{c,i}, \mathbf{V}_{c,i}) &= \frac{P(\mathbf{v}_{c,i}, \mathbf{u}_{c,i}, \Delta t_{c,i} | \mathbf{V}_{c,i})}{P(\mathbf{v}_{c,i} | \Delta t_{c,i}, \mathbf{V}_{c,i}) P(\Delta t_{c,i} | \mathbf{V}_{c,i})} \\ &= \frac{(\mathbf{v}_{c,i} - \mathbf{V}_{c,i}) \cdot \mathbf{u}_{c,i}}{\pi |\mathbf{v}_{c,i} - \mathbf{V}_{c,i}|} \Theta[(\mathbf{v}_{c,i} - \mathbf{V}_{c,i}) \cdot \mathbf{u}_{c,i}] \end{aligned} \quad (3.13)$$

From Equations (3.11), (3.12), and (3.13), $\Delta t_{c,i}$, $\mathbf{v}_{c,i}$, and $\mathbf{u}_{c,i}$ are sampled. Since Equation (3.11) is the exponential function, $\Delta t_{c,i}$ is straightforwardly sampled using the inversion method. Here,

sampling $\mathbf{v}_{c,i}$ is relatively complicated because it is a vector with three components. For this calculation, Equation (3.12) is expressed using the relative velocity $\mathbf{v}_r = \mathbf{v}_{c,i} - \mathbf{V}_{c,i}$ with the spherical coordinates v_r , $\theta \in [0, \pi]$, and $\phi \in [0, 2\pi)$: $\mathbf{v}_r = v_r \cos \phi \sin \theta \hat{\mathbf{x}} + v_r \sin \phi \sin \theta \hat{\mathbf{y}} + v_r \cos \theta \hat{\mathbf{z}}$ with $\hat{\mathbf{x}}$, $\hat{\mathbf{y}}$, and $\hat{\mathbf{z}}$ being the orthogonal basis vectors in the Cartesian coordinate. Without loss of generality, $\hat{\mathbf{z}}$ is set as $\hat{\mathbf{z}} = \mathbf{V}_{c,i}/|\mathbf{V}_{c,i}|$. In this spherical coordinate, Equation (3.12) is displayed as

$$P(v_r, \theta, \phi | \Delta t_{c,i}, \mathbf{V}_{c,i}) = \frac{\rho \pi d^2 v_r^3 \sin \theta}{\bar{v}(\mathbf{V}_{c,i})} \left(\frac{\beta m}{2\pi} \right)^{3/2} \exp \left[-\frac{\beta m (v_r^2 + |\mathbf{V}_{c,i}|^2 + v_r |\mathbf{V}_{c,i}| \cos \theta)}{2} \right] \quad (3.14)$$

Since Equation (3.14) does not include ϕ , ϕ is sampled from the uniform distribution for the range $\phi \in [0, 2\pi)$. The conditional probability density of v_r is obtained as the integration of Equation (3.14) over θ and ϕ as follows:

$$\begin{aligned} P(v_r | \Delta t_{c,i}, \mathbf{V}_{c,i}) &= \int d\theta \int d\phi P(v_r, \theta, \phi | \Delta t_{c,i}, \mathbf{V}_{c,i}) \\ &= \left[\left(\frac{\beta m}{2\pi} \right)^{3/2} \frac{4\pi \rho \pi d^2 \sin \theta}{|\mathbf{V}_{c,i}| \bar{v}(\mathbf{V}_{c,i})} \exp \left(-\frac{\beta m |\mathbf{V}_{c,i}|^2}{2} \right) \right] v_r^2 \exp \left[-\frac{\beta m v_r^2}{2} \right] \sinh (|\mathbf{V}_{c,i}| v_r) \end{aligned} \quad (3.15)$$

From Equation (3.15), v_r is sampled using the rejection method. The conditional probability density of θ is represented as

$$\begin{aligned} P(\theta | v_r, \phi, \Delta t_{c,i}, \mathbf{V}_{c,i}) &= \int d\phi \frac{P(v_r, \theta, \phi | \Delta t_{c,i}, \mathbf{V}_{c,i})}{P(v_r | \Delta t_{c,i}, \mathbf{V}_{c,i})} \\ &= \left[\frac{|\mathbf{V}_{c,i}| v_r}{2 \sinh (|\mathbf{V}_{c,i}| v_r)} \right] \sin \theta \exp(-v_r |\mathbf{V}_{c,i}| \cos \theta) \end{aligned} \quad (3.16)$$

θ is sampled from Equation (3.16) by the inversion method. Combining v_r , θ , and ϕ , $\mathbf{v}_{c,i}$ is obtained. Also for sampling $\mathbf{u}_{c,i}$ from Equation (3.13), the spherical coordinate with $\theta' \in [0, \pi]$ and $\phi' \in [0, 2\pi)$ is employed: $\mathbf{u}_{c,i} = \cos \phi' \sin \theta' \hat{\mathbf{x}}' + \sin \phi' \sin \theta' \hat{\mathbf{y}}' + \cos \theta' \hat{\mathbf{z}}'$ with $\hat{\mathbf{x}}'$, $\hat{\mathbf{y}}'$, and $\hat{\mathbf{z}}'$ being the orthogonal basis vectors and $\hat{\mathbf{x}}'$ set along $\hat{\mathbf{z}}' = \mathbf{v}_r/|v_r|$. In this coordinate, Equation (3.13) is expressed as

$$P(\theta', \phi' | \mathbf{v}_{c,i}, \Delta t_{c,i}, \mathbf{V}_{c,i}) = \frac{1}{\pi} \cos \theta' \sin \theta' \Theta[v_r \cos \theta'] \quad (3.17)$$

Since Equation (3.17) is independent of ϕ' , ϕ' is sampled from the uniform distribution ranged $\phi' \in [0, 2\pi)$. From Equation (3.17), The probability density of θ is obtained by the integration over ϕ' as

$$P(\theta' | \mathbf{v}_{c,i}, \Delta t_{c,i}, \mathbf{V}_{c,i}) = \int d\phi' P(\theta', \phi' | \mathbf{v}_{c,i}, \Delta t_{c,i}, \mathbf{V}_{c,i}) = 2 \cos \theta' \sin \theta' \Theta[v_r \cos \theta'] \quad (3.18)$$

From Equation (3.18), θ' is sampled from the inversion method. The unit vector $\mathbf{u}_{c,i}$ at collision is constructed from the obtained θ' and ϕ' .

Based on the collision statistics $P(\mathbf{v}_{c,i}, \mathbf{u}_{c,i}, \Delta t_{c,i} | \mathbf{V}_{c,i})$ and the rule of the velocity change (Equation (3.2)), the dynamics of the minor molecule is calculated as follows:

1. The initial velocity is sampled from the Maxwell-Boltzmann distribution, as described in Equation (3.9).
2. The collision time interval, $\Delta t_{c,i}$, the velocity of the colliding major molecule, $\mathbf{v}_{c,i}$, and the direction unit vector connecting from the minor molecule to the colliding major molecule, $\mathbf{u}_{c,i}$ are sampled based on the collision statistics $P(\mathbf{v}_{c,i}, \mathbf{u}_{c,i}, \Delta t_{c,i} | \mathbf{V}_{c,i})$, using each conditional probability densities.
3. The velocity of the minor molecule changes using $\mathbf{v}_{c,i}$ and $\mathbf{u}_{c,i}$, based on Equation (3.2).

From this algorithm, the time sequence of the velocity of the minor molecule is obtained, as illustrated in Figure 3.1. The position of the minor molecule at time t , $\mathbf{R}(t)$, are straightforwardly produced from the time sequence of the velocities $\{\mathbf{V}_{c,i}\}$. Based on this algorithm, the following results are obtained. Here, it should be emphasized that the collision statistics $P(\mathbf{v}_{c,i}, \mathbf{u}_{c,i}, \Delta t_{c,i} | \mathbf{V}_{c,i})$ is independent of the particle position and time. Thus, the environment surrounding the target minor molecule is always statistically homogeneous; environmental heterogeneity, one of the origins of the fluctuating diffusivity, can not occur in the current system. In the current system, if the mass of the major molecule, m , the inverse temperature, β , and a characteristic length ρd^2 are chosen to define the dimensionless units, the dynamics of the minor molecule depends only on the mass of the minor molecule, M , while the following variables are displayed with the dimensions for the physical clarity.

3.3 Results

3.3.1 Fluctuating Diffusivity in Gas

Figure 3.2 displays the mean square displacement of the minor molecule defined as $\langle \Delta \mathbf{R}(\Delta t)^2 \rangle$, where $\Delta \mathbf{R}(\Delta t)$ is the displacement for the time lag Δt as $\Delta \mathbf{R}(\Delta t) = \mathbf{R}(\Delta t) - \mathbf{R}(0)$. For comparison, the prediction by the Enskog theory [9, 79] is also plotted:

$$\langle \Delta \mathbf{R}(\Delta t)^2 \rangle = \frac{6\tau_{\text{MSD}}^2}{\beta M} \left[-1 + \frac{\Delta t}{\tau_{\text{MSD}}} + \exp\left(-\frac{\Delta t}{\tau_{\text{MSD}}}\right) \right], \quad (3.19)$$

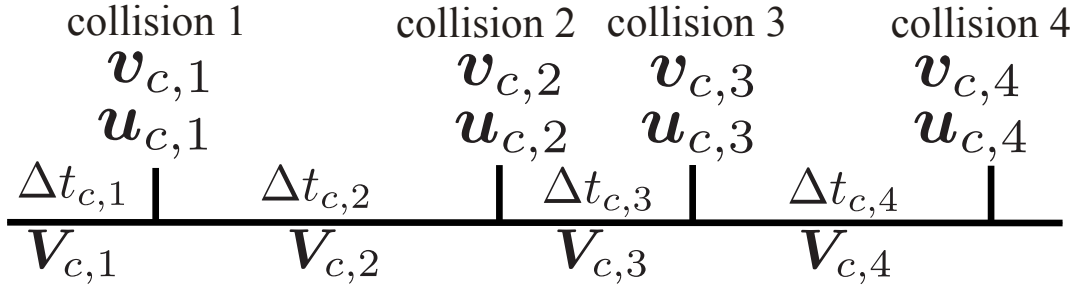


Figure 3.1: Schematic illustration of the time development of the particle velocity $\mathbf{V}_{c,i}$. The minor molecule collides with a major molecule with the velocity $\mathbf{v}_{c,i}$ at the direction $\mathbf{u}_{c,i}$ for the collision time interval $\Delta t_{c,i}$.

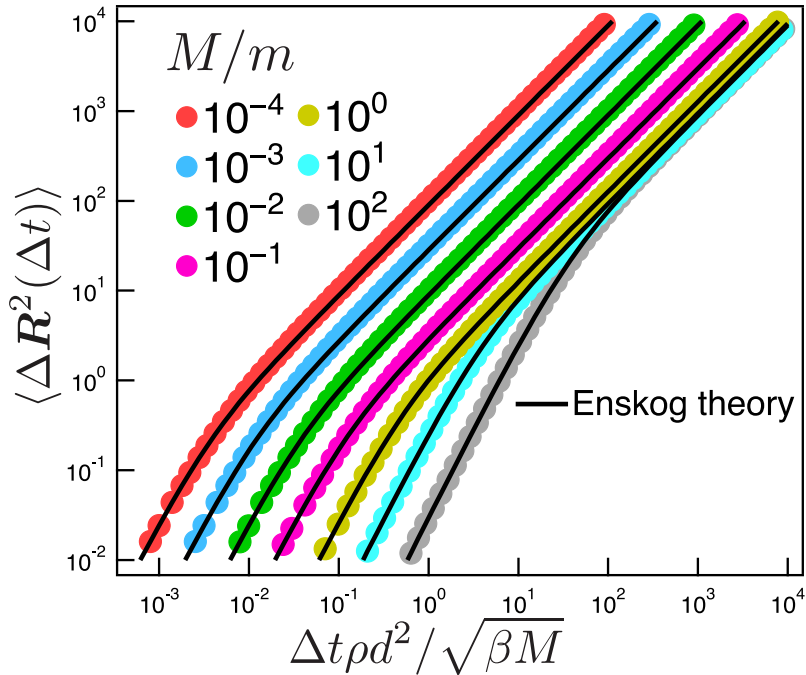


Figure 3.2: Mean square displacement of the minor molecule with various mass ratios M/m . The symbols describe the result from the KMC simulations, and the black curves are the predictions of the Enskog theory (Equation (3.19)).

where τ_{MSD} is the crossover time from the ballistic $\langle \Delta \mathbf{R}(\Delta t)^2 \rangle \propto \Delta t^2$ to the diffusive $\langle \Delta \mathbf{R}(\Delta t)^2 \rangle \propto \Delta t^1$ regimes defined as

$$\tau_{\text{MSD}} = \frac{3}{8\rho d^2} \sqrt{\frac{\beta M(m+M)}{2\pi m}}. \quad (3.20)$$

The results from the KMC simulations show simple ballistic and diffusive behaviors for any mass ratio M/m . These behaviors are almost perfectly consistent with Equation (3.19).

Although the mean square displacement of the minor molecule is simple, the trajectory of the minor molecule shows intriguing behavior. Figure 3.3 displays the representative trajectories of the minor molecule for the large and small mass ratios, $M/m = 10^2$ and 10^{-4} . The observation time is $T = 10^6 \tau_{\text{MSD}}$, and the three-dimensional trajectories are projected onto the two-dimensional XY plane for visibility. The color of the trajectories means the magnitude of the displacement scaled by the root of the mean square displacement for a time lag $\Delta t = 10\tau_{\text{MSD}}$. When the minor molecule is heavy $M/m = 10^2$, the fast (red) and slow (blue) parts are homogeneously distributed, and it is the simple Brownian motion where the diffusion coefficient is constant. Meanwhile, when the minor molecule is lightweight $M/m = 10^{-4}$, large clusters of fast and slow areas appear. This result suggests that the dynamics of the minor molecule are not simple when M/m is small. In the following, the results are displayed for the typical mass ratios $M/m = 10^2$ and 10^{-4} as the representative instances for the simple and unusual diffusion, respectively. Data for other mass ratios are summarized in Appendix 3.A.

To examine the heterogeneous dynamics shown in Figure 3.3, the self-part of the van-Hove correlation functions, defined as $G_s(\Delta X, \Delta t) = \langle \delta[\Delta X - (X(t + \Delta t) - X(t))] \rangle$ with X being the position of the minor molecule along x axis, are computed. Figure 3.4 shows $G_s(\Delta X, \Delta t)$ with the various scaled time lag $\Delta t/\tau_{\text{MSD}}$ for the large and small mass ratios $M/m = (a)10^2$ and 10^{-4} . If the particle mass is heavy ($M/m = 10^2$), $G_s(\Delta X, \Delta t)$ is almost the Gaussian distribution for the simulated Δt . In contrast, when the minor molecule is lightweight ($M/m = 10^{-4}$), $G_s(\Delta X, \Delta t)$ deviates from the Gaussian distribution within the intermediate time lag $10^1 \lesssim \Delta t/\tau_{\text{MSD}} \lesssim 10^4$, while $G_s(\Delta X, \Delta t)$ converges to the Gaussian distribution for a long time scale $\Delta t/\tau_{\text{MSD}} \gtrsim 10^5$. Intriguingly, for $M/m = 10^{-4}$, the deviation from the Gaussian distribution occurs at the timescale where the mean square displacement exhibits the normal diffusion as shown in Figure 3.2. Similar behaviors are also observed for the other small mass cases, $M/m < 1$, as displayed in Figure 3.9 in Appendix 3.A. These results indicate that the Brownian yet non-Gaussian diffusion emerges even in the gas system composed of spherical particles, which do not essentially have any heterogeneous environments and a large number of internal degrees of freedom. To characterize the

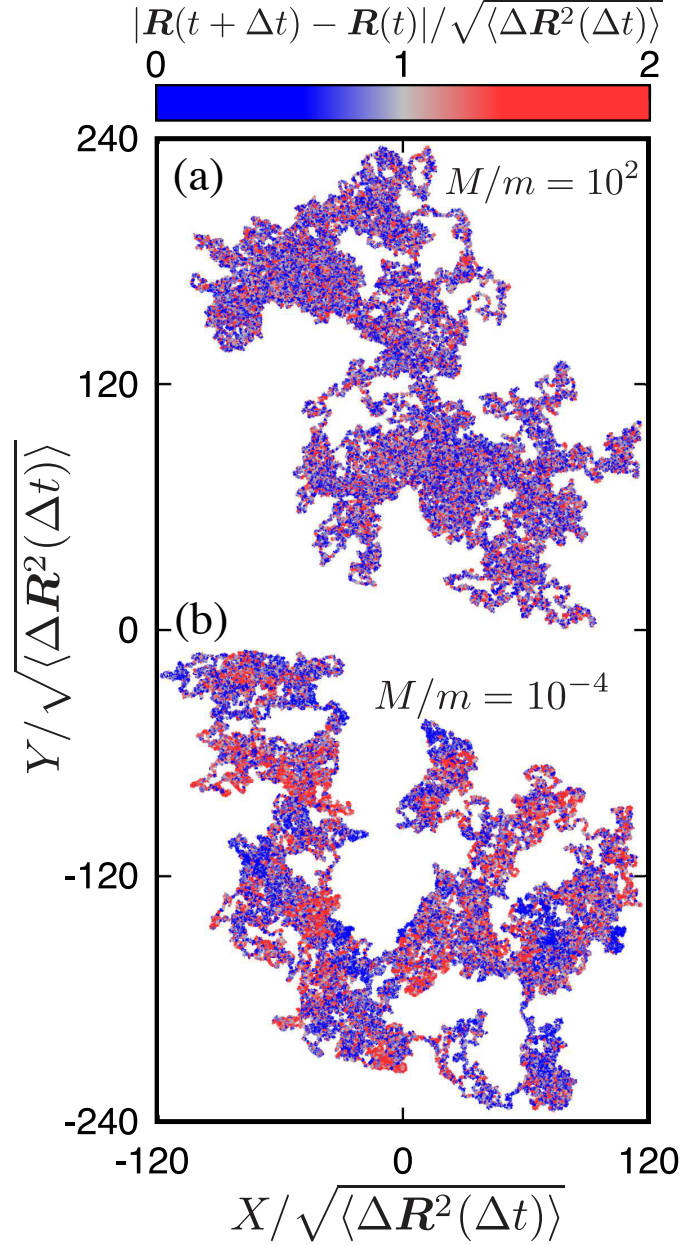


Figure 3.3: Trajectories of minor molecule during the observation time $T = 10^6 \tau_{\text{MSD}}$ with the mass ratios $M/m =$ (a) 10^2 and (b) 10^{-4} , obtained from the KMC simulations. The three-dimensional dynamics is projected onto the XY plane. The color indicates the displacement scaled by the mean square displacement with $|\mathbf{R}(\Delta t) - \mathbf{R}(0)| / \sqrt{\langle \Delta \mathbf{R}^2(\Delta t) \rangle}$ with Δt set to be $10\tau_{\text{MSD}}$.

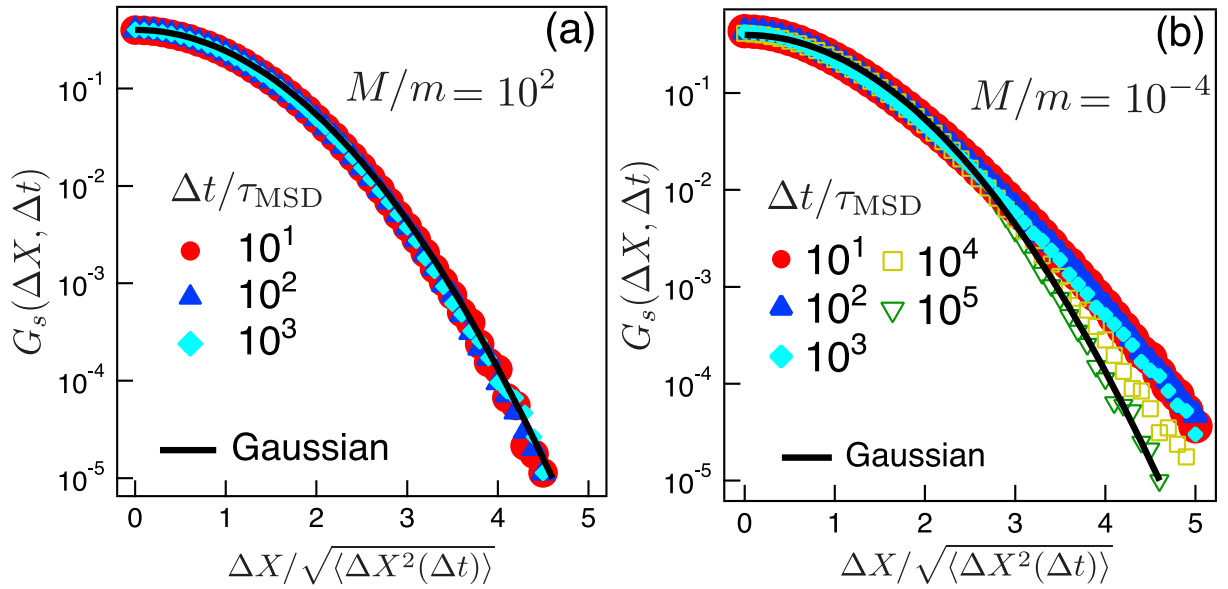


Figure 3.4: Self-part of the van-Hove correlation functions of the minor molecule, defined as $G_s(\Delta X, \Delta t) = \langle \delta[\Delta X - (X(t + \Delta t) - X(t))] \rangle$, obtained from the KMC simulations. The representative mass ratios $M/m =$ (a) 10^2 and (b) 10^{-4} for the various scaled time lag $\Delta t / \tau_{\text{MSD}}$ are displayed. For comparison, the horizontal axes are scaled using the root of mean square displacement $\sqrt{\langle \Delta X^2(\Delta t) \rangle}$, and the Gaussian distribution is also displayed by the black curve.

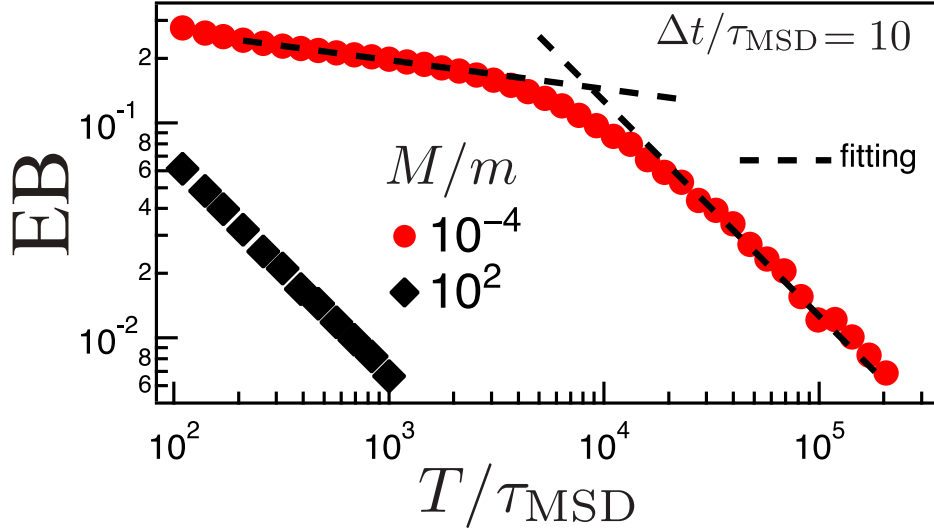


Figure 3.5: Ergodicity breaking (EB) parameters against the scaled observation time T/τ_{MSD} with the representative minor molecule masses, $M/m = 10^2$ and 10^{-4} , obtained from the KMC simulations. The time lag is set to be $\Delta t/\tau_{\text{MSD}} = 10$. The dotted lines are the fitting results with the power exponent functions $\text{EB} \propto T^{-\kappa}$ and T^{-1} for the short and long time scales, respectively.

non-Gaussianity, the non-Gaussian parameter [89], defined as $\langle 3\Delta\mathbf{R}^4(\Delta t) \rangle / \langle 5\Delta\mathbf{R}^2(\Delta t) \rangle^2 - 1$, is often analyzed. The non-Gaussian parameter becomes 0 when $G_s(\Delta X, \Delta t)$ is the Gaussian distribution, while it deviates from 0 for the non-Gaussian distribution. As displayed in Figure 3.10, the non-negligible deviations of the non-Gaussian parameter from 0 are observed when the mass ratio is small ($M/m < 1$).

The Brownian yet non-Gaussian diffusion has been considered to be attributed to the temporal change of the diffusion coefficient of the particle, called the fluctuating diffusivity. To characterize the fluctuating diffusivity, the following ergodicity breaking parameter is often computed:

$$\text{EB}(\Delta t, T) = \frac{\langle [\bar{\delta}^2(\Delta t, T)]^2 \rangle}{\langle \bar{\delta}^2(\Delta t, T) \rangle^2} - 1, \quad (3.21)$$

where $\bar{\delta}^2(\Delta t, T)$ expresses the time-averaged mean square displacement for the time lag Δt with the observation time T , defined as

$$\bar{\delta}^2(\Delta t, T) = \frac{1}{T - \Delta t} \int_0^{T-\Delta t} [\mathbf{R}(t + \Delta t) - \mathbf{R}(t)]^2 dt. \quad (3.22)$$

For $T \gg \Delta t$, the dependence of the EB parameter on Δt was theoretically proven to be weak [24]. In the current work, the time lag is set to be $\Delta t/\tau_{\text{MSD}} = 10$, and EB parameter is calculated

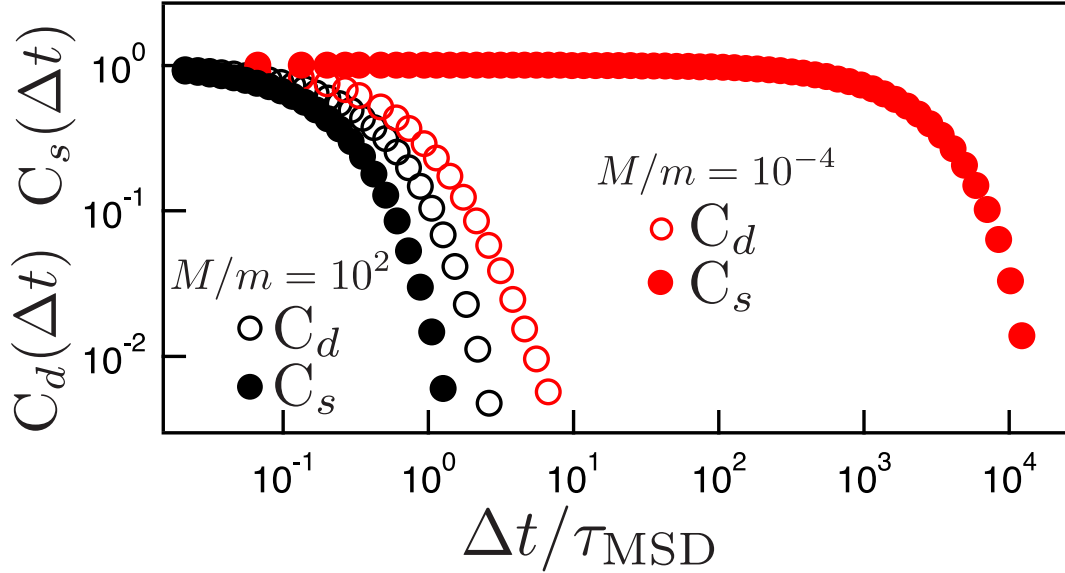


Figure 3.6: Time-correlation function of the velocity direction $C_d(\Delta t)$ and speed $C_s(\Delta t)$, defined as Equation (3.23) and (3.24), respectively. The data for the representative mass $M/m = 10^2$ and 10^{-4} are calculated by the KMC simulations.

for the observation time $T/\tau_{\text{MSD}} \geq 10^2$, which is larger than the time lag. Figure 3.5 shows the EB parameter against the scaled observation time T/τ_{MSD} with the representative mass ratios. For the large mass $M/m = 10^2$, the EB parameter decays as $\text{EB} \propto T^{-1}$. This result means that the dynamics of the minor molecule is just the Gaussian process. Meanwhile, when the minor molecule is lightweight ($M/m = 10^{-4}$), the EB parameter exhibits shoulder before the timescale of Gaussian decay $\text{EB} \propto T^{-1}$. Similar behaviors are also observed for other small mass cases $M/m < 1$, as displayed in Figure 3.11 in Appendix 3.A. From Equation (3.21), the EB parameter can be interpreted as the variance of the diffusion coefficient for the diffusive time regime $\Delta t/\tau_{\text{MSD}} \gg 1$. Thus, the observation of the shoulder in the EB parameter means the emergence of fluctuating diffusivity. The crossover time scale from the shoulder to the Gaussian decay, τ_{EB} , can be interpreted as the characteristic timescale of the fluctuating diffusivity. $\tau_{\text{EB}}/\tau_{\text{MSD}}$ can be roughly estimated as $\tau_{\text{EB}}/\tau_{\text{MSD}} \sim 10^4$ from the cross point of the two power exponent fitting functions $\text{EB} \propto T^{-\kappa}$ with $\kappa \in [0, 1)$ and T^{-1} at the short and long time regimes, respectively. The timescale $\tau_{\text{EB}}/\tau_{\text{MSD}} \sim 10^4$ is approximately equal to the timescale where the van-Hove correlation function $G(\Delta X, \Delta t)$ approaches Gaussian distribution as shown in Figure 3.4(b). Also, the large fluctuation of the displacement observed in Figure 3.3 can be interpreted as the emergence of the fluctuating diffusivity.

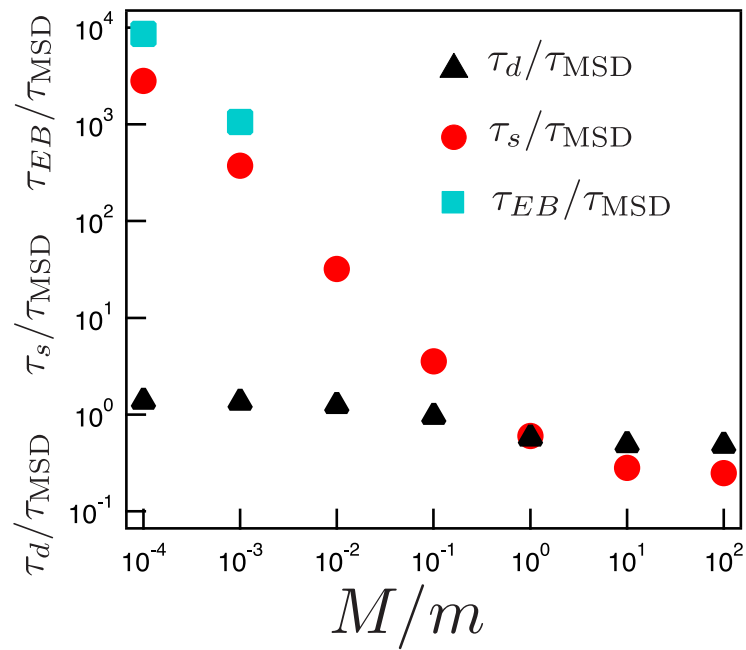


Figure 3.7: Relaxation times of the velocity direction τ_d and speed τ_s of the minor molecule as a function of mass ratio M/m , defined in Equations (3.25), obtained from the KMC simulations. The horizontal axis is scaled by τ_{MSD} . For comparison, the crossover timescales of the ergodicity breaking parameter τ_{EB} , calculated using the curve fittings, are also displayed.

3.3.2 Origin of Fluctuating Diffusivity

In the results above, the fluctuating diffusivity is observed for a timescale longer than τ_{MSD} , even in the gas systems. The current system does not have any heterogeneous nature and a large number of internal degrees of freedom, which are the known origins for the fluctuating diffusivity. A novel mechanism should be considered to elucidate the origin of the fluctuating diffusivity in the gas system. When the mass of the minor molecule is sufficiently smaller than that of the major molecule, $M/m \ll 1$, the speed of the minor molecule is statistically larger than that of the major molecule due to the Maxwell-Boltzmann velocity distribution (Equation (3.9)), i.e., $|\mathbf{V}| \gg |\mathbf{v}|$. In this condition, the motion of the minor molecule seems to be that in immobile obstacles like a Lorentz gas system [69, 71, 100] within a short timescale. In such a case, the direction of the velocity is randomized via a single collision, while the speed of the minor molecule is almost unchanged. From this consideration, it is expected that the relaxation time of the minor molecule speed is sufficiently larger than that of the direction of the velocity. This slow relaxation of the speed is possibly related to the fluctuating diffusivity, which occurs in the timescale larger than τ_{MSD} . Possible time-correlation functions of the velocity direction $C_d(\Delta t)$ and speed $C_s(\Delta t)$ are the followings:

$$C_d(\Delta t) = \left\langle \frac{\mathbf{V}(\Delta t)}{|\mathbf{V}(\Delta t)|} \cdot \frac{\mathbf{V}(0)}{|\mathbf{V}(0)|} \right\rangle, \quad (3.23)$$

$$C_s(\Delta t) = \frac{\langle |\mathbf{V}(\Delta t)| |\mathbf{V}(0)| \rangle - \langle |\mathbf{V}| \rangle^2}{\langle |\mathbf{V}|^2 \rangle - \langle |\mathbf{V}| \rangle^2}. \quad (3.24)$$

From the definitions, both functions $C_d(\Delta t)$ and $C_s(\Delta t)$ becomes 1 at the initial time, $\Delta t = 0$, and approaches 0 at $\Delta t \rightarrow \infty$. Figure 3.6 displays $C_d(\Delta t)$ and $C_s(\Delta t)$ against $\Delta t/\tau_{\text{MSD}}$ with the representative masses M/m from the KMC simulations. When the mass of the minor molecule is large ($M/m = 10^2$), $C_d(\Delta t)$ and $C_s(\Delta t)$ decays with a similar timescale, $\Delta t/\tau_{\text{MSD}} \sim 1$. This means that both the velocity direction and speed of the minor molecule relaxes at the crossover time τ_{MSD} in the mean square displacement. In contrast, for the small mass cases $M/m = 10^{-4}$, the relaxation time of $C_s(\Delta t)$ is significantly larger than that of $C_d(\Delta t)$. This result indicates the speed of the minor molecule persists for a long timescale while the velocity direction rapidly changes. Similar behaviors are commonly observed for the small mass cases, as represented in Figures 3.12 and 3.13 in Appendix 3.A. Here, possible definitions of the relaxation timescales of

$C_d(\Delta t)$ and $C_s(\Delta t)$, τ_d and τ_s , are the followings:

$$\tau_{d/s} = \frac{\int_0^\infty d\Delta t \Delta t C_{d/s}(\Delta t)}{\int_0^\infty d\Delta t C_{d/s}(\Delta t)} \quad (3.25)$$

From Equation (3.25), the relaxation times τ_d and τ_s are computed and shown in Figure 3.7, as a function of the mass ratio M/m . For comparison, the crossover time of the ergodicity breaking parameter, estimated from the curve fittings in Figure 3.11, is also displayed (clear crossover is observed when the minor molecule mass is sufficiently small, $M/m \leq 10^{-3}$, and only such a data are analyzed). Figure 3.7 shows that τ_d/τ_{MSD} is approximately 1 for the simulated M/ms . Meanwhile, τ_s/τ_{MSD} becomes significantly large quantities at the small mass regime $M/m \ll 1$. Intriguingly, τ_s/τ_{MSD} at the small M/m regime is almost the same order against τ_{EB} . This result implies that the fluctuating diffusivity observed in the current gas mixture is attributed to the slow relaxation of the speed of the minor molecule.

The results presented suggest a plausible explanation for the observed fluctuating diffusivity in the studied binary gas mixture, especially when the mass ratio of the minor molecule, M/m , is significantly smaller than unity. Within the intermediate time scale defined as $\tau_d \lesssim T \lesssim \tau_s$, the diffusion of the minor molecule occurs due to the random alterations in its velocity direction. In this timescale, the speed of the minor molecule does not almost change, indicated by $|\mathbf{V}(t)| \approx V$, allowing for the representation of the diffusion coefficient as a constant function, expressed as $D(t) = D(V)$. As the time scale extends to $T \gtrsim \tau_s$, temporary fluctuations in $D(t)$ emerge from the variations in $|V(t)|$. When observing this long time scale, the fluctuation of the diffusivity is averaged and then becomes less prominent, leading to the emergence of Gaussian normal diffusion characterized by an effective diffusion coefficient, denoted as $D_{\text{eff}} = \langle D \rangle$. The underlying cause of the observed fluctuating diffusivity in the current system is attributed to the distinct timescale separation in the relaxation timescales of the velocity direction and speed of the molecules. Furthermore, this scenario accounts for the clusters depicted in Figure 3.3, which are indicative of the slow relaxation of the speed of the minor molecule over the timescale τ_s .

To check the validity of the proposed model, a theoretical evaluation of the van-Hove correlation function for the minor molecule under the condition $M/m \ll 1$ is performed. During the intermediate timescale $\tau_d \lesssim T \lesssim \tau_s$, the behavior of a minor molecule would be approximately modeled as a moving particle in dilute fixed spherical obstacles. Here, the diffusion coefficient is described using the speed $|V(t)|$ as the expression $D(|\mathbf{V}(t)|) = |\mathbf{V}(t)|/3\pi\rho d^2$ [11]. The displacement probability density for the minor molecule within the timescale $\tau_d \lesssim T \lesssim \tau_s$, moving at speed

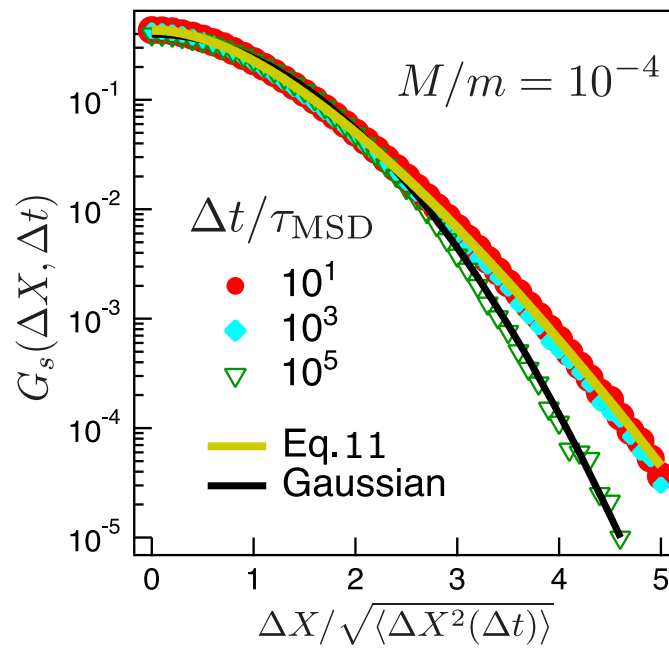


Figure 3.8: Theoretical prediction for the scaled self-part of the van-Hove correlation function, $G_s(\Delta X, \Delta t)$, pertaining to minor molecule, represented by an ochre curve. This is compared against the kinetic Monte Carlo (KMC) simulation results, demonstrated using distinct symbols for varying time lags, under the condition $M/m = 10^{-4}$, as displayed in Figure 3.4(b). Additionally, for reference, the Gaussian distribution is depicted with a black curve.

$V = |\mathbf{V}|$, follows a Gaussian distribution.

$$P(\Delta X; \Delta t | V) = \frac{1}{\sqrt{4\pi D(V)\Delta t}} \exp\left(-\frac{\Delta X^2}{4D(V)\Delta t}\right). \quad (3.26)$$

At equilibrium, the distribution of the minor molecule speed V follows the Maxwell-Boltzmann distribution: $P_{\text{MB}}(V) = 4\pi V^2 (2\pi)^{-3/2} \exp(-V^2/2)$. Integrating Equation (3.26) over V , considering its equilibrium distribution, yields the van-Hove correlation function $G_s(\Delta X, \Delta t)$ for the intermediate timescale $\tau_d \lesssim \Delta t \lesssim \tau_s$:

$$G_s(\Delta X; \Delta t) = \int_0^\infty dV P(\Delta X; \Delta t | V) P_{\text{MB}}(V). \quad (3.27)$$

Numerical calculation of Equation (3.27), depicted in Figure 3.4, reveals a reasonable concordance with the results from the kinetic Monte Carlo (KMC) simulations for the intermediate timescale. This supports the hypothesis that fluctuating diffusivity in this system is a consequence of different relaxation timescales between velocity direction and speed. Deviations from Gaussian distribution in $G_s(\Delta X; \Delta t)$, commonly observed in various systems, are evident. The non-Gaussian tail in Equation (3.27) can be approximated using the saddle point method:

$$G_s(\Delta X; \Delta t) = \sqrt{\frac{3}{4\pi}} \frac{|\Delta X|}{\Delta t} \exp\left[-3 \left(\frac{3\Delta X^2}{8\sqrt{2}\Delta t}\right)^{\frac{2}{3}}\right] \quad (\text{for } \Delta X \gg 1). \quad (3.28)$$

This result indicates that the tail behavior differs from the exponential or stretched Gaussian distributions frequently observed in glass-forming liquids [17, 23, 101, 102] and certain biological systems [26, 27, 92–94].

3.4 Discussion

The behavior of minor molecule, when its mass ratio is much smaller than that of the major molecule ($M/m \ll 1$), can be considered to be akin to the particle in the Lorenz gas model, as detailed in several studies [11, 71, 103–105]. The Lorenz gas model is a well-studied dynamic model representing a single gas particle moving among spatially fixed obstacles. In this model, only the direction of the particle velocity changes, while its speed remains constant at any timescale. Therefore, the fluctuating diffusivity observed in the current system does not emerge for the conventional Lorenz gas systems.

The obtained results indicate that in situations where the difference in mass is significantly large, $M/m \ll 1$, fluctuating diffusivity can appear. Currently, there are no experimental studies

documenting non-Gaussian behavior or fluctuating diffusivity in gaseous systems. However, it can be speculated that such phenomena could be observed in experiments for binary gas mixtures. For example, in a mixture of helium and radon [106], the mass ratio is approximately $M/m \approx 0.018$. In cases with this mass ratio, it is likely that Brownian yet non-Gaussian diffusion, which is a result of fluctuating diffusivity, will occur, as demonstrated in Figure 3.10 in Appendix. It is anticipated that this non-Gaussian behavior could be detected with detailed and accurate measurements. While the kinetics of gases [9] are often thought to be well understood, this study suggests that there may still be aspects that are not fully understood.

3.5 Summary

In this chapter, a new origin of fluctuating diffusivity was discovered. This origin is distinct from previously known origins, such as environmental heterogeneity or changes in particle conformations. The fluctuating diffusivity can emerge in simple binary gas mixtures with differences in mass and fraction, particularly when the mass of the minor component is much smaller than that of the major component. This study demonstrated that the fluctuating diffusivity results from the gap in the relaxation time scales between the velocity direction and speed of the minor component molecule. These findings will provide a novel path to model fluctuating diffusivity and fresh insights into the kinetic behavior of gas systems. It is hoped that the non-Gaussian behavior and fluctuating diffusivity predicted in this study will be verified through elaborate experiments.

3.A Additional Simulation Data

In Chapter 3, the simulation data are displayed only for the representative mass ratios $M/m = 10^2$ and 10^4 for visibility. The other mass ratio cases ranged from $M/m = 10^{-4}$ to 10^2 are shown in this Appendix 3.A. The self-part of the van-Hove correlation functions $G(\Delta X, \Delta t)$ against displacement with various time lags $\Delta t/\tau_{\text{MSD}}$ are displayed in Figure 3.4. The non-Gaussian parameter against time lag $\Delta t/\tau_{\text{MSD}}$ with various mass ratios M/m are shown in Figure 3.10. The ergodicity breaking (EB) parameters against the scaled observation time T/τ_{MSD} with various mass ratios are displayed in Figure 3.11. The time-correlation functions of the velocity direction $C_d(\Delta t)$ and speed $C_s(\Delta t)$ of the minor molecule, defined as Equations (3.23) and (3.24), are displayed in Figures 3.12 and 3.13, respectively, with the various mass ratios M/m .

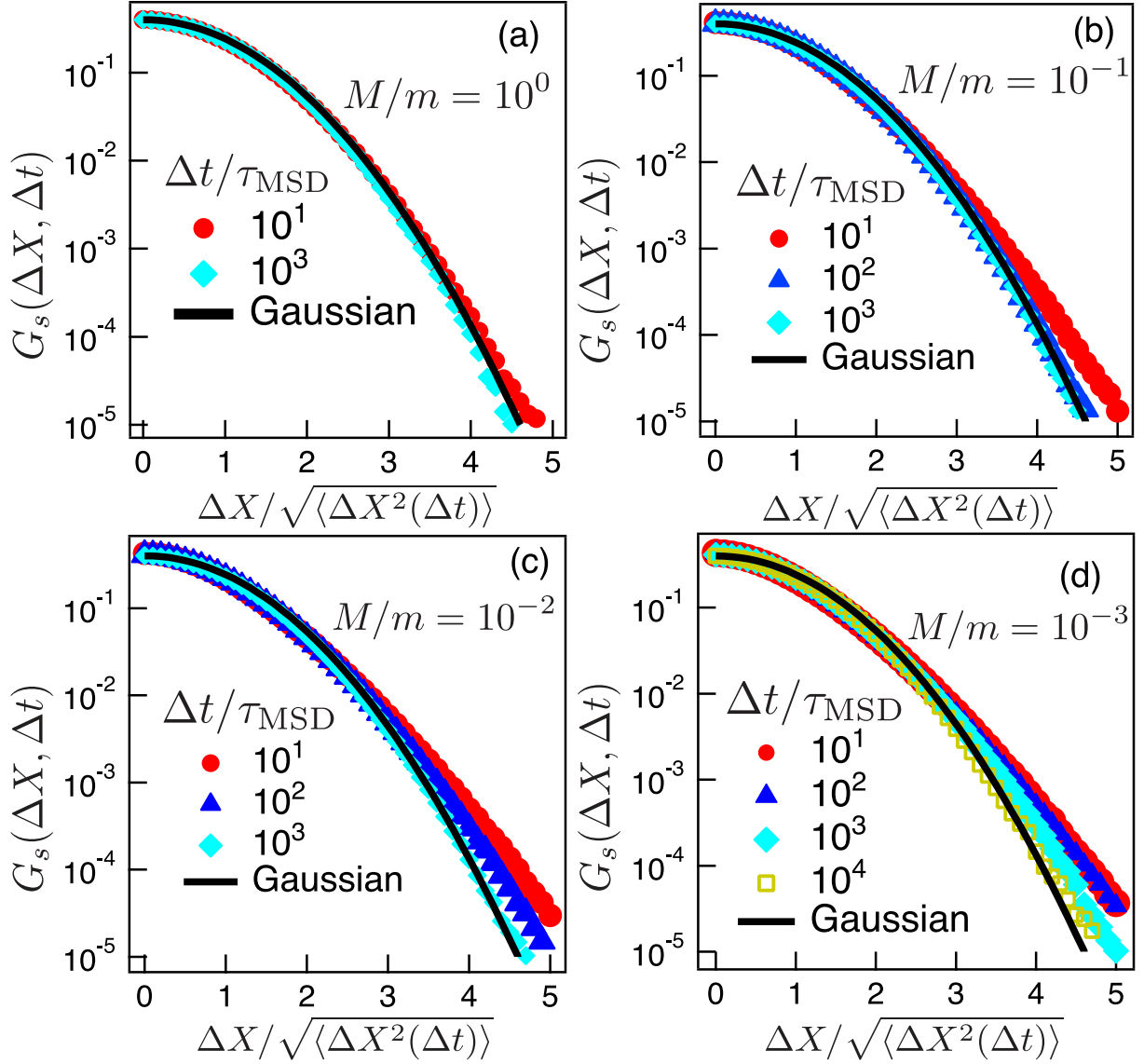


Figure 3.9: Self-part of the van-Hove correlation functions of the minor molecule with the mass ratios $M/m =$ (a) 10^0 , (b) 10^{-1} , (c) 10^{-2} , and (d) 10^{-3} from the KMC simulations. The horizontal axis is scaled using the root of mean square displacement $\sqrt{\langle \Delta X^2(\Delta t) \rangle}$. The black curves are represented for comparisons with the simulation data.

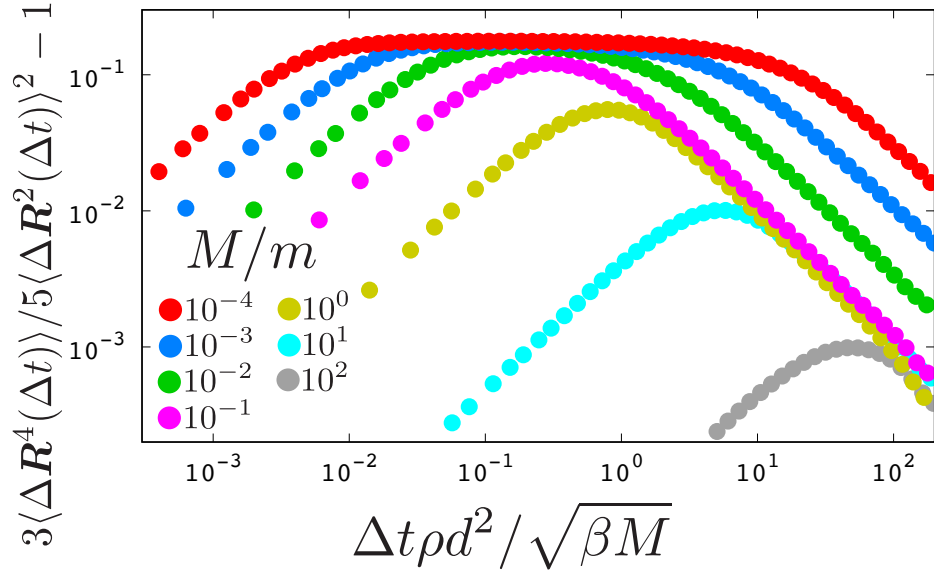


Figure 3.10: Non-Gaussian parameters of the minor molecule defined as $\langle 3\Delta\mathbf{R}^4(\Delta t) \rangle / 5\langle \Delta\mathbf{R}^2(\Delta t) \rangle^2 - 1$ with various mass ratios M/m , obtained from the KMC simulations.

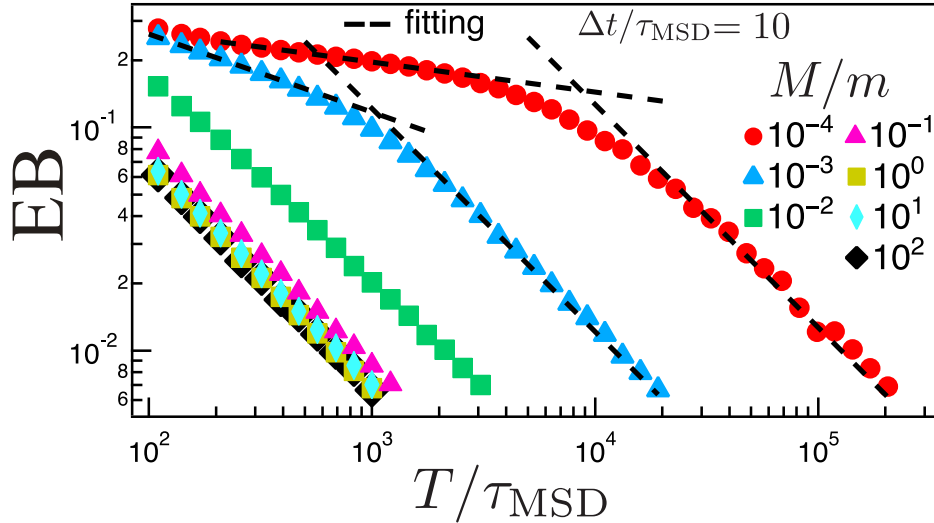


Figure 3.11: Ergodicity breaking (EB) parameters as the function of the scaled observation time T/τ_{MSD} with the various mass ratios, $M/m = 10^2$ and 10^{-4} , calculated from the KMC simulations. The time lag is chosen as $\Delta t/\tau_{\text{MSD}} = 10$. The dotted lines are the fitting results with the power exponent functions $\text{EB} \propto T^{-\kappa}$ and T^{-1} for the short and long time scales, respectively.

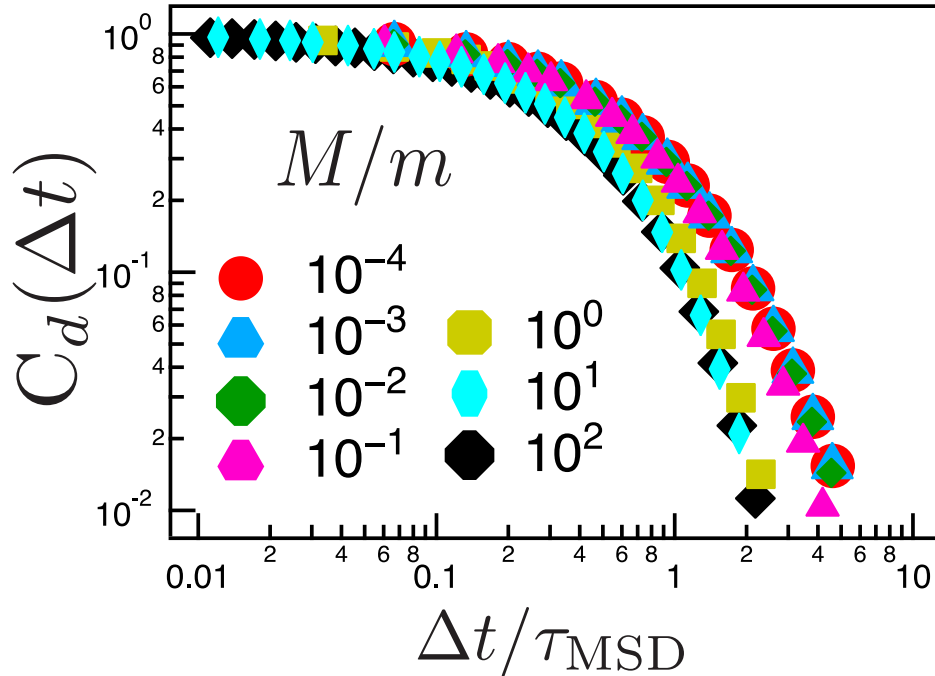


Figure 3.12: Time-correlation functions for the velocity direction of the minor molecule, defined as Equation (3.23), with the various mass ratios M/m , obtained from the KMC simulations.

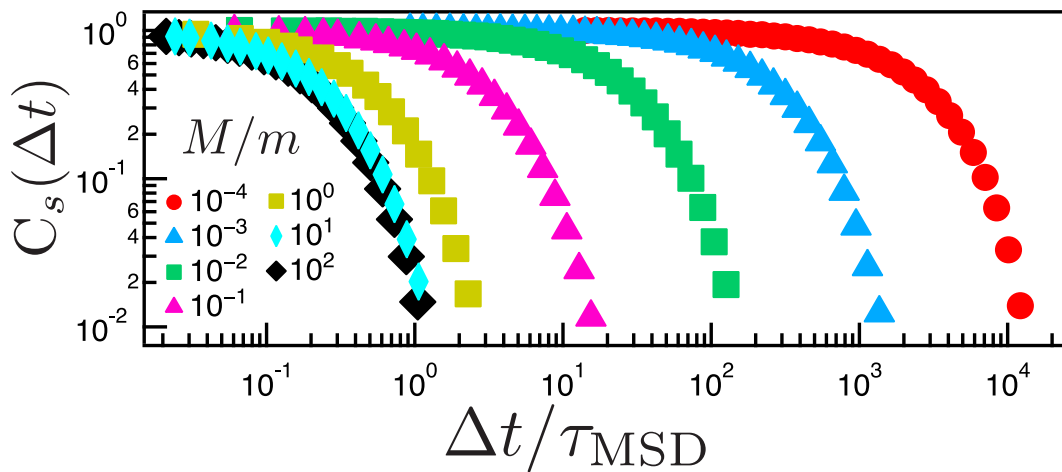


Figure 3.13: Time-correlation functions for the speed of the minor molecule, defined as Equation (3.24), with the various mass ratios M/m , obtained from the KMC simulations.

Chapter 4

Fluctuating Diffusivity of Particle in Gas Mixtures: Theoretical Study

Abstract

The theoretical analyses for the Brownian yet non-Gaussian diffusion observed for a minor lightweight particle diffusing in the binary gas mixtures is performed based on the Lorentz gas, consisting of a moving particle situated in fixed point obstacles. For the Lorentz gas model, the mean square displacement and non-Gaussian parameter are computed using the point process, and they do not show the Brownian yet non-Gaussian diffusion since the speed of the mobile particle remains unchanged. To incorporate the effect that the minor particle takes various speeds, the canonical ensemble averages for the correlation functions of the Lorentz gas are analytically calculated. The averaged results exhibit the Brownian yet non-Gaussian diffusion, which is quantitatively consistent with the numerical results for the binary gas mixture.

4.1 Introduction

Gas diffusion is a classical problem in statistical mechanics, and has been considered to be well-understood [9–11, 107]. However, Chapter 3 presents that the gas system can exhibit a non-trivial non-Gaussian diffusion. The numerical simulations revealed that a lightweight particle situated in heavy gas particles exhibits the Brownian yet non-Gaussian diffusion; the mean square displacement increases linearly against time, $\langle \Delta \mathbf{R}^2(\Delta t) \rangle \propto \Delta t$, while the self part of the van-Hove correlation function deviates from the Gaussian statistics. (Here, it should be noted that the non-

Gaussian diffusion often accompanies the anomalous diffusion $\langle \Delta \mathbf{R}^2(\Delta t) \rangle \propto \Delta t^\kappa$ ($\kappa \neq 1$), which is observed in glass former [23] or polymeric liquids [22]. Such a non-linear non-Gaussian diffusion is beyond the scope of this chapter.) The Brownian yet non-Gaussian diffusion has been considered to be attributed to two known origins: the first is the heterogeneous environment like glass-forming liquids [23, 85, 108], biological systems [18, 26, 27], active matter [92, 93], or colloidal suspensions [41, 91, 109], and the second is the fluctuation of the internal degrees of freedom appearing in polymer melts or rod-shaped particles [24, 25]. The gas mixture investigated in Chapter 3 has neither environmental heterogeneities nor conformational fluctuations. The observed Brownian yet non-Gaussian diffusion originates from a novel origin concerning the velocity degree of freedom of the minor particle: the separation of the relaxation timescales between the velocity direction and speed of the minor particle. Namely, In the spherical coordinates, the angle components in the velocity rapidly relax, while the radial component correlates for a longer timescale.

The dynamics of a light particle among heavier ones has frequently been modeled using the Lorentz gas models [11, 71, 103, 110]. This model consists of a single mobile particle navigating through a field of spatially fixed particles. Initially developed to represent the behavior of an electron in a metal, the Lorentz gas model has been broadly applied as a simple representation for transport phenomena in gases [103] and for certain classical dynamical systems [111, 112]. This model has been instrumental in analyzing various properties like diffusion coefficients [71, 113] and velocity relaxation [71, 103]. Moreover, numerous extended models of the Lorentz gas have been extensively explored [111, 112, 114]. Intuitively, one might anticipate that the diffusion of a light gas particle in heavier particles could be effectively described using the Lorentz gas model. However, the relationship between the basic, dilute Lorentz gas and the diffusion of a light particle in a matrix of heavier gas particles remains unclear. Additionally, whether the Lorentz gas model can accurately account for the non-Gaussian behavior in such gas systems is also uncertain.

This chapter conducts a theoretical analysis of the diffusion behavior of a light gas particle moving through a medium of heavier gas particles in an equilibrium state. To model the Brownian yet non-Gaussian diffusion observed in this medium, the random dilute Lorentz gas model is utilized. This chapter begins with deriving analytical representations for both the mean square displacement (MSD) and the non-Gaussian parameter for the Lorentz gas. These derivations are based on the framework of the point process [115]. Subsequent to the derivation of these analytical expressions, their ensemble averages over the initial speed of the minor particle, which follows the Maxwell-Boltzmann distribution, are analytically calculated. This averaged result quantitatively aligns with the observed Brownian yet non-Gaussian diffusion of a lightweight and minor gas

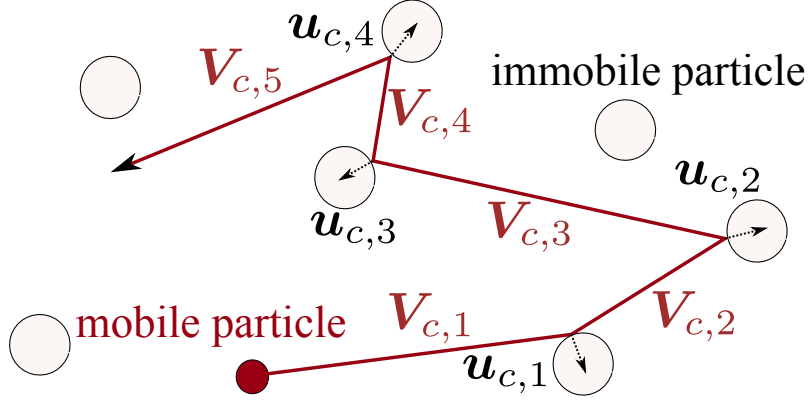


Figure 4.1: Illustration of the Lorentz gas system, consisting of the single mobile particle, depicted as a red point particle, immersed in the fixed spherical particles. The velocity of the mobile particle after the i th collision is denoted as $\mathbf{v}_{c,i}$. $\mathbf{u}_{c,i}$ means the unit vector directed from the mobile particle towards the colliding fixed particle at the i th collision.

particle in binary gas mixtures, except for a long timescale.

4.2 Theoretical Analyses

4.2.1 Model Setting

The system is comprised of a mobile point particle with size zero situated in fixed spherical obstacles with the radius σ . The mass of the mobile particle is denoted as M , which is required for the current issue, while the dynamics of the conventional Lorentz gas does not depend on M . This work is limited to the situation where the fixed particles are infinitely diluted, while such a simple situation is enough to describe the Brownian yet non-Gaussian diffusion. The fixed particles are randomly situated in the three-dimensional space with a uniform distribution. The number density of the fixed particles is described as ρ . In the fixed particles, the mobile particle moves ballistically until it collides with a fixed particle. Based on the hard-core potential [11], the velocity of the mobile particle instantaneously changes at the collision. The velocity of the mobile particle after the i th collision $\mathbf{V}_{c,i+1}$ is expressed using that before the collision $\mathbf{V}_{c,i}$ as follows:

$$\mathbf{V}_{c,i+1} = (\mathbf{1} - 2\mathbf{u}_{c,i}\mathbf{u}_{c,i}) \cdot \mathbf{V}_{c,i} \quad (4.1)$$

where $\mathbf{u}_{c,i}$ denotes the direction vector from the mobile particle to the colliding fixed particle, and $\mathbf{1}$ means the unit tensor. Figure 4.1 schematically illustrates the current model. From Equation (4.1),

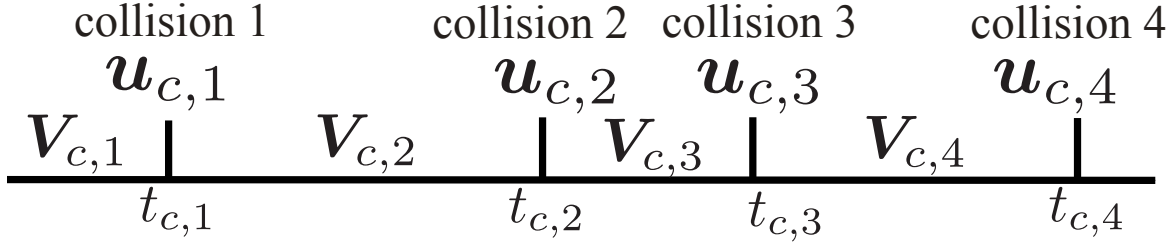


Figure 4.2: Illustration of the time sequence of the variables, concerning the dynamics of the mobile particle. The mobile particle with the velocity $\mathbf{V}_{c,i}$ collides with a fixed particle at the time $t_{c,i}$ and the direction vector $\mathbf{u}_{c,i}$ at the i th collision.

the speed of the mobile particle V remains unchanged, i.e., $V = |\mathbf{V}_{c,i}|$ for any i . In the dilute obstacle case, successive collisions are safely assumed to be uncorrelated if the long time-tails in time-correlation functions are not examined. Namely, the dynamics of the mobile particle can be described as a Markovian stochastic process. When dimensionless units are defined using M , V , and $\rho\sigma^2$, the Lorentz gas model for the dilute case has no parameters.

The Lorentz gas model has been regarded as a simplified representation of the minor and lightweight particles in the binary gas mixture [11, 12]. For the gas mixture, the speed (or the kinetic energy) of the minor particle is not constant even when the minor particle is sufficiently lightweight. However, the speed of the minor particle can be approximated as a constant within the relaxation timescale of the speed, which can be significantly larger than that of the velocity direction as shown in Chapter 3. Later, the relation between the Lorentz gas model and binary gas mixture is also discussed.

4.2.2 Correlation Function of Lorentz Gas

The dynamics of a moving particle is characterized by its velocities $\{\mathbf{V}_{c,i}\}$ and the times at the collision $\{t_{c,i}\}$. The position of this particle at time lag Δt following the n th collision, denoted as $\Delta\mathbf{R}(n, \Delta t)$, is given by:

$$\Delta\mathbf{R}(n, \Delta t) = \mathbf{V}_{c,n+1}(\Delta t - t_{c,n}) + \sum_{i=1}^n \mathbf{V}_{c,i}(t_{c,i} - t_{c,i-1}), \quad (4.2)$$

where $t_{c,0} = 0$, which is arbitrary chosen. For clarity, the time sequence of the variables is illustrated in Figure 4.2. To calculate the dynamics of the particle, the collision statistics for the single collision between the mobile and a fixed particle is required. In the current model, the collision frequency density $\nu(\mathbf{u}_{c,i})$, as a function of the direction unit vector at the i th collision $\mathbf{u}_{c,i}$, completely

characterizes the collision statistics. $\nu(\mathbf{u}_{c,i})$ is derived from the collision statistics of a binary gas mixture [2] under the assumption that the mass of the velocity of the surrounding gas particle is zero:

$$\nu(\mathbf{u}_{c,i}) = \rho\sigma^2 \mathbf{V}_{c,i} \cdot \mathbf{u}_{c,i} \Theta(\mathbf{V}_{c,i} \cdot \mathbf{u}_{c,i}), \quad (4.3)$$

with $\Theta(x)$ representing the Heaviside step function. Equation (4.3) can be further simplified using spherical coordinates. By setting the Cartesian coordinates of the mobile particle velocity as $\mathbf{V}_{c,i} = (0, 0, v)$ and representing $\mathbf{u}_{c,i}$ as $\mathbf{u}_{c,i} = (\sin \theta_i \cos \phi_i, \sin \theta_i \sin \phi_i, \cos \theta_i)$, where θ_i is in the range $[0, \pi/2]$ and ϕ_i is in $[0, 2\pi)$, the equation simplifies to:

$$\nu(\mathbf{u}_{c,i}) = \rho\sigma^2 V \cos \theta_i. \quad (4.4)$$

Integrating Equation (4.4) over the variable $\mathbf{u}_{c,i}$ leads to the total collision frequency, expressed as:

$$\int \nu(\mathbf{u}_{c,i}) d\mathbf{u}_{c,i} = \frac{V}{\lambda}, \quad (4.5)$$

where λ , defined as $1/\pi\rho\sigma^2$, represents the mean free path of the particle. By combining Equations (4.4) and (4.5), one can derive the probability density for the event where the mobile particle collides at the direction of $\mathbf{u}_{c,i}$ at the time interval $t_{c,i} - t_{c,i-1}$, given a specific speed V . This probability density, $P(t_{c,i} - t_{c,i-1}, \mathbf{u}_{c,i}; V)$, is formulated as:

$$P(t_{c,i} - t_{c,i-1}, \mathbf{u}_{c,i}; V) = \nu(\mathbf{u}_{c,i}) \exp\left[-\frac{V}{\lambda}(t_{c,i} - t_{c,i-1})\right]. \quad (4.6)$$

From Equation (4.6), the probability density at a time lag Δt for a given number of collisions n and speed V is obtained as follows:

$$P(\Delta \mathbf{R}, \{\mathbf{u}_{c,i}\}, \{t_{c,i}\}; n, \Delta t, v) = \delta[\Delta \mathbf{R} - \Delta \mathbf{R}(n, \Delta t)] \prod_{i=1}^{n+1} P(t_{c,i} - t_{c,i-1}, \mathbf{u}_{c,i}; V), \quad (4.7)$$

here the time lag should be within $t_{c,i} < \Delta t < t_{c,i+1}$. Further, integrating Equation (4.7) over all $\{\mathbf{u}_{c,i}\}$ and $\{t_{c,i}\}$ sets, the probability density for $\Delta \mathbf{R}$ with n , Δt , and V is given as:

$$\begin{aligned} P(\Delta \mathbf{R}; n, \Delta t, V) &= \int d\mathbf{V}_1 \int_{\Delta t}^{\infty} dt_{c,n+1} \int_0^{\Delta t} dt_{c,n} \int_0^{t_{c,n}} dt_{c,n-1} \cdots \int_0^{t_{c,2}} dt_{c,1} \\ &\quad \times \int d\mathbf{u}_{c,n+1} \cdots \int d\mathbf{u}_{c,1} P(\Delta \mathbf{R}, \{\mathbf{u}_{c,i}\}, \{t_{c,i}\}; n, \Delta t, V) P(\mathbf{V}_1) \\ &= e^{-V\Delta t/\lambda} \int d\mathbf{V}_1 \int_0^{\Delta t} dt_{c,n} \int_0^{t_{c,n}} dt_{c,n-1} \cdots \int_0^{t_{c,2}} dt_{c,1} \\ &\quad \times \int d\mathbf{u}_{c,n} \cdots \int d\mathbf{u}_{c,1} \delta[\Delta \mathbf{R} - \Delta \mathbf{R}(n, \Delta t)] \prod_{i=1}^n \nu(\mathbf{u}_{c,i}) P(\mathbf{V}_1; V), \end{aligned} \quad (4.8)$$

where $P(\mathbf{V}_1; V) = \delta(|\mathbf{V}_1| - V)/4\pi V^2$ denotes the initial velocity distribution of the mobile particle. To advance the calculation, a characteristic function is introduced:

$$C(\mathbf{k}; n, \Delta t, V) = \int d\Delta\mathbf{R} e^{i\mathbf{k}\cdot\Delta\mathbf{R}} P(\Delta\mathbf{R}; n, \Delta t, V) \quad (4.9)$$

Utilizing Equation (4.8), the characteristic function $C(\mathbf{k}; n, \Delta t, V)$ can be computed as follows:

$$\begin{aligned} & C(\mathbf{k}; n, \Delta t, V) \\ &= e^{-V\Delta t/\lambda} \int d\mathbf{V}_1 \int_0^{\Delta t} dt_{c,n} \int_0^{t_{c,n}} dt_{c,n-1} \cdots \int_0^{t_{c,2}} dt_{c,1} \int d\mathbf{u}_{c,n} \cdots \int d\mathbf{u}_{c,1} \\ & \times \prod_{i=1}^n \nu(\mathbf{u}_{c,i}) P(\mathbf{V}_1; V) \exp \left\{ i\mathbf{k} \cdot \left[\mathbf{V}_{c,n}(\Delta t - t_{c,n}) + \sum_{i=1}^n \mathbf{V}_{c,i}(t_{c,i} - t_{c,i-1}) \right] \right\}. \end{aligned} \quad (4.10)$$

Considering the Laplace transform of Equation (4.10), denoted as

$$\hat{C}(\mathbf{k}; n, s, V) = \mathcal{L}C(\mathbf{k}; n, \cdot, V) = \int_0^\infty d\Delta t e^{-\Delta t s} C(\mathbf{k}; n, \Delta t, V), \quad (4.11)$$

the following equation is obtained:

$$\hat{C}(\mathbf{k}; n, s, V) = \int d\mathbf{V}_1 \frac{P(\mathbf{V}_1; V)}{s - i\mathbf{k} \cdot \mathbf{V}_1 + V/\lambda} \prod_{i=1}^n \int d\mathbf{u}_{c,i} \frac{\nu(\mathbf{u}_{c,i})}{s - i\mathbf{k} \cdot \mathbf{V}_{c,i+1} + V/\lambda}. \quad (4.12)$$

This integration over \mathbf{V}_1 and $\{\mathbf{u}_{c,i}\}$ is analytically obtained as

$$\hat{C}(\mathbf{k}; n, s, V) = \frac{\lambda}{V} \left[\frac{1}{k\lambda} \arctan \left(\frac{kV}{s + V/\lambda} \right) \right]^{n+1}, \quad (4.13)$$

here $k = |\mathbf{k}|$. The Fourier-Laplace transform of the total probability density of $\Delta\mathbf{R}$ for a given V is computed as the sum of the probability density of $\Delta\mathbf{R}$ at the specific n (Equation (4.13)) over the collision number n : $\hat{C}(\mathbf{k}; s, V) = \sum_{n=0}^\infty \hat{C}(\mathbf{k}; n, s, V)$. The result of this calculation is

$$\hat{C}(\mathbf{k}; s, V) = \frac{\arctan \left(\frac{kV}{s + V/\lambda} \right)}{(V/\lambda) \left[k\lambda - \arctan \left(\frac{kV}{s + V/\lambda} \right) \right]}. \quad (4.14)$$

Equation (4.14) is the Fourier-Laplace transform of the self part of the van Hove correlation function. Any time-correlation function of the mobile particle can be straightforwardly calculated. It is noteworthy that Equation (4.14) satisfies the normalization condition of the probability density: $\hat{C}(\mathbf{k}; s, V) = s^{-1}$ at $|\mathbf{k}| \rightarrow 0$.

MSD is derived as the second-order moment of the van Hove correlation function. Based on Equation (4.14), the Laplace transform of the MSD for a given V is computed as the following expression:

$$\mathcal{L}[\langle \Delta \mathbf{R}^2(\cdot) \rangle_V](s) = - \left. \frac{\partial^2}{\partial \mathbf{k}^2} \hat{C}(\mathbf{k}; s, V) \right|_{\mathbf{k}=\mathbf{0}} = \frac{2V^2}{s^2(s + V/\lambda)}, \quad (4.15)$$

where $\langle \dots \rangle_V$ represents the statistical average for a given V . The fourth-order moment of the Laplace transform is also calculated as follows.

$$\mathcal{L}[\langle \Delta \mathbf{R}^4(\cdot) \rangle_V](s) = \left. \frac{\partial^2}{\partial \mathbf{k}^2} \frac{\partial^2}{\partial \mathbf{k}^2} \hat{C}(\mathbf{k}; s, V) \right|_{\mathbf{k}=\mathbf{0}} = \frac{8V^4(9s + 5V/\lambda)}{3s^3(s + V/\lambda)^3}. \quad (4.16)$$

The inverse Laplace transforms of Equations (4.15) and (4.16) are:

$$\frac{\langle \Delta \mathbf{R}^2(t) \rangle_V}{\lambda^2} = 2(-1 + V\Delta t/\lambda + e^{-V\Delta t/\lambda}), \quad (4.17)$$

$$\frac{\langle \Delta \mathbf{R}^4(t) \rangle_V}{\lambda^4} = \frac{4V^2\Delta t^2}{3\lambda^2} (5 + 4e^{-V\Delta t/\lambda}) - \frac{8V\Delta t}{\lambda} (2 - e^{-V\Delta t/\lambda}) + 8(1 - e^{-V\Delta t/\lambda}). \quad (4.18)$$

At the short time lag limit, $\Delta t \rightarrow 0$, Equations (4.17) and (4.18) are simplified as $\langle \Delta \mathbf{R}^2(\Delta t) \rangle_V \rightarrow V^2\Delta t^2$ and $\langle \Delta \mathbf{R}^4(\Delta t) \rangle_V \rightarrow V^4\Delta t^4$, respectively. This indicates just the ballistic motion at the short timescale. Conversely, in the long-time scale, $\Delta tV/\lambda \gg 1$, MSD converges to $\langle \Delta \mathbf{R}^2(\Delta t) \rangle_V \rightarrow 2V\lambda\Delta t$, which is the normal diffusion. From the definition of the diffusion coefficient $\langle \Delta \mathbf{R}^2(\Delta t; V) \rangle = 6D\Delta t$, D is calculated as $D = V\lambda/3$. This result aligns with the established finding in gas kinetic theory [11]. Furthermore, using Equations (4.17) and (4.18), the non-Gaussian parameter (NGP) under a given velocity V , $\alpha(\Delta t; V)$, is derived as follows:

$$\begin{aligned} \alpha(\Delta t; V) &= \frac{3\langle \Delta \mathbf{R}^4(\Delta t) \rangle_V}{5\langle \Delta \mathbf{R}^2(\Delta t) \rangle_V^2} - 1 \\ &= \frac{4e^{-V\Delta t/\lambda}(V^2\Delta t^2/\lambda^2 - V\Delta t/\lambda + 1) + 1 - 2V\Delta t/\lambda - 5e^{-2V\Delta t/\lambda}}{5(-1 + V\Delta t/\lambda + e^{-V\Delta t/\lambda})^2}. \end{aligned} \quad (4.19)$$

Figure 4.3 presents the MSD as formulated in Equation(4.17) and the absolute value of the NGP according to Equation(4.19) for the Lorentz gas, where the NGP is always negative. The MSD exhibits ballistic motion ($\langle \Delta \mathbf{R}^2(\Delta t) \rangle_V \propto \Delta t^2$) at a short timescale and diffusive regime ($\langle \Delta \mathbf{R}^2(\Delta t) \rangle_V \propto \Delta t$) at a long timescale. The crossover from the ballistic regime to the diffusive regime is approximately the mean free time, indicated by $V\Delta t/\lambda \approx 1$. The NGP is observed to be $-2/5$ at shorter timescales and approaches zero as the time lag Δt increases. This means that the dynamics of the mobile particle in the random dilute Lorentz gas is approximately regarded as the Gaussian process at the timescale $\Delta tV/\lambda \gtrsim 1$. Namely, the random dilute Lorentz gas model does

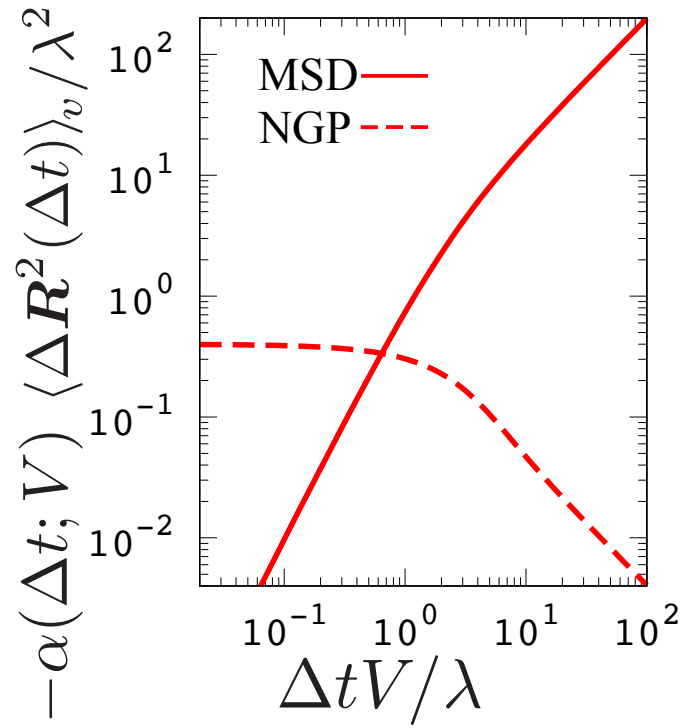


Figure 4.3: Scaled mean square displacement and non-Gaussian parameter against scaled time $V\Delta t/\lambda$ for the dilute random Lorentz gas model, predicted by Equations (4.17) and (4.18).

not show the Brownian yet non-Gaussian diffusion, which is observed in the binary gas mixture where one component is minor and lightweight. Here, the origin of non-Gaussianity at $\Delta t = 0$ is linked to the energy conservation and the smallness of the degrees of freedom in the Lorentz gas. In short timescales, the particle moves ballistically, and the NGP reflects the non-Gaussian nature in the velocity distribution. The NGP at the short-time limit can be easily calculated as:

$$\alpha(\Delta t; V) = \frac{3\langle \mathbf{V}^4 \Delta t^4 \rangle_V}{5\langle \mathbf{V}^2 \Delta t^2 \rangle_V^2} - 1 = -\frac{2}{5}, \quad (4.20)$$

This result aligns with the theoretical predictions for the short timescale behavior displayed in Figure 4.3.

4.2.3 Correlation Functions of Binary-Gas Mixture

The Lorentz gas has been conventionally regarded as a model representing a lighter particle moving in heavier particles. Then, one might anticipate that this model could replicate the Brownian yet non-Gaussian diffusion observed for the lighter particle. However, the theoretical analysis of the random dilute Lorentz gas, as depicted in Figure 4.3, indicates that the model does not demonstrate non-Gaussian behavior in the timescale of normal diffusion (where MSD is proportional to t).

The discrepancy between the behaviors observed in the Lorentz gas model and those in binary gas mixtures [2] stems from the relaxation of the speed (or kinetic energy) of a lightweight particle in the binary gas mixture over very long timescales. Namely, it is physically not reasonable to assume that the speed of a lightweight particle remains constant over a long time scale for the description of the Brownian yet non-Gaussian diffusion. To address this type of diffusion, it is necessary to consider the effect that the target particle takes at various speeds. This effect can be incorporated by the ensemble average for the time-correlation function. The statistical quantities, such as the MSD for the binary-gas mixture, would be interpreted as the MSD in the Lorentz gas averaged over the initial speed of the lightweight particle within a certain timescale. In an equilibrium state, the probability density for the speed of the lightweight particle follows the Maxwell-Boltzmann distribution at inverse temperature β , expressed as:

$$P_{\text{MB}}(V) = 4\pi V^2 \left(\frac{\beta M}{2\pi} \right)^{3/2} \exp\left(-\frac{\beta M V^2}{2} \right). \quad (4.21)$$

The ensemble average of the MSD is calculated as

$$\begin{aligned} \frac{\langle \Delta \mathbf{R}^2(\Delta t) \rangle}{\lambda^2} &= \int \frac{\langle \Delta \mathbf{R}^2(\Delta t) \rangle_V}{\lambda^2} P_{\text{MB}}(V) dV \\ &= 2 \left[-1 + \frac{2\gamma \Delta t}{\sqrt{\pi}} + (1 + 2\gamma^2 \Delta t^2) e^{\gamma^2 \Delta t^2} \text{erfc}(\gamma \Delta t) \right], \end{aligned} \quad (4.22)$$

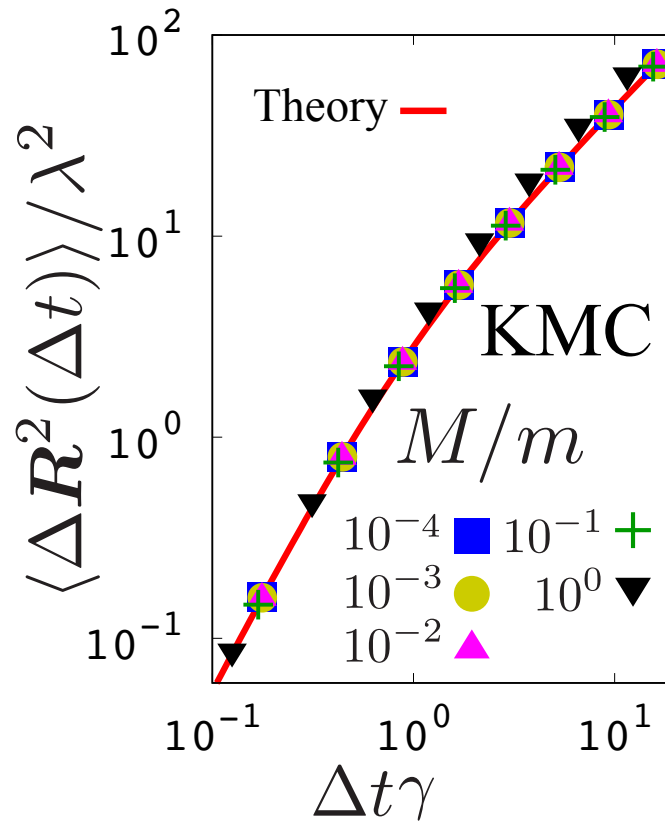


Figure 4.4: Scaled mean square displacement against scaled time $\Delta t \gamma$ in binary gas mixtures. The red curve represents the theoretical prediction (Equation (4.22)). For comparison, symbols present the result for the lightweight particle in the binary gas mixture with various mass ratios M/m , obtained from the KMC simulations as displayed in Figure 3.2.

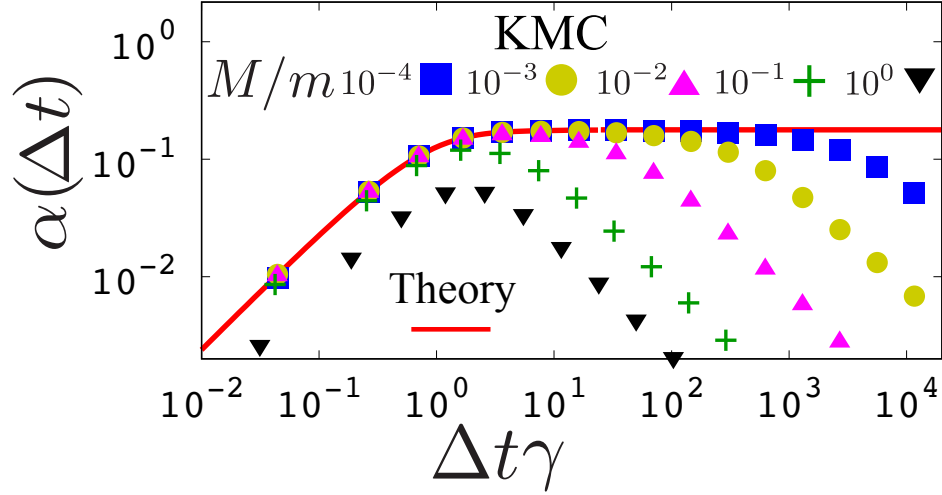


Figure 4.5: Theoretical prediction for the non-Gaussian parameter (NGP) for the minor lightweight particle in the binary gas mixtures, derived from Equations (4.22) and (4.23). The symbols represent the results with the various mass ratios obtained from the KMC simulations, as represented in Figure 3.10.

where γ is defined as $\gamma = 1/\lambda\sqrt{2\beta m}$, which can be regarded as a characteristic frequency. Figure 4.4 shows the scaled mean square displacement against scaled time. The red curve represents the theoretical result for the averaged time correlation function, Equation (4.22). For comparison, the results for the binary gas mixture are also presented with various mass ratios M/m , which have already been obtained by the KMC simulations displayed in Figure 3.2. The theoretical predictions align well quantitatively with the results from the KMC simulations, particularly when the mass ratio is considerably small ($M/m \ll 1$).

Analogously, the canonical ensemble average for the NGP for the Lorentz gas is analytically computed. The ensemble average of the fourth-order moment of the self-part of the van-Hove correlation function is calculated as follows:

$$\begin{aligned}
 \frac{\langle \Delta \mathbf{R}^4(\Delta t) \rangle}{\lambda^4} &= \int \frac{\langle \Delta \mathbf{R}^4(\Delta t) \rangle_V}{\lambda^4} P_{\text{MB}}(V) dV \\
 &= 8 - \frac{16\gamma\Delta t}{\sqrt{\pi}} + 40\gamma^2\Delta t^2 - \frac{224\gamma^3\Delta t^3}{3\sqrt{\pi}} - \frac{128\gamma^5\Delta t^5}{3\sqrt{\pi}} \\
 &\quad - \left(8 + 32\gamma^2\Delta t^2 - 96\gamma^4\Delta t^4 - \frac{128}{3}\gamma^6\Delta t^6 \right) e^{\gamma^2\Delta t^2} \text{erfc}(\gamma\Delta t).
 \end{aligned} \tag{4.23}$$

From the second and fourth moments, Equations (4.22) and (4.23), the non-Gaussian parameter is calculated. Figure 4.5 presents the NGP, $\alpha(\Delta t)$, against scaled time. The theoretical result,

described in Equation (4.22), is represented as the red curve. The numerical data for the binary gas mixture, which is obtained in Figure 3.10, is also shown with various mass ratios, using symbols. The theoretical result exhibits the plateau regime at the normal diffusion regime $\Delta t\gamma \gtrsim 1$, which indicates that the canonical ensemble average of the Lorentz gas model can capture the Brownian yet non-Gaussian diffusion. Further, the theoretical result is quantitatively consistent with the simulation result, except for the Gaussian decay at a very long timescale, which will be discussed subsequently. Distinct from the Lorentz gas case, as presented in Figure 4.3, the NGP calculated using Equations (4.22) and (4.23) approaches zero at $\Delta t \rightarrow 0$. This is a natural consequence where the velocity distribution of the minor lightweight particle obeys the Maxwell-Boltzmann distribution, i.e., Gaussian distribution. When considering the long timescale as time extends to infinity ($\Delta t\gamma \rightarrow \infty$), the NGP asymptotically approaches the constant value of $3\pi/8 - 1$. This limit is consistent with the plateau observed in the NGP obtained using the KMC simulations.

The self part of the van-Hove correlation function $G_s(\Delta\mathbf{R}, \Delta t)$ would be important, particularly at a timescale, which is considerably larger than the mean free time. When considering the Lorentz gas at such a time scale (where $s \ll V/\lambda$), the expression given in Equation (4.14) is simplified as

$$\hat{C}(\mathbf{k}; s, V) \approx \frac{\arctan(k\lambda) - \frac{ks}{k^2V + V/\lambda^2}}{(V/\lambda) \left[k\lambda - \arctan(k\lambda) + \frac{ks}{k^2V + V/\lambda^2} \right]}. \quad (4.24)$$

Its inverse-Laplace-transform is

$$C(\mathbf{k}; t, V) \approx (1 + k^2\lambda^2) \exp \left[-\frac{(1 + k^2\lambda^2)[k\lambda - \arctan(k\lambda)] \Delta t V}{k\lambda \lambda} \right]. \quad (4.25)$$

It is important to recognize that Equation (4.25) is applicable for the long time scale, specifically when $\Delta t \gg \lambda/V$. In such a timescale, the predominance of the short-wavelength component at $k\lambda \ll 1$ would be expected. For the small wavelength, Equation (4.25) is simplified to:

$$C(\mathbf{k}; \Delta t, V) \approx \exp \left(-\frac{V\Delta t\lambda k^2}{3} \right). \quad (4.26)$$

This equation is nothing but the characteristic function of the Gaussian distribution. Consequently, the van Hove correlation function for the Lorentz gas for a given speed V at the long-timescale is approximately expressed as the Gaussian distribution:

$$G(\Delta X; \Delta t, V) \approx \sqrt{\frac{3}{4\pi V\lambda\Delta t}} \exp \left(-\frac{3\Delta X^2}{4V\lambda\Delta t} \right). \quad (4.27)$$

When integrating this function with the Maxwell-Boltzmann distribution as shown in Equations (4.21) and (4.27), the van Hove correlation function for a minor lightweight gas particle in a binary gas mixture is obtained:

$$G(\Delta X; \Delta t) = \int_0^\infty G(\Delta X; \Delta t, V) P_{\text{MB}}(V) dV, \quad (4.28)$$

This result aligns with the result obtained from a phenomenological approach as shown in Equation (3.27).

4.3 Discussion

The current model predicts that the Non-Gaussian Parameter $\alpha(\Delta t)$ asymptotes to a constant at a long-time limit. Namely, the model fails to reproduce the Gaussian decay, which was observed in the binary gas mixture, which is presented in Figure 4.5. The difference between the theoretical calculation and the kinetic Monte Carlo simulation at the long timescale stems from the omission of the speed relaxation. The current theoretical model simply incorporates the effect that the target particle takes various speeds, just through the canonical ensemble average for the time-correlation function. Namely, the relaxation of the speed is not directly treated in the calculation. As a result, the diffusion coefficient of the target particle for a given speed V remains unchanged even at the long timescale for a single trajectory. This is the reason why the NGP does not approach zero at the long-time limit in the theoretical model.

In a binary gas mixture, the diffusion coefficient of a lightweight particle experiences temporal fluctuations owing to slow speed relaxation. To accurately describe the diffusion of such a particle over a long timescale, it is necessary to integrate an additional stochastic process into the model. The diffusing diffusivity model, as presented by Chechkin et al. [116], serves as a suitable framework for this purpose. In this model, the diffusion coefficient is governed by the Langevin equation, which can effectively capture the effect of the speed fluctuations. Some results from the gas kinetic theory [117] would be utilized in designing the stochastic process of the diffusion coefficient.

Another possible approach for the description of the Brownian yet non-Gaussian diffusion in gas is based on the Boltzmann equation [11, 12]. Formally, any distribution function and time correlation function of a gas particle can be calculated from the Boltzmann equation, and thus, the Brownian yet non-Gaussian diffusion should also be expressed, although the analytical calculations would be challenging. However, for some limited cases, the analyses are possible. For instance, the Boltzmann equation of a heavy particle immersed in light gas particles can be reduced to

the Fokker-Planck equation corresponding to the simple Langevin equation, which is analytically solvable [84]. In the same way, the Boltzmann equation for a light particle in heavy gas particles could possibly be simplified into a Fokker-Planck equation, which is solvable. If such a strategy can be performed, a new modeling path for the fluctuating diffusivity based on the microscopic description becomes possible. Such a theoretical analysis is interesting for future work.

4.4 Summary

This chapter theoretically examined the dynamics of a minor light particle situated in heavier gas particles, utilizing the dilute Lorentz gas model. The Mean Squared Displacement and Non-Gaussian parameter for the conventional Lorentz gas model at a given velocity V were analytically obtained. The result did not exhibit the Brownian yet non-Gaussian diffusion, which appears in binary gas mixtures with significant differences in mass and fraction. It was observed that such Brownian yet non-Gaussian diffusion can be reproduced by averaging the time correlation functions of the Lorentz gas model over initial speeds, except for the long timescale, which is larger than the relaxation time of the speed of the minor lightweight particle. This study establishes a link between the traditional Lorentz gas model and binary gas mixtures, offering novel perspectives on gas diffusion.

Chapter 5

Increase in Diffusivity of Rod in Obstacles

Abstract

The dynamics of the rod particle situated in spatially fixed point obstacles is numerically examined under the assumption of the Markovian process. It is found that the translational diffusion coefficient of the rod particle exhibits non-monotonic dependence against the number density of the obstacles when the aspect ratio of the rod is large, even in the current Markovian case. The power exponents of the translational diffusion coefficient at the dilute, intermediate density, and concentrated regimes are straightforwardly understood based on the angular velocity of the rod and collision frequency.

5.1 Introduction

The translational diffusion coefficient D of a target particle decreases when the concentration of the surrounding matrix particles increases in most cases. This reduction in D is typical behavior, which can be intuitively explained as the result of the increase in the collision frequency subject to the target particle. Interestingly, in cases where the particle is rod-shaped, an unexpected behavior is observed: D may actually increase with an increase in matrix concentration, provided the concentration reaches a certain value. This unusual behavior was initially reported by Frenkel and Maguire [34, 35] in their study of fluids composed of infinitely thin rods, where the static properties are those in an ideal gas. Subsequent studies [118, 119] provided more precise data on this

phenomenon. In the systems examined by Frenkel and Maguire, there are no concealed particles or thermostats; particles move in a ballistic manner, interrupted only by elastic collisions. Following these foundational studies [34, 35], a similar increase in D has been observed in diverse systems, including (i) an infinitely thin rod in a two-dimensional array of spatially fixed point obstacles [43], (ii) a thick rod navigating through a two-dimensional matrix filled with circular obstacles [67], and (iii) an active matter fluid where rods propel themselves along their major axis [120]. Notably, in these instances, the increase in D does not result from a phase transition. Still, it is important to note that in certain rod systems, an increase in D is observed concurrently with the isotropic-nematic transition [53]. These complex multi-particle interactions, though interesting, are not within the scope of this chapter.

Some concepts were considered to explain the increase in the diffusion coefficient D of the rod-shaped particle, including steric hindrance, dynamic correlation, confinement, and tube-like restriction [35, 43]. Although these concepts are not well-defined, they represent a cylindrical constraint that restricts the rotational motion of the rod. In this dissertation, such a concept is referred to as the “kinetic constraint,” which is defined as a constraint that prevents the rod from moving through neighboring obstacles until the rod travels a distance approximately equal to the rod length. Based on the kinetic constraint, the increase in D can be phenomenologically explained. The rod rotational motion is kinetically constrained by the matrix particles, while the ballistic motion along the major axis of the rod is not largely hindered when the rod is sufficiently thin. Consequently, the ballistic motion of the rod along the major axis persists for a long timescale, which becomes large as the concentration of media increases and the rotational constraint becomes strong. The ballistic motion is rapid compared with the diffusive motion, and the persistence of the ballistic motion leads to the increase in D . An active matter composed of a rod swimming along the major axis can also show the increase in D with a similar mechanism [120]. In light of prior works, one question arises: Is the kinetic constraint required for the realization of the increase in rod translational diffusivity?

In exploring the potential mechanism for an increase in the diffusion coefficient D , a hypothesis has been formulated. Specifically, the increase in diffusivity could result only from a hindrance of rotational motion without disturbing motion along the major axis. To validate this hypothesis, a simple model system is employed; the current system features a decrease in rotational diffusivity as the density of the matrix increases while maintaining largely unaffected ballistic motion along the major axis of a rod particle. A possible representation of this system is a single mobile rod within three-dimensional (3D) fixed point obstacles. This system can be viewed as an extension

of the Lorentz gas models [68,81,100], which usually involve a single spherical particle navigating through fixed obstacles.

In this Chapter, an increase in the diffusion coefficient D is observed even under a Markovian process, where the kinetic constraint is essentially non-existent; the obstacles in the current system do not remain in the same position nor constrain the rotational motion of the rod, while the obstacles change the rod motion. The dynamics of a single sphere-cylindrical particle situated in a three-dimensional matrix of randomly distributed point obstacles are explored using a kinetic Monte Carlo (KMC) method [97,98]. This approach assumes a Markovian process, where successive collisions between the rod and obstacles are stochastically independent like those in a dilute gas model, contrasting with typical molecular dynamics simulations. The study finds that D for this rod-like particle increases in a regime of intermediate matrix density if the rod is sufficiently long. In this model, D reaches a peak value and subsequently decreases as obstacle density is sufficiently large, which is attributed to the finite thickness of the rod. Based on the Markovian nature of the system, scaling relations between D and obstacle density are provided for respective regimes, including dilute, intermediate, and concentrated densities. These findings may offer new insights into the diffusion phenomena of non-spherical particles.

5.2 Simulation Method

5.2.1 System Setting

The current system is comprised of a rod-like sphero-cylinder, also termed a capsule or stadium of revolution, characterized by a radius σ , mass M , and a major axial length L . The effective length of the rod is $L_e = L + 2\sigma$, accounting for the half-spherical end-caps. The inertia tensor \mathbf{I} is calculated under the assumption that the rod mass is uniformly distributed throughout its volume [121]. The schematic representation of the rod is illustrated in Figure 5.1. In this model, point obstacles are uniformly distributed throughout an unbounded three-dimensional space, characterized by a number density ρ . The interaction between the rod and these obstacles is defined by a hard-core potential, ensuring that the obstacles neither penetrate the rod nor move during a collision. The rod exhibits ballistic motion except when it undergoes an elastic collision with an obstacle. During such a collision, both the translational velocity \mathbf{V} and the angular velocity $\mathbf{\Omega}$ of the rod are altered, adhering to the principle of conservation of the total energy of the system. This total energy is apportioned between the translational and rotational kinetic energy of the rod particle. The total

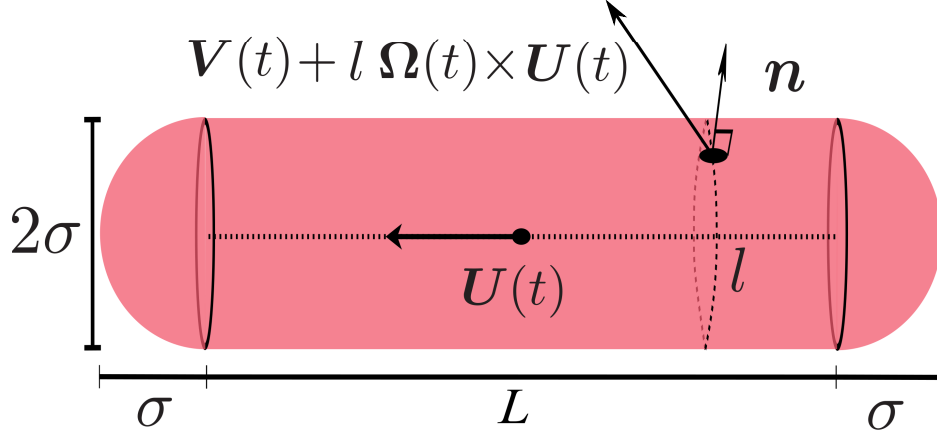


Figure 5.1: Schematic illustration of the rod. The collision frequency with the variables l and \mathbf{n} is determined from rod direction $\mathbf{U}(t)$ and velocities for the translational and rotational degrees of freedom, $\mathbf{V}(t)$ and $\boldsymbol{\Omega}(t)$.

energy of the system is fixed at $5/2\beta$, with β representing the inverse temperature. This energy value remains constant throughout the duration of the simulations. By choosing mass M , radius σ , and inverse temperature β as the basis for dimensionless units, this model is characterized only by two remaining parameters: the effective rod length L_e and the number density of the obstacles, ρ . For clarity, a speed unit \bar{V} , which satisfies $1 = \beta M \bar{V}^2$, is defined. This study presents physical quantities with their dimensions to enhance understanding. However, for those who prefer working with reduced quantities, it is possible to set variables, including M , σ , β , and \bar{V} , to unity without compromising the generality. In this system, the interaction between the rod and obstacles is defined by a hard-core potential, and then the dynamical properties remain independent of temperature, provided that the physical quantities are represented in dimensionless units. Here, in this chapter, the focus is not on the trapping regime, which emerges approximately at densities surpassing the inverse volume of the sphero-cylinder, denoted as $\rho \sigma^2 L_e \gtrsim 1$.

5.2.2 Simulation Protocol

For the current system, the kinetic Monte Carlo (KMC) simulation [97, 98] is constructed to calculate the dynamics of the rod with the Markovian process. This method requires two key inputs: (i) collision frequency density between the rod and an obstacle, and (ii) the change rule of the translational and angular velocities of the rod at the collision. The input (i) is calculated in a similar manner as the case for collisions between the spherical particles, as presented in Chapter 3.

Namely, the collision frequency density between the sphero-cylinder and a point obstacle for given variables $\mathbf{V}(t)$, $\mathbf{\Omega}(t)$, and $\mathbf{U}(t)$ is calculated under the assumption that the point obstacles are uniformly distributed in any time. Here, for a simple description, the 8-dimensional time-dependent variables $\mathbf{V}(t)$, $\mathbf{\Omega}(t)$, and $\mathbf{U}(t)$ are simply represented as $\mathbf{\Lambda}(t)$. $\mathbf{\Lambda}(t)$ defines the state of the rod, and the input (i) depends only on $\mathbf{\Lambda}(t)$. The total collision frequency for a given $\mathbf{\Lambda}(t)$, which is denoted as $\bar{\nu}(\mathbf{\Lambda}(t))$, is calculated by the integration of the following collision frequency density over the surface of the rod:

$$\begin{aligned} \nu(l, \mathbf{n}; \mathbf{\Lambda}(t)) = & \rho\sigma \mathbf{V}_e(l; \mathbf{\Lambda}(t)) \cdot \mathbf{n} \Theta[\mathbf{V}_e(l; \mathbf{\Lambda}(t)) \cdot \mathbf{n}] \\ & \times \left\{ \delta(\mathbf{U}(t) \cdot \mathbf{n}) + \sigma\delta\left(l - \frac{L}{2}\right) \Theta[\mathbf{U}(t) \cdot \mathbf{n}] + \sigma\delta\left(l + \frac{L}{2}\right) \Theta[-\mathbf{U}(t) \cdot \mathbf{n}] \right\}, \end{aligned} \quad (5.1)$$

where l refers to the axial coordinate along the rod direction, and \mathbf{n} is a unit vector perpendicular to the rod surface as illustrated in Figure 5.1. These variables determine the coordinate of the collision point between the rod and a colliding obstacle, expressed as $l\mathbf{U} + \sigma\mathbf{n}$. The velocity at this collision point is represented as $\mathbf{V}_e(l; \mathbf{\Lambda}(t)) = \mathbf{V}(t) + l\mathbf{\Omega}(t) \times \mathbf{U}(t)$. In Equation (5.1), the three terms within the curly brackets correspond to collisions occurring on different parts of the rod: the first term relates to collisions along the side (denoted as \parallel), while the second and third terms pertain to collisions at the two opposite edges (indicated as \pm) of the rod. Utilizing $\nu(l, \mathbf{n}; \mathbf{\Lambda}(t))$ and $\bar{\nu}(\mathbf{\Lambda})$, the location of the collision point and the time interval Δt_c for consecutive collisions are determined through stochastic sampling methods like inversion method or rejection method [122]. Subsequently, From the sampled variables, the rod state, characterized by \mathbf{R} , \mathbf{U} , \mathbf{V} , and $\mathbf{\Omega}$, undergoes updates in accordance with the principles of classical mechanics for the rigid body. By iteratively performing these sampling and updating processes, the dynamics of the rod particle is numerically computed. Comprehensive explanations regarding the derivation of collision statistics, the employed sampling technique, and update protocols are available in Appendix 5.A in this Chapter.

5.3 Results

5.3.1 Increase in Diffusivity

Distinct behaviors emerge when varying the parameter ρ while maintaining a constant $L_e = 2502\sigma$, as visually captured by the representative trajectories illustrated in Figure 5.3. For visibility, the three-dimensional dynamics is projected onto the XY plane, and respective axes are scaled by

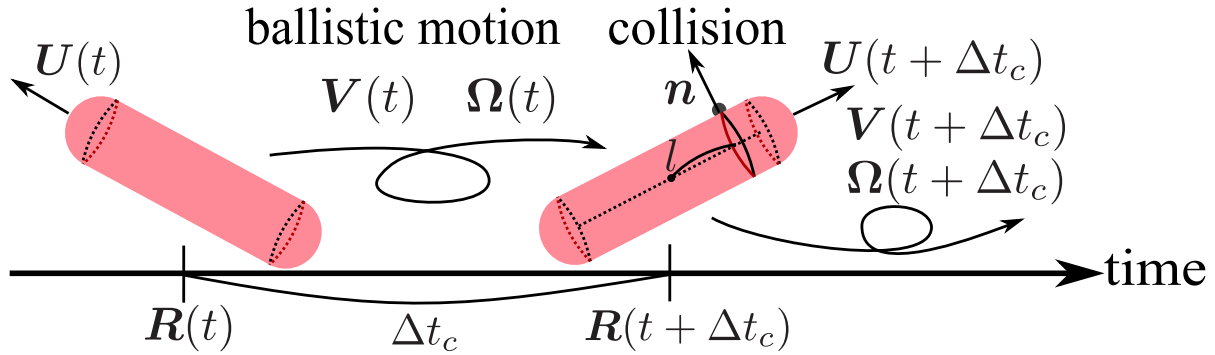


Figure 5.2: Schematic representation of the Kinetic Monte Carlo (KMC) method. $\mathbf{U}(t)$, $\mathbf{R}(t)$, $\mathbf{V}(t)$, and $\mathbf{\Omega}(t)$ denote the directional unit vector, position, velocity, and angular velocity of the rod at time t , respectively. The coordinates of the collision point are represented by l and \mathbf{n} , with l ranging from $-L/2$ to $+L/2$ as the axial coordinate and \mathbf{n} being the surface normal at the point of collision. Δt_c refers to the time interval between successive collisions. The variables Δt_c , l , and \mathbf{n} are stochastically sampled based on the collision statistics, as per Equation (5.1). Following this sampling, the values of \mathbf{R} , \mathbf{U} , \mathbf{V} , and $\mathbf{\Omega}$ at the subsequent time $t + \Delta t_c$ are calculated.

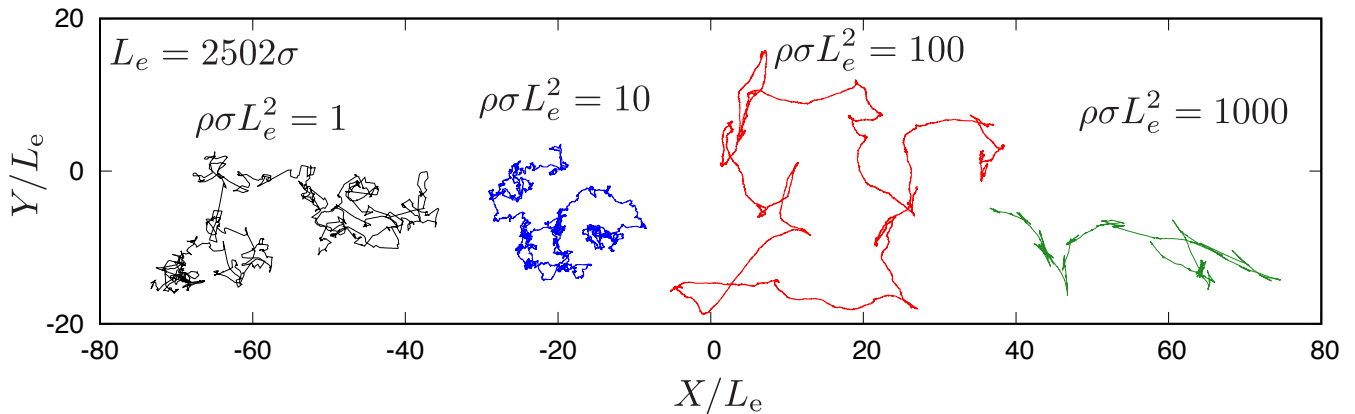


Figure 5.3: Illustration of the center of mass trajectories of a rod at the length $L_e = 2502 \sigma$ with different scaled obstacle densities, $\rho \sigma L_e^2$, obtained using the kinetic Monte Carlo simulations. The 3D motions are projected onto the XY -plane and are normalized with respect to the rod effective length, L_e .

the effective rod length. The duration of observation for these behaviors is $2.0 \times 10^6 \sigma / \bar{V}$. When $\rho\sigma L_e^2$ equals 1 or 10, the motion of the rod appears to be random. However, at a higher density, specifically when $\rho\sigma L_e^2$ is 100, there is a noticeable tendency for the rod to move in a straight manner over greater distances compared to that in lower density cases. At a higher density, where $\rho\sigma L_e^2$ reaches 1000, the motion of the rod is characterized by both straight and bouncing motions

To analyze the motions depicted in Figure 5.3, the translational diffusion coefficient D of the center of mass of the mobile rod is computed from the mean square displacement in a linear time regime using the relation, $\langle \Delta \mathbf{R}^2(\Delta t) \rangle = 6Dt$. The relation between $D/\bar{V}\sigma$ and the obstacle number density $\rho\sigma^3$ is presented in Figure 5.4(a) for various lengths of the target rod, L_e , where error bars are a result of the fitting. D demonstrates non-monotonic behavior with an increase in ρ for rods that are significantly elongated, specifically when $L_e \gtrsim 66 \sigma$. In such cases, D at large L_e displays both a local minimum and maximum. When the data are displayed in scaled dimensions as $D/\bar{V}L_e$ and $\rho\sigma L_e^2$, as indicated in Figure 5.4(b), the curves collapse except in the case of higher density regimes. The observed asymptotic behaviors in different density regimes are as follows: for small densities, $D/\bar{V}\sigma \propto (\rho\sigma^2 L_e)^{-1}$; for intermediate densities, $D/\bar{V}\sigma \propto \rho L_e^3$; and for large densities; $D/\bar{V}\sigma \propto (\rho\sigma^3)^{-1}$. It is important to note that this non-monotonic dependence of D on ρ occurs even in a Markovian process. In contrast to D , the rotational diffusion coefficient D_{rot} in the current system displays a monotonic relation with ρ , specifically, $D_{\text{rot}}\sigma/\bar{V} \sim (\rho L_e^3)^{-1}$ as detailed in Figure 5.7 in Appendix 5.C.

The scaling relations between the diffusion coefficient D and the number density ρ can be simply elucidated based on the Markovian nature of the current system. In an equilibrium state, D is calculated not from the mean square displacement, but through the integration of the velocity auto-correlation function over a time lag, represented by $D = \int_0^\infty \langle \mathbf{V}(\Delta t) \cdot \mathbf{V}(0) \rangle d\Delta t$. Consequently, the diffusion coefficient can be approximated as the product of the squared speed \bar{V}^2 and the relaxation time of the translational velocity. The collision frequency in this system is contributed by two distinct parts: the collision frequencies from the side, denoted as \bar{v}_\parallel , and those from the edges, denoted as \bar{v}_\pm . The scaling of these contributions is quantified as $\bar{v}_\parallel \sim \rho\sigma L_e \bar{V}$ and $\bar{v}_\pm \sim \rho\sigma^2 \bar{V}$. These scaling relations are further substantiated by detailed calculations regarding collision frequencies, as outlined in Equations (5.8) and (5.13) in Appendix 5.A. Additionally, the average angular velocity of the rod scales as $\bar{\Omega} \sim \bar{V}/L_e$. In the dilute regime, where $\rho\sigma L_e^2 \lesssim 1$, the condition $\bar{\Omega} > \bar{v}_\parallel$ is typically met. Under this low-density condition, the rod predominantly rotates and infrequently collides with obstacles along its side. A few collisions significantly alter the rod motion as the rod undergoes impulsive forces from a variety of directions. Consequently,

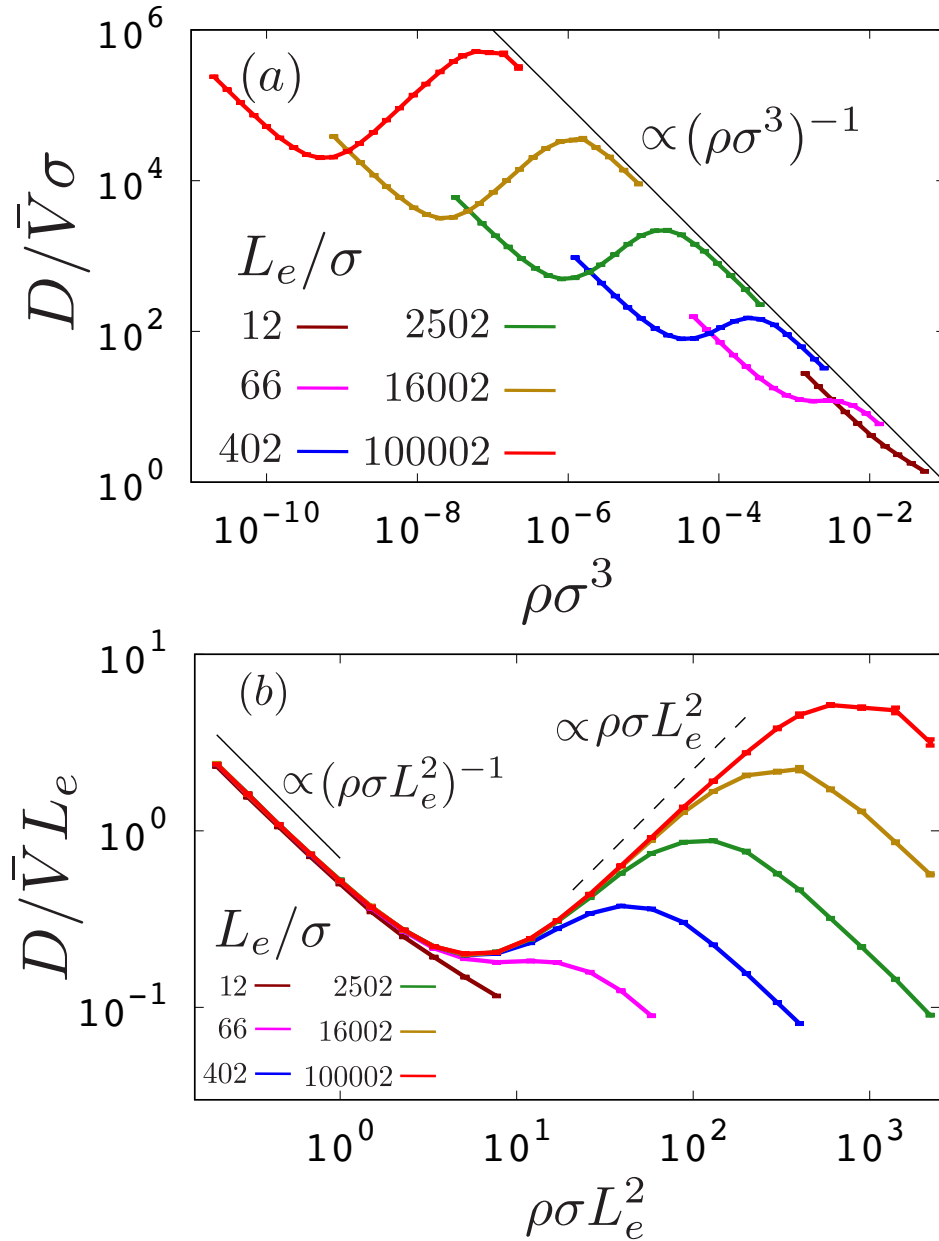


Figure 5.4: Translational diffusion coefficient D of the rod for varying lengths L_e , calculated from Kinetic Monte Carlo simulations. The data are presented in two forms: (a) $D/\bar{V}\sigma$ as a function of the obstacle number density $\rho\sigma^3$, and (b) in a scaled manner as $D/\bar{V}L_e$ versus $\rho\sigma L_e^2$. Error bars and the respective asymptotic exponents are also included.

the translational velocity relaxation time can be estimated as roughly equal to the average collision time $\sim 1/\bar{v}_{\parallel}$, and D scales as $D \sim \bar{V}^2/\bar{v}_{\parallel} \sim \bar{V}/\rho\sigma L_e$. This explanation aligns with the random motions observed in the lower density regions, specifically where $\rho\sigma L_e^2 \lesssim 10$, as illustrated in Figure 5.3.

In the higher density regime, $\rho\sigma L_e^2 \gtrsim 1$, the condition $\bar{\Omega} < \bar{v}_{\parallel}$ is met. In this case, the rod rotational motion becomes diffusive, resulting in a slow directional change. In this regime, velocities in orthogonal directions relax swiftly, while those in axial directions remain relatively unaffected. In such a circumstance, two potential relaxation mechanisms exist for the axial direction velocity: alteration in the rod direction or collisions at its edges. The change in the rod direction between collisions is approximated as $\Delta\theta \sim \bar{\Omega}/\bar{v}_{\parallel}$. Consequently, the rotational relaxation time is scaled as $\tau_r \sim \Delta\theta^{-2}/\bar{v}_{\parallel} \sim \rho L_e^3 \sigma / \bar{V}$. This calculation also leads to the prediction of the rotational diffusion coefficient, $D_{\text{rot}} = (2\tau_{\text{rot}})^{-1} \sim \bar{V}/\rho L_e^3 \sigma$, which agrees with the simulation data, as shown in Figure 5.7 in Appendix 5.C. The time interval between collisions at the rod edge is approximately \bar{v}_{\pm}^{-1} . In the intermediate density regime, characterized by an increase in D , the rotational relaxation time is shorter than the collision time interval at the edge. Therefore, the velocity relaxes through the rotation of direction, leading to an explanation of diffusion coefficient $D \sim \bar{V}^2 \tau_{\text{rot}} \sim \rho L_e^3 \bar{V} \sigma$. In the higher density regime, where D begins to decrease, collisions at the edge become the primary mechanism for axial velocity relaxation. Under this circumstance, the diffusion coefficient is roughly derived as $D \sim \bar{V}^2/\bar{v}_{\pm} \sim \bar{V}/\rho\sigma^2$. These described mechanisms appear to align with the observed phenomena of persistent straight motion at $\rho\sigma L_e^2 = 100$ and both straight and bouncing motions at $\rho\sigma L_e^2 = 1000$, as depicted in Figure 5.3. Furthermore, the estimated exponents are consistent with the simulation results presented in Figure 5.4.

5.3.2 Comparison with Molecular Dynamics Simulation

One may suspect that the increase in D might appear as an artifact, given the assumption of a Markovian process even for situations with large concentration regimes. Nonetheless, the following analysis demonstrates that this assumption is, fortunately, a good approximation for calculating D in the context of a rod within a 3-dimensional matrix of point obstacles. To this end, the dynamics of a rod are computed using standard molecular dynamics (MD) simulations [51]. In these simulations, the repulsive interactions between the rod and point obstacles are set to be the Weeks-Chandler-Andersen potential [123], a softer alternative to a hard-core potential. The methodology of the molecular dynamics simulations is expressed in Appendix 5.D. Figure 5.5

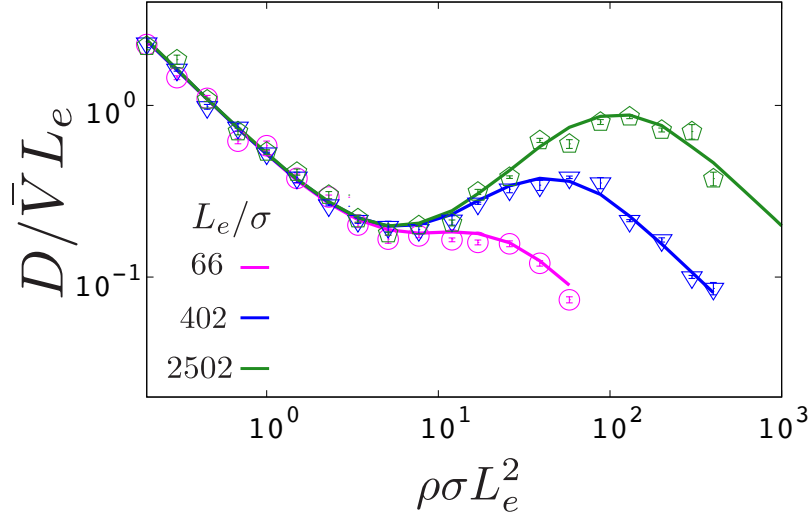


Figure 5.5: Reduced translational diffusion coefficient, denoted as $D/\bar{V}L_e$, in relation to the obstacle number density $\rho\sigma L_e^2$, obtained from the molecular dynamics (MD) simulations. Error bars, denoted by symbols, are also displayed. Data is presented for three distinct lengths of rods L_e . For comparison, results from Kinetic Monte Carlo (KMC) simulations, as previously shown in Figure 5.4, are represented using curves.

shows $D/\bar{V}L_e$ against $\rho\sigma L_e^2$ for varied rod lengths L_e/σ , calculated through MD simulations. These results include error bars derived from fittings of the mean square displacements. Due to high computational costs, long rod cases, $L_e \gtrsim 16000 \sigma$, are not analyzed. For comparisons, Figure 5.5 also presents data from the kinetic Monte Carlo (KMC) simulations (Figure 5.4) as solid curves. The diffusion coefficients obtained from MD simulations quantitatively agree with the KMC results, indicating that multi-body correlations can be negligible for the calculation of D over the broad range of ρ assessed.

5.4 Discussion

This study demonstrates that the translational diffusion coefficient, D , can indeed increase even under the Markovian process, and the exponents observed in the current system are easily explained. However, this finding does not necessarily simplify the understanding of exponents in previously studied systems. Notably, the study conducted by Frenkel and Maguire [34, 35] on the diffusion coefficient D of constituent particles in a system of infinitely thin hard rods showed that D is proportional to the square root of the rod density. In a two-dimensional setting involving a rod

among point obstacles, Höfling, Frey, and Franosch [43] found the power exponent of D relative to obstacle density to be 0.8 in a concentrated regime. Additionally, Mandal et al. [120] explored the dynamics of a rod-shaped active swimmer moving axially and found that D is proportional to the square of the density of its constituent particles. In these earlier systems, kinetic constraints would play a significant role for each power exponent and must be considered to explain the exponents comprehensively.

Tucker and Hernandez [67, 124] examined a system that is similar to the current system. They considered the dynamics of a mobile rod with the length 5\AA moving through spatially fixed spherical obstacles with a radius of 0.5\AA . They considered various rod thicknesses, specifically 0, 0.1, and 0.5\AA . They argued that an increase in the diffusion coefficient D does not occur in their 3D system, although it occurs in a 2D setup. This argument may appear to be inconsistent with the obtained results. Nonetheless, equating the dimensional parameters in their system with those in the current study, the rod effective aspect ratio becomes approximately 10, which is obtained from considering the effective interaction distance: the sum of the rod thickness and the obstacle size. For a rod with an aspect ratio of 10, no increase in the diffusion coefficient D is observed, as demonstrated in Appendix 5.8. The rise in D becomes apparent when the aspect ratio exceeds approximately 24, corresponding to $L_e/\sigma \gtrsim 520/11$ in the current system. Namely, in the system analyzed by Tucker and Hernandez [67], an increase in D would transpire with either a significantly smaller obstacle radius or a substantially longer rod. Otto, Aspelmeier, and Zippelius [125] approached the dynamics of infinitely thin rods in a Markovian process, assuming uncorrelated sequential collisions. They concluded that an increase in D is unlikely in such a Markovian nature. This stance starkly contrasts with the findings of this study. However, their theory did not incorporate the slow relaxation of the ballistic motion along the axial direction, and thus, the increase in D could not be captured in their theory.

The current numerical simulations demonstrated that the increase in the diffusion coefficient can appear in the Markovian nature. This means that, if the stochastic process for the velocity \mathbf{V} , angular velocity $\mathbf{\Omega}$, and direction vector \mathbf{U} of the rod is considered, the Markovian process is enough to express the increase in D . Meanwhile, if only the translational velocity is observed, its stochastic process will seem to be the non-Markovian process; the coarse-graining of the variables, $\mathbf{\Omega}$ and \mathbf{U} in this case, generally induces the non-Markovianity. The rotational degrees of freedom exhibit a long-time relaxation, as estimated in Section 5.3.1. If such a long-time relaxation can be incorporated as a historical effect into the stochastic process of the translational degrees of freedom of the rod, the increase in D would be analytically expressed.

It is emphasized to note that the increases in D can manifest in a ballistic system [34, 35, 43, 118, 119] or in certain active matter systems [120], in which the persistence of the axial motion emerges. While it might be speculated that a rise in D is possible for passive rod-shaped particles in some solvents or porous media, these systems do not demonstrate an increase in diffusivity via the same mechanism as the current study due to the rapid relaxation of the ballistic motion in the axial direction by Brownian motion. A recent study observed an increase in diffusivity with the growing aspect ratio of a rod within a gel [126], though the underlying mechanism differs from that of this study.

The current system involves a rod interacting with fixed or infinitely massive point obstacles. Considering the finite mass cases in an equilibrium state may be interesting. When the mass of the obstacles substantially surpasses M , the obstacle motion is slow due to the Maxwell-Boltzmann velocity distribution. This situation aligns closely with the current system, as the mobile obstacles can effectively be regarded as fixed obstacles in relation to the rod particle, and the increase in diffusivity of the rod is expected to occur. Conversely, if the obstacle mass is on par with M , a deviation from the current system can occur, influenced by the substantial variation in translational and rotational relaxation times against obstacle mass. Nonetheless, an increase in diffusivity might still be evident since the increase in D simply results from the reduction of the rotational motion and persistence of the ballistic motion along the axial direction, which can hold for finite mass cases. Investigating the impact of obstacle mass on the increase in diffusivity will be an interesting future work.

5.5 Summary

This chapter revealed that an upturn in D is possible even in a Markovian nature, which does not essentially induce the kinetic constraint. A simplified model was employed, consisting of a single mobile rod-shaped particle in fixed obstacles in a three-dimensional space. The dynamics of the rod was analyzed through efficient kinetic Monte Carlo simulations assuming the Markovian process. The translational diffusion coefficient D of the rod exhibits a decrease, then an increase, and finally a decrease again with the increase in obstacle density. This unusual diffusion behavior is interpretable thanks to the Markovian process assumption. Specifically, the D upturn is elucidated without invoking kinetic constraints but rather by focusing on two timescales: angular velocity and collision frequency. Additionally, the minimal length L_e required for the emergence of D upturn in the current system is approximately estimated as $L_e/\sigma \simeq 520/11$ (corresponding to an aspect ratio

of 24). This investigation will provide fresh insight into the kinetics of the non-spherical particles.

5.A Kinetic Monte Carlo Method

5.A.1 Overview of KMC Simulation

The dynamics of a target rod particle situated in fixed point obstacles are analyzed using an extended version of the kinetic Monte Carlo (KMC) method. For the implementation of the KMC simulation for the current system, four assumptions are imposed:

1. The point obstacles are uniformly situated and fixed throughout the three-dimensional space.
2. The motion of the rod particle is described by the stochastic process, and the Markovian process is induced; the collision is stochastically sampled only based on the current state of the rod, $\Lambda(t)$.
3. The interparticle interaction between the rod and the fixed obstacles is the hard-core potential. This means that any overlaps between the rod and point obstacles do not occur.
4. The collision frequency of the rod against an obstacle is assumed to be constant over a small time interval, denoted as Δt_{\max} .

Based on the settings, the collision frequency of a rod for a given rod direction \mathbf{U} , translational velocity \mathbf{V} , and angular velocity $\mathbf{\Omega}$ is calculated. This frequency is used to sample the time interval between successive collisions and the location of a collision on the rod surface. After the sampling, the rod position, direction, and velocities of the translational and rotational degrees of freedom are updated. From the time-dependent direction of the rod $\mathbf{U}(t)$, the collision frequency varies between successive collisions. Consequently, the collision time interval distribution deviates from a simple exponential function, making direct sampling of the time interval difficult. In order to circumvent this challenge, the fourth assumption is introduced in the methodology. The current strategy involves the introduction of a new parameter, denoted as Δt_{\max} . It is confirmed that the outcomes derived from Kinetic Monte Carlo (KMC) simulations remain largely unaffected by the magnitude of Δt_{\max} , provided it remains substantially smaller than the average rotation period of the rod, as demonstrated in Figure 5.6. In the KMC simulations conducted for this study, the value of Δt_{\max} chosen is significantly less than the average rotation period of the rod. More precisely, Δt_{\max} is chosen as $\sqrt{\beta I}/100$. Here, I stands for the relevant component of the moment of inertia tensor, and $1/2\beta$ is the averaged kinetic energy for each degree of freedom.

5.A.2 Collision Statistics

This section explains the derivation of collision frequency density between the rod and point obstacles, which is required for an input of the kinetic Monte Carlo scheme. The rod is characterized by its length L , radius σ , mass M , and inertia tensor \mathbf{I} , and it possesses a total kinetic energy of $5/2\beta$. The amount of point obstacles is described by a number density denoted as ρ . For clarity in physical interpretation, these physical quantities are presented with dimensions, as presented in the main texts. The rod state is described by the translational velocity $\mathbf{V}(t)$, angular velocity $\boldsymbol{\Omega}(t)$, and the direction of its symmetry axis represented by $\mathbf{U}(t)$. The following relation between $\mathbf{U}(t)$ and $\boldsymbol{\Omega}(t)$ is maintained any time,

$$\mathbf{U}(t) \cdot \boldsymbol{\Omega}(t) = 0. \quad (5.2)$$

This equation holds because the relation $\dot{\mathbf{U}} = \boldsymbol{\Omega}(t) \times \mathbf{U}(t)$, and the magnitude of \mathbf{U} remains constant over time, $0 = \mathbf{U} \cdot \dot{\mathbf{U}}$, where the dot symbolizes a time derivative. In the subsequent discussion, $\boldsymbol{\Lambda}(t)$ is used to represent the time-dependent 8-dimensional phase space variable $(\mathbf{V}(t), \boldsymbol{\Omega}(t), \mathbf{U}(t))$, which describes the rod state. Further, the effective velocity at the rod surface is introduced, defined as $\mathbf{V}_e(l; \boldsymbol{\Lambda}(t)) = \mathbf{V}(t) + l\boldsymbol{\Omega}(t) \times \mathbf{U}(t)$. Here, l denotes the axial coordinate along $\mathbf{U}(t)$, with its range specified as $l \in [-L/2, L/2]$.

On the surface of the rod, collisions with point obstacles can occur at three distinct locations: the cylindrical surface (side) or at one of the two half-spherical caps (edges). The collision point on the surface is defined by two parameters: the axial coordinate l and the direction of the surface normal at the collision point \mathbf{n} , which is a unit vector as depicted in Figure 5.1. When the collision occurs on the side of the rod, the normal vector \mathbf{n} is oriented perpendicular to the vector $\mathbf{U}(t)$. In the case of a collision at the edges, the value of l will be either $+L/2$ or $-L/2$. The collision frequency density at a given point characterized by l and \mathbf{n} for a specific state $\boldsymbol{\Lambda}(t)$, denoted as $\nu(l, \mathbf{n}; \boldsymbol{\Lambda}(t))$, is formulated as a sum of three terms: the side part and the two edge parts on the rod surface as follows.

$$\nu(l, \mathbf{n}; \boldsymbol{\Lambda}(t)) = \sum_{\mu \in \{\parallel, -, +\}} \nu_\mu(l, \mathbf{n}; \boldsymbol{\Lambda}(t)). \quad (5.3)$$

A collision on the side of the rod $\bar{\nu}_\parallel(l, \mathbf{n}; \boldsymbol{\Lambda}(t))$ is expressed as

$$\nu_\parallel(l, \mathbf{n}; \boldsymbol{\Lambda}(t)) = \rho\sigma \mathbf{V}_e(l; \boldsymbol{\Lambda}(t)) \cdot \mathbf{n} \Theta[\mathbf{V}_e(l; \boldsymbol{\Lambda}(t)) \cdot \mathbf{n}] \delta(\mathbf{U}(t) \cdot \mathbf{n}), \quad (5.4)$$

For collisions at the ends of the rod, represented by $\nu_\pm(l, \mathbf{n}; \boldsymbol{\Lambda}(t))$, the expression is:

$$\nu_\pm(l, \mathbf{n}; \boldsymbol{\Lambda}(t)) = \rho\sigma^2 \mathbf{V}_e(l; \boldsymbol{\Lambda}(t)) \cdot \mathbf{n} \Theta[\mathbf{V}_e(l; \boldsymbol{\Lambda}(t)) \cdot \mathbf{n}] \Theta[\pm \mathbf{U}(t) \cdot \mathbf{n}] \delta\left(l \mp \frac{L}{2}\right). \quad (5.5)$$

Here, the Heaviside step function is represented by Θ , while the Dirac delta function is denoted as δ . To calculate the collision frequency, it is necessary to integrate the collision frequency density $\nu(l, \mathbf{n}; \mathbf{\Lambda}(t))$ over the surface of the rod particle. This requires performing the integration across both the axial coordinate l and the surface normal \mathbf{n} . For efficient calculations, it is advantageous to adopt two distinct frames of reference that are suitably selected for the two types of collision contributions, described in Equations (5.4) and (5.5).

■ **Integration of ν_{\parallel} .** To carry out the integration of Equation (5.4), the reference frame is adjusted so that the rod direction vector and the effective velocity are represented as $\mathbf{U}(t) = (0, 0, 1)$ and $\mathbf{V}_e(t) = (V_r, 0, V_z)$, respectively, where $V_r > 0$. Consequently, the direction vector at the collision point is given by $\mathbf{n} = (\sin \theta \cos \phi, \sin \theta \sin \phi, \cos \theta)$, with $\theta \in [0, \pi]$ and $\phi \in [-\pi, \pi)$. Utilizing this coordinate system, the integration of Equation (5.4) over θ is performed, leading to:

$$\nu_{\parallel}(l, \phi; \mathbf{\Lambda}(t)) = \int_0^{\pi} d\theta \nu_{\parallel}(l, \theta, \phi; \mathbf{\Lambda}(t)) = \rho\sigma V_r(l; \mathbf{\Lambda}(t)) \cos(\phi) \Theta[\cos \phi], \quad (5.6)$$

The integration over the angle ϕ on the surface normal leads to the collision frequency density on the side at l

$$\nu_{\parallel}(l; \mathbf{\Lambda}(t)) = \int_{-\pi}^{\pi} d\phi \nu_{\parallel}(l, \phi; \mathbf{\Lambda}(t)) = 2\rho\sigma V_r(l; \mathbf{\Lambda}(t)). \quad (5.7)$$

Based on Equation (5.7), the calculation of the total collision frequency at the side, denoted as $\bar{\nu}_{\parallel}(\mathbf{\Lambda}(t))$, is expressed as follows:

$$\begin{aligned} \bar{\nu}_{\parallel}(\mathbf{\Lambda}(t)) &= \int_{-\frac{L}{2}}^{\frac{L}{2}} dl \nu_{\parallel}(l; \mathbf{\Lambda}(t)) \\ &= \frac{\rho\sigma L^2 \Omega(t)}{4} \left[(a+1)c_+ - (a-1)c_- - b \ln \left(\frac{a-1+c_-}{a+1+c_+} \right) \right], \end{aligned} \quad (5.8)$$

where various terms are defined for simplicity: $\Omega(t) = |\mathbf{\Omega}(t)|$ represents the magnitude of the angular velocity, $V(t) = |\mathbf{V}(t)|$ denotes the velocity magnitude, $c_{\pm} = \sqrt{(a \pm 1)^2 + b}$, and

$$a = \frac{2\mathbf{V}(t) \cdot (\mathbf{\Omega}(t) \times \mathbf{U}(t))}{\Omega^2(t)L}, \quad (5.9)$$

$$b = \frac{4(\mathbf{V}(t) \cdot \mathbf{\Omega}(t))^2}{\Omega^4(t)L^2}, \quad (5.10)$$

When the velocity vector \mathbf{V} is parallel to the vector \mathbf{U} , the parameters simplify to $a = b = 0$, leading to the equation $\bar{\nu}_{\parallel}(\mathbf{\Lambda}(t)) = \rho\sigma L^2 \Omega/2$. Notably, for $\Omega = 0$, the frequency becomes zero, which aligns with expectations.

■ **Integration of ν_{\pm} .** In the integration of Equation (5.5), a different frame of reference is utilized. In the new frame, the direction of $\mathbf{V}_e(l; \mathbf{\Lambda}(t)) = (0, 0, V_e(l; \mathbf{\Lambda}(t)))$ is designated as the new z -axis, while $\mathbf{U}(t) = (U_r, 0, U_z)$, with $U_r > 0$, establishes the new x -axis. Accordingly, the surface normal vector is defined as $\mathbf{n} = (\sin \theta \cos \phi, \sin \theta \sin \phi, \cos \theta)$, where θ and ϕ are within the range of $\theta \in [0, \pi]$ and $\phi \in [-\pi, \pi)$, respectively. Within this coordinate system, the collision frequency density at the angle vector \mathbf{n} is expressed as follows:

$$\begin{aligned} \nu_{\pm}(\mathbf{n}; \mathbf{\Lambda}(t)) &= \int_{-\frac{L}{2}}^{\frac{L}{2}} dl \nu_{\pm}(l, \mathbf{n}; \mathbf{\Lambda}(t)) \\ &= \rho \sigma^2 \mathbf{V}_e \left(\pm \frac{L}{2}; \mathbf{\Lambda}(t) \right) \cdot \mathbf{n} \Theta[\pm \mathbf{U}(t) \cdot \mathbf{n}] \Theta \left[\mathbf{V}_e \left(\pm \frac{L}{2}; \mathbf{\Lambda}(t) \right) \cdot \mathbf{n} \right]. \end{aligned} \quad (5.11)$$

When integrating Equation (5.11) over ϕ , the collision frequency density at θ is determined as follows:

$$\begin{aligned} \nu_{\pm}(\theta; \mathbf{\Lambda}(t)) &= \int_{-\pi}^{\pi} d\phi \nu_{\pm}(\mathbf{n}; \mathbf{\Lambda}(t)) \\ &= 2\rho \sigma^2 V_e \left(\pm \frac{L}{2}; \mathbf{\Lambda}(t) \right) \cos(\theta) \Theta[\cos \theta] \\ &\quad \times \left\{ \pi \Theta[\pm \gamma(\theta) - 1] + \cos^{-1}(\mp \gamma(\theta)) \Theta[1 - |\gamma(\theta)|] \right\}, \end{aligned} \quad (5.12)$$

where $\gamma(\theta)$ is defined as $\gamma(\theta) = U_z \cos \theta / U_r \sin \theta$. To obtain the collision frequencies at the two edges, the remaining integration over θ is performed, leading to:

$$\begin{aligned} \bar{\nu}_{\pm}(\mathbf{\Lambda}(t)) &= \int_0^{\pi} \sin \theta d\theta \nu_{\pm}(\theta; \mathbf{\Lambda}(t)) \\ &= \frac{\pi \rho \sigma^2}{2} \left\{ \left| \mathbf{V}_e \left(\pm \frac{L}{2}; \mathbf{\Lambda}(t) \right) \right| \pm \mathbf{V}_e \left(\pm \frac{L}{2}; \mathbf{\Lambda}(t) \right) \cdot \mathbf{U}(t) \right\}. \end{aligned} \quad (5.13)$$

■ **Combining Integrated ν_{\parallel} and ν_{\pm} .** By Combining Equations (5.8) and (5.13), the total collision frequency, denoted as $\bar{\nu}(\mathbf{\Lambda}(t))$, for a specific set of parameters $\mathbf{V}(t)$, $\mathbf{\Omega}(t)$, and $\mathbf{U}(t)$ is obtained. This is succinctly expressed as:

$$\bar{\nu}(\mathbf{\Lambda}(t)) = \bar{\nu}_{\parallel}(\mathbf{\Lambda}(t)) + \bar{\nu}_{+}(\mathbf{\Lambda}(t)) + \bar{\nu}_{-}(\mathbf{\Lambda}(t)). \quad (5.14)$$

5.A.3 Protocol of KMC Simulation

The rod moves ballistically until it collides against a fixed obstacle. The collision is characterized by the collision time interval Δt_c and the location at the collision point denoted as l and \mathbf{n} . To sample

these variables, the probability density of these variables is required. Here, the collision frequency is not constant because the rod direction $\mathbf{U}(t)$ is time-dependent between the successive collisions, and thus, the probability density is not straightforwardly obtained. To avoid this difficulty, the collision frequency density is assumed to be constant within the Δt_{\max} (the fourth assumption). Here, this assumption does not largely affect the result as far as Δt_{\max} is sufficiently smaller than the mean rotational period, as demonstrated in Figure 5.6. Based on this assumption, the probability density of the collision time interval for a given $\mathbf{\Lambda}(t)$ at the side and edges is simply expressed via the exponential function using Equation 5.14:

$$P(\Delta t_c; \mathbf{\Lambda}(t)) = \bar{\nu}(\mathbf{\Lambda}(t)) \exp[-\bar{\nu}(\mathbf{\Lambda}(t))\Delta t_c]. \quad (5.15)$$

Here, Equation (5.15) is valid within the range of $0 < \Delta t_c < \Delta t_{\max}$.

Step 1: Sample Collision Time Interval Δt_c . Referring to Equation (5.15), the value of Δt_c is sampled using the inversion method. Here, Δt_c should satisfies the criterion $\Delta t_c \in (0, \infty]$.

Step 2: Update of Position and Direction Vector for $\Delta t_c > \Delta t_{\max}$ When the sampled value Δt_c exceeds Δt_{\max} , it indicates that a collision has not occurred within the interval Δt_{\max} . In such a case, the time t , the position $\mathbf{R}(t)$, and the direction vector $\mathbf{U}(t)$ are updated to $t + \Delta t_{\max}$, $\mathbf{R}(t + \Delta t_{\max}) = \mathbf{R}(t) + \mathbf{V}(t)\Delta t_{\max}$, and $\mathbf{U}(t + \Delta t_{\max}) = (0, -\sin(\Omega\Delta t_{\max}), \cos(\Omega\Delta t_{\max}))$, respectively. This update is in accordance with a frame of reference where $\mathbf{U}(t) = (0, 0, 1)$ and $\mathbf{\Omega}(t) = (\Omega, 0, 0)$, which define the z - and x -axes. Moreover, the velocity \mathbf{V} and the angular velocity $\mathbf{\Omega}$ remain constant during this process, as represented by $\mathbf{V}(t + \Delta t_{\max}) = \mathbf{V}(t)$ and $\mathbf{\Omega}(t + \Delta t_{\max}) = \mathbf{\Omega}(t)$. Following the update of the variables, the process returns to Step 1.

Step 3: Update of Position and Direction Vector for $\Delta t_c < \Delta t_{\max}$ In the event that Δt_c is less than Δt_{\max} , the time parameter t , the position $\mathbf{R}(t)$, and the direction vector $\mathbf{U}(t)$ are updated in a similar manner. These updates are to $t + \Delta t_c$, $\mathbf{R}(t + \Delta t_c) = \mathbf{R}(t) + \mathbf{V}(t)\Delta t_c$, and $\mathbf{U}(t + \Delta t_c) = (0, -\sin(\Omega\Delta t_c), \cos(\Omega\Delta t_c))$, respectively.

Step 4: Sample Side or Edge Utilizing the updated phase space coordinate $\mathbf{\Lambda}(t + \Delta t_c)$, the determination of whether a collision occurs at the side or the edges of the rod is made. This is based on the collision frequencies described in Equations (5.8) and (5.13). The probability that a collision occurs at the side is calculated as $\bar{\nu}_{\parallel}(\mathbf{\Lambda}(t + \Delta t_c))/\bar{\nu}(\mathbf{\Lambda}(t + \Delta t_c))$. Similarly, the probability of a collision occurring at the edges is given by $\bar{\nu}_{\pm}(\mathbf{\Lambda}(t + \Delta t_c))/\bar{\nu}(\mathbf{\Lambda}(t + \Delta t_c))$.

Step 5: Sample Location for Collision at Side When a collision occurs at the side of the rod, the value of l is sampled using the probability density $P(l; \mathbf{\Lambda}(t + \Delta t_c))$, derived from Equations (5.7) and (5.8), expressed as follows:

$$P(l; \mathbf{\Lambda}(t + \Delta t_c)) = \frac{\nu_{\parallel}(l; \mathbf{\Lambda}(t + \Delta t_c))}{\bar{\nu}_{\parallel}(\mathbf{\Lambda}(t + \Delta t_c))} = \frac{v_r}{\mathcal{N}} = \frac{|[\mathbf{1} - \mathbf{U}(t + \Delta t_c)\mathbf{U}(t + \Delta t_c)] \mathbf{V}_e(l; \mathbf{\Lambda}(t + \Delta t_c))|}{\mathcal{N}}, \quad (5.16)$$

where $\mathbf{1}$ represents the unit tensor, and \mathcal{N} is the normalization factor. Using this probability density, l is sampled within the range $l \in [-L/2, L/2]$ using the rejection method. The probability density for ϕ is derived from Equations (5.7) and (5.6), and is given as:

$$P(\phi; \mathbf{\Lambda}(t + \Delta t_c)) = \frac{\nu_{\parallel}(l, \phi; \mathbf{\Lambda}(t + \Delta t_c))}{\nu_{\parallel}(l; \mathbf{\Lambda}(t + \Delta t_c))} = \frac{\cos(\phi) \Theta[\cos \phi]}{2}. \quad (5.17)$$

ϕ is sampled using the inversion method, expressed as $\phi = \sin^{-1}(1 - 2\chi)$, where χ is a random number uniformly distributed in the range $\chi \in [0, 1]$. For a collision occurring at the side, the angle θ is simply $\pi/2$. Consequently, the collision point l and the normal vector \mathbf{n} at time $t + \Delta t_c$ for a given $\mathbf{\Lambda}(t + \Delta t_c)$ are determined.

Step 5: Sample Location for Collision at Edge In the event of a collision occurring at one of the edges at $l = \pm L/2$, the probability density for the normal vector \mathbf{n} is formulated using Equations (5.11) and (5.13). This is represented as:

$$P(\mathbf{n}; \mathbf{\Lambda}(t + \Delta t_c)) = \frac{\nu_{\pm}(\mathbf{n}; \mathbf{\Lambda}(t + \Delta t_c)) \sin \theta}{\bar{\nu}_{\pm}(\mathbf{\Lambda}(t + \Delta t_c))} = \frac{\cos(\theta) \sin(\theta) \Theta[\cos \theta] \Theta[\pm \mathbf{U}(t + \Delta t_c) \cdot \mathbf{n}]}{\mathcal{N}}, \quad (5.18)$$

Here, \mathcal{N} denotes a normalization factor, and the term $\sin(\theta)$ is included to account for the solid angle. Based on Equation (5.18), the angles θ and ϕ are sampled simultaneously using the rejection method. As a result, the collision point, characterized by l and \mathbf{n} at time $t + \Delta t_c$ for the given $\mathbf{\Lambda}(t + \Delta t_c)$, is determined.

Step 6: Update Velocity $\mathbf{V}(t)$ and Angular Velocity $\mathbf{\Omega}(t)$. After a collision, the velocity $\mathbf{V}(t + \Delta t_c)$ and angular velocity $\mathbf{\Omega}(t + \Delta t_c)$ are updated based on the sampled values of l and \mathbf{n} . For this computation, a frame of reference is utilized in which $\mathbf{U}(t + \Delta t_c) = (0, 0, 1)$ defines the z -axis. Within this frame, two components of the inertia tensor, I_{xx} and I_{yy} , are equivalent to I , which is expressed as:

$$I_{xx} = I_{yy} = I = M \frac{5L^3 + 20\sigma L^2 + 45\sigma^2 L + 32\sigma^3}{60L + 80\sigma}. \quad (5.19)$$

The hard-core potential between the sphero-cylinder and point obstacles does not generate torque along the z -axis. Consequently, the rod does not rotate around the z -axis, and it is unnecessary to consider I_{zz} . Furthermore, the non-diagonal components of the inertia tensor \mathbf{I} are zero in this frame due to the symmetrical shape of the rod. The updated velocity $\mathbf{V}(t + \Delta t_c)$ and angular velocity $\mathbf{\Omega}(t + \Delta t_c)$ after the collision are calculated using the following equations:

$$\mathbf{V}(t + \Delta t_c) = \mathbf{V}(t) + \Delta v \mathbf{n} \quad (5.20)$$

$$I\mathbf{\Omega}(t + \Delta t_c) = I\mathbf{\Omega}(t) + Ml\Delta v\mathbf{U}(t + \Delta t_c) \times \mathbf{n}, \quad (5.21)$$

Here, Δv represents the change in velocity magnitude, which is derived from the conservation of energy before and after the collision, expressed as $Mv^2(t) + I\Omega^2(t) = Mv^2(t + \Delta t_c) + I\Omega^2(t + \Delta t_c)$. The expression for Δv is:

$$\Delta v = -\frac{2I[\mathbf{V}(t) + I\mathbf{\Omega}(t) \times \mathbf{U}(t + \Delta t_c)] \cdot \mathbf{n}}{I + l^2[\mathbf{U}(t + \Delta t_c) \times \mathbf{n}]^2}. \quad (5.22)$$

After updating $\mathbf{V}(t + \Delta t_c)$ and $\mathbf{\Omega}(t + \Delta t_c)$, the next step is resampling Δt_c , i.e., restarting the process from step (i). This algorithm is repeated to compute the time series data for the rod position $\mathbf{R}(t)$, and velocities of the translational and rotational degrees of freedom, $\mathbf{V}(t)$ and $\mathbf{\Omega}(t)$.

5.B Empirical Expression for Diffusion Coefficient

An empirical fitting function for the measured D , displayed in Figure 5.4 (b), is represented by:

$$\frac{D}{\bar{V}L_e} \approx \frac{1}{2\rho\sigma L_e^2} + \frac{11\rho\sigma L_e^2}{65[11 + 2(\rho\sigma L_e^2)^2\sigma/L_e]}, \quad (5.23)$$

This function is consistent with the three scaling relations observed in Figure 5.4, namely (1) $D/\bar{V}\sigma \sim 1/\rho\sigma^2L_e$, (2) $D/\bar{V}\sigma \sim \rho L_e^3$, and (3) $D/\bar{V}\sigma \sim 1/\rho\sigma^3$ for small, intermediate, and large values of ρ , respectively. Equation (5.23) also quantitatively aligns with the KMC simulation data in Figure 5.4(b), as illustrated in Figure 5.8. According to Equation (5.23), $D/\bar{V}L_e$ exhibits a monotonic decrease with an increase in $\rho\sigma L_e^2$ for $L_e/\sigma \leq 520/11$ (aspect ratio approximately 24). For larger rod length, $D/\bar{V}L_e$ displays a local minimum and maximum as $\rho\sigma L_e^2$ increases. Furthermore, Equation (5.23) enables the estimation of two crossover densities, $\rho_{1\leftrightarrow 2} \approx 5.7 \times (\sigma L_e^2)^{-1}$ and $\rho_{2\leftrightarrow 3} \approx 2.3 \times (\sigma L_e)^{-3/2}$. These densities remain unaffected by temperature variations, while D proportionally increases with $\bar{V} = 1/\sqrt{\beta M}$, a behavior typically observed in gas diffusion [11, 127, 128] in fixed obstacle geometries.

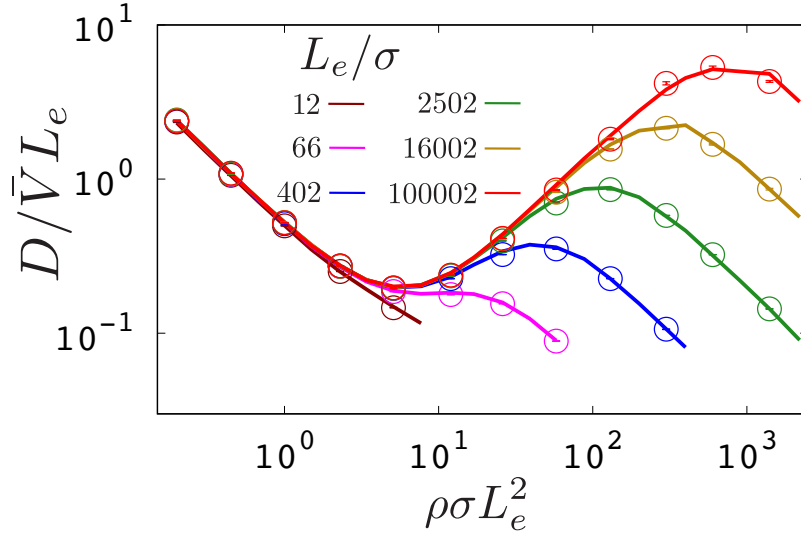


Figure 5.6: Scaled translational diffusion coefficient $D_c/\bar{V}L_e$ as a function of the scaled obstacle density $\rho\sigma L_e^2$ with the various rod length L_e , which is obtained using the KMC simulations. Symbols express the results for $\Delta t_{\max} = \sqrt{\beta I}/10$. Curves represent the data for $\Delta t_{\max} = \sqrt{\beta I}/100$, which have been displayed in Figure 5.4 in the main manuscript.

5.C Additional KMC Simulation Data

Figure 5.6 illustrates the relation between $D/u\sigma$ and $\rho\bar{V}L_e^2$, using symbols for $\Delta t_{\max} = \sqrt{\beta I}/10$ and curves for $\Delta t_{\max} = \sqrt{\beta I}/100$. The overlapping data from these two Δt_{\max} suggest that the KMC simulation results are largely independent of the magnitude of Δt_{\max} , provided it remains significantly smaller than the rotational period, specifically $\Delta t_{\max} \ll \sqrt{\beta I}$. Figure 5.7 presents the scaled rotational diffusion coefficient $D_{\text{rot}}L_e/\bar{V}$ against the scaled obstacle density $\rho\sigma L_e^2$ as derived from KMC simulations for cases where $\rho\sigma^2L_e < 1$. Here, D_{rot} is defined via the rotational relaxation time τ_{rot} , following the equation $D_{\text{rot}} = (2\tau_{\text{rot}})^{-1}$. The determination of τ_{rot} is achieved through fitting the directional correlation function $\langle \mathbf{U}(\Delta t) \cdot \mathbf{U}(0) \rangle$ using the exponential function $\exp(-t/\tau_{\text{rot}})$. This fitting procedure is limited to the data within the higher density regime, where $\rho\sigma L_e^2 > 3$. In this regime, $\langle \mathbf{U}(\Delta t) \cdot \mathbf{U}(0) \rangle$ demonstrates a monotonic decay, making it suitable for fitting with the exponential function. Conversely, in the lower density regime ($\rho\sigma L_e^2 < 3$), $\langle \mathbf{U}(\Delta t) \cdot \mathbf{U}(0) \rangle$ shows a damped oscillatory behavior, rendering it unsuitable for such fitting.

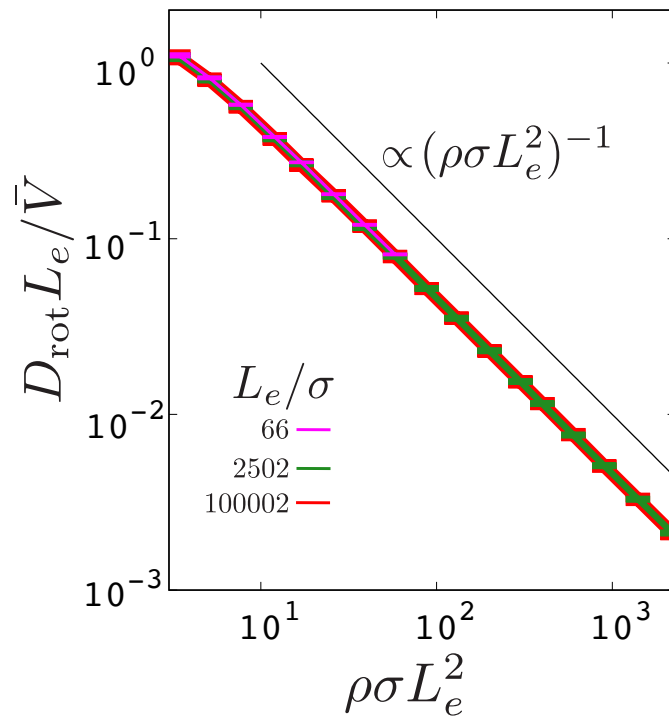


Figure 5.7: Reduced rotational diffusion coefficient $D_{\text{rot}} L_e / \bar{V}$ plotted against the scaled obstacle density $\rho \sigma L_e^2$ along with the error bars from the curve fittings, as obtained using the kinetic Monte Carlo simulations. The asymptotic exponent, expressed as $D_{\text{rot}} \sim \bar{V} / (\rho L_e^3 \sigma)$, is also displayed.

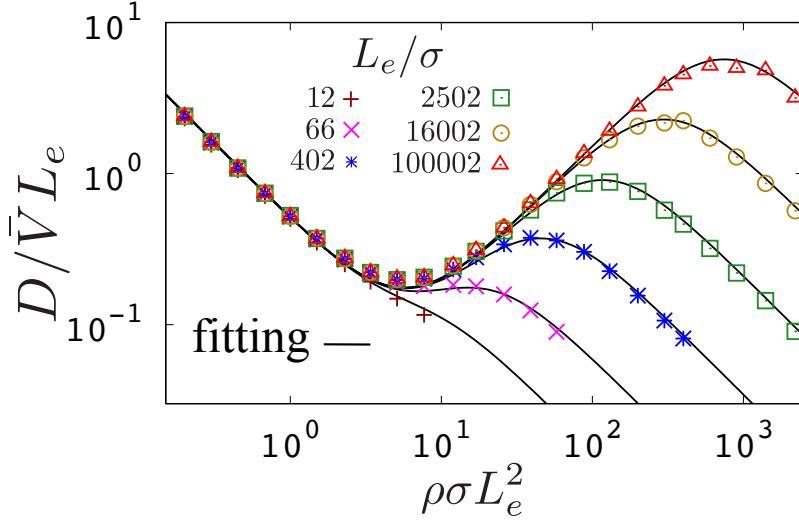


Figure 5.8: Fitting function for D as delineated by Equation (5.23) with various rod lengths L_e , depicted by black curves. For comparison, D calculated from the KMC simulation, as presented in Figure 5.4(b), are illustrated using symbols. Based on Equation (5.23), it is estimated that the upturn in D is unlikely for $L_e/\sigma \leq 520/11$.

5.D Protocol of Simulation

In the MD simulation, the system comprises a single mobile rod and, in contrast to the Kinetic Monte Carlo (KMC) method, incorporates a significant number, precisely 10^8 , of immobile point obstacles. These obstacles are placed uniformly at a number density ρ within a three-dimensional cubic box with periodic boundary conditions. The mobile rod is initially positioned in such a manner that it does not overlap with any of the obstacles. Regarding the characteristics of the mobile rod, it possesses a sphero-cylindrical shape. The radius, length along its axis, and mass of the rod are denoted by σ , L , and M , respectively, consistent with the case for the KMC simulation as in Figure 5.1. Additionally, the moment of inertia tensor of the rod is represented by \mathbf{I} (Equation (5.19)). This tensor is defined in a frame of reference where the vector $\mathbf{U} = (0, 0, 1)$ designates the z -axis. The system total energy, represented by E , includes the kinetic energy from both the translational and rotational degrees of freedom of the mobile rod, as well as the potential energy E_U arising from the interaction between the mobile rod and the fixed obstacles. This is expressed as:

$$E = \frac{M\mathbf{V}^2}{2} + \frac{\mathbf{I}\boldsymbol{\Omega}^2}{2} + E_U(\mathbf{R}, \mathbf{U}, \{\mathbf{r}_i\}), \quad (5.24)$$

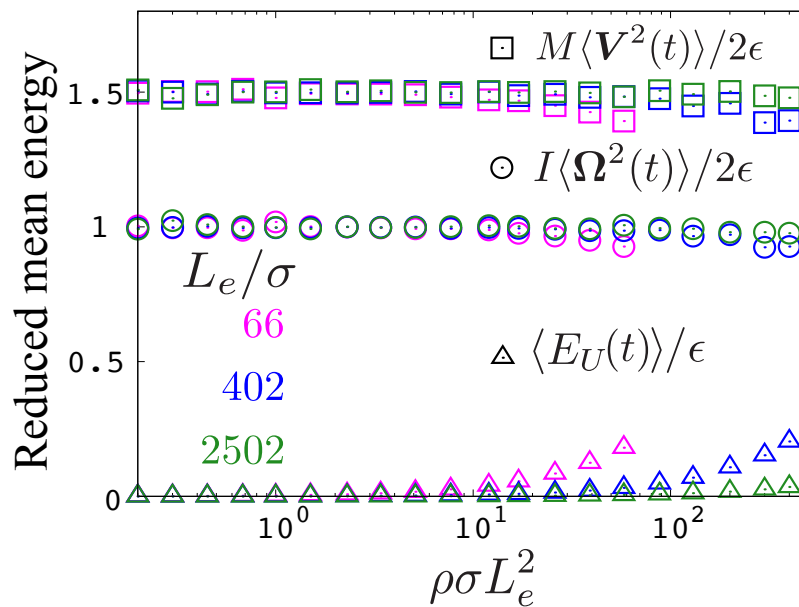


Figure 5.9: Reduced mean energies against obstacle density, calculated from the molecular dynamics (MD) simulations. Squares symbolize the data points for mean translational energy $M\langle\mathbf{V}^2(t)\rangle/2$, circles for mean rotational energy $I\langle\boldsymbol{\Omega}^2(t)\rangle/2$, and triangles for mean potential energy $\langle E_u(t)\rangle$, each normalized by ϵ . The total of these energy components remains constant throughout the simulation. Each color represents the rod length: pink for $L_e = 66 \sigma$, blue for $L_e = 402 \sigma$, and green for $L_e = 2502 \sigma$.

In this equation, I is defined as Equation (5.19). The variables \mathbf{V} and $\mathbf{\Omega}$ are the translational and angular velocities of the rod, respectively. \mathbf{R} and \mathbf{U} denote the position and direction vectors of the rod, respectively. Additionally, \mathbf{r}_i specifies the position of the i th fixed obstacle within the system. In the MD simulation, the interparticle interaction is chosen by the Weeks-Chandler-Andersen (WCA) potential working for the minimum distance from the major axis of the rod to each obstacle, denoted as $d_i = d(\mathbf{R}, \mathbf{U}, \mathbf{r}_i)$, which is formulated as:

$$E_U(\mathbf{R}, \mathbf{U}, \{\mathbf{r}_i\}) = 4\epsilon \sum_i \left[\left(\frac{\sigma}{d_i} \right)^{12} - \left(\frac{\sigma}{d_i} \right)^6 + \frac{1}{4} \right], \quad (5.25)$$

This equation applies when d_i is less than or equal to $2^{1/6}\sigma$. Here, ϵ means the unit of energy for the WCA potential. The computation of $d_i = d(\mathbf{R}, \mathbf{U}, \mathbf{r}_i)$, indicating the minimum distance from the rod major axis to the i th obstacle, is performed using Lumelsky's algorithm [129]. At the onset of the MD simulation, the initial velocities of the rod \mathbf{V} and the angular velocity $\mathbf{\Omega}$ are assigned randomly so that the combined value of the kinetic energies, $MV^2/2$ for translational and $I\Omega^2/2$ for rotational motion, equates to $5\epsilon/2$. As a result, the total energy E of the system is maintained at $5\epsilon/2$ since the system is initially constructed without any overlaps between the rod and the obstacles ($U = 0$). The dynamics of the rod within this system are computed using a modified version of the Leap-Frog algorithm, specifically extended for rod-shaped particles [51]. The simulation spans a time duration of $10^7\sigma\sqrt{M/\epsilon}$, employing a step size of $10^{-3}\sigma\sqrt{M/\epsilon}$ for each calculations. In Figure 5.5, the reduced diffusion coefficient, expressed as $D/\bar{V}L_e$, is plotted against the number density $\rho\sigma L_e^2$ for various lengths of the rod L_e . Here, V is defined as $1/\sqrt{\beta M}$, where $1/2\beta$ is the mean of the kinetic energy per degree of freedom, as determined in the MD simulation. In the MD simulation, it is noted that the rod becomes completely immobilized at sufficiently high number densities, specifically when $\rho\sigma^2 L_e$ exceeds 1, where L_e is defined as $L + 2\sigma$. This phenomenon of the rod being trapped is not the focus of this study. Therefore, the analysis is limited to a range of number densities where $\rho\sigma^2 L_e$ is less than 1, or equivalently expressed as $\rho\sigma L_e^2 \leq L_e/\sigma$.

During the MD simulations, the total energy E of the system is distributed among its translational, rotational, and potential components. In Figure 5.9, the time-averaged energies, namely $M\langle\mathbf{V}^2(t)\rangle/2$ for translational kinetic energy, $I\langle\mathbf{\Omega}^2(t)\rangle/2$ for rotational kinetic energy, and $\langle E_U(t)\rangle$ for potential energy, are represented against the scaled number density of obstacles. From these representations, it is observed that the normalized kinetic energy terms, $M\langle\mathbf{V}^2(t)\rangle/2\epsilon$ and $I\langle\mathbf{\Omega}^2(t)\rangle/2\epsilon$, become values around $3/2$ and 1 in the density range explored in the MD simulation, although there is a slight reduction in these kinetic energies as the density of obstacles increases, particularly

when approaching the threshold of the trapping density regime $\rho\sigma^2L_e \sim 1$.

Chapter 6

Conclusion

This dissertation numerically and theoretically explored the dynamics of particles immersed in simple structureless media; the static properties are always an ideal gas. The summaries of each chapter are presented as follows.

Chapter 2: Non-Gaussian Diffusion of Particle in Ideal Gas. The dynamics of a target particle introduced into an ideal gas composed of point masses were examined through numerical simulations. The target particle exhibits qualitatively different behavior against the mass of the target particle and the number density of the gas particle. When the target particle is heavy, the target particle exhibits simple ballistic and diffusive behavior in short and long timescales, respectively. Meanwhile, when the target particle is lightweight, the non-Gaussian diffusion emerges. Notably, when the gas particle is concentrated, the lightweight particle shows anomalous diffusion, even though the structure of the gas particle is always that of the ideal gas. To clarify the origin of the observed non-Gaussian anomalous diffusion, analyses focusing on the collisions between the target particle and point masses were conducted. Consequently, it was revealed that this type of diffusion originates from repeated collisions with the same gas particles.

Chapter 3: Fluctuating Diffusivity of Particle in Gas Mixtures: Numerical Study. This chapter delved into the non-Gaussian diffusion of a minor lightweight particle in binary-gas mixtures. To calculate the dynamics of the minor particle, the novel simulation scheme based on the collision statistics between a minor particle and major gas particles was constructed. The minor lightweight particle demonstrates an unusual diffusion behavior termed Brownian yet non-Gaussian diffusion. This type of diffusion is attributed to the fluctuating diffusivity. The origin of

the observed fluctuating diffusivity in the gas mixture was identified as the timescale separation between the velocity direction and speed of the minor particle.

Chapter 4: Fluctuating Diffusivity of Particle in Gas Mixtures: Theoretical Study. To reproduce the Brownian yet non-Gaussian diffusion in the binary-gas mixture, theoretical analyses based on the Lorentz gas model were conducted. Specifically, the dynamics of a minor lightweight particle in heavy gas particles are assumed to be that in the Lorentz gas model at a short time scale where only a few collisions occur. The mean square displacement and non-Gaussian parameter in the Lorentz gas model are analytically calculated, and they do not show the Brownian yet non-Gaussian diffusion. To incorporate the effect that the minor particle speed takes various magnitudes, the canonical ensemble averages for the mean square displacement and non-Gaussian parameter were calculated. The averaged result successfully reproduces the Brownian yet non-Gaussian diffusion of a minor lightweight particle in the binary-gas mixture.

Chapter 5: Increase in Diffusivity of Rod in Obstacles. This chapter numerically examined the dynamics of a rod-shaped particle moving through the fixed point obstacles in three-dimensional space under the Markovian process. To calculate the dynamics of the rod, the stochastic simulation based on the collision statistics between the rod and obstacles was constructed. It was found that the diffusion coefficient of the rod decreases, increases, and decreases again with increasing the obstacle density when the rod is sufficiently long. The power exponent in each regime can be simply explained based on the timescales of the angular velocity and collision frequency of the rod.

In conclusion, this dissertation revealed that the particle exhibits intriguing diffusion when the particle is lightweight or elongated, even in simple structureless media; the particle can exhibit anomalous non-Gaussian diffusion, Brownian yet non-Gaussian diffusion, and an increase in diffusivity. Thanks to the simple nature of the studied systems, the observed dynamics were elucidated based on the collisions between the target and media particles. The findings can be achieved by the investigations in the simple structureless media. However, elucidated mechanisms potentially hold for more complex media since they are not restricted to structureless media. The findings in this dissertation may provide fresh insight into the studies for diffusion phenomena of a particle diffusing in diverse, complex media.

Acknowledgements

主査の畝山多加志先生に心より感謝申し上げます。畝山先生は筆者の指導教員であり、大学4年時から研究をご指導頂きました。博士論文の2章、3章、4章に対応する、学位取得に用いた論文 [1-3] は畝山先生のご指導の下実施した研究です。畝山先生は、毎日学生居室に足を運んで下さり、研究議論だけでなく研究の考え方も懇切にご教示下さいました。特に、「良く分からないものでよく分からないものを測っても何も分からん」というお言葉が強く印象に残っております。このお言葉が、筆者が博士論文において単純な系を研究した強い動機になっております。畝山先生のご指導のおかげで、研究者として成長することができました。今後筆者は実験研究に取り組み、畝山先生のような理論、実験、シミュレーションの何れにも精通する研究者を目指します。

副査の増渕雄一先生に心より感謝致します。増渕先生は、私が所属する研究室の主宰であり、研究生活全般や研究者としての考え方に関して親身にご指導下さいました。増渕先生自身が手を動かして迅速に主著論文を執筆する姿に、心より尊敬の念を抱いております。増渕先生に論文執筆に関するコツを尋ねた際に、あるアドバイスを頂いたことがありました。頂いた助言により、執筆作業に対する抵抗感が大きく軽減して、筆者は博士前期/後期課程で6本の主著論文（+1本投稿中）を出版できました。増渕先生のような面に関するご指導のおかげで、研究者として自信を持つことができました。増渕先生のように筆者も自身で手を動かして論文を書く研究者であり続けようと思います。

副査を担当して頂いた武藤俊介先生に感謝申し上げます。武藤先生には、筆者の研究内容のプレゼンテーションをご覧頂いて、多数のアドバイスを頂きました。特に、博士論文全体の導入部分と棒状粒子の章の導入部分及び論理に関して非常に有用なコメントを頂き、論文の論理構成を強化することができました。

副査を務めて頂いた宮崎州正先生に心より感謝申し上げます。宮崎先生とは、博士論文の審査だけでなく学会でも度々お会いして、筆者の研究に関する貴重なコメントを頂いておりました。頂いたコメントは、博士後期課程の研究の方向性を見直す大きなきっかけになりました。第5章の棒状粒子の研究は、宮崎先生がご執筆された”ガラス転移とモード結合理論: 最近の発展と課題”にある無限に細い棒の系に関する記述に触発されて実施したものです。棒の運動論に関する研究

は海外の研究者と共同研究をするきっかけにもなりました。このような貴重な機会をご提供下さった宮崎先生に大変感謝致します。

副査をご担当頂いた芳松克則先生に感謝致します。芳松先生には、博士論文と研究内容のプレゼンテーションをご覧頂いて、表現方法に関して詳細なアドバイスを頂きました。併せて、流体分野や物性分野の研究者の視点をご提供下さり、博士論文本体及び審査会の発表内容の構成を磨き上げることができました。

Martin Kröger 先生 (ETH Zrich) に感謝申し上げます。筆者は Martin 先生のご指導の下、スイスのチューリッヒで5ヶ月間研究を実施しました。Martin 先生の部屋は筆者が滞在していた部屋の隣にあり、研究に関する議論を密に交わして頂きました。研究以外にも、スイスの Walensee 湖を囲む雪山へ遠足に連れて行って貰ったり、クリスマスマーケットの飲み会にお誘い頂いたり、とても楽しい思い出を作ることができました。学位取得に用いた論文 [4] については Martin 先生からご指導を賜りました。貴重な機会を提供頂いたことに重ねて感謝申し上げます。

土肥侑也先生に感謝致します。土肥先生は筆者が所属する研究室の助教であり、博士前期過程から研究の議論を頂いておりました。特に、実験サイドからの視座をご提供下さり、論文の議論を深めることができました。併せて、研究生活全般の懇切なご指導も頂き、大変お世話になりました。

石田崇人先生に感謝申し上げます。石田先生は、筆者が所属する研究室に学術振興会特別研究員 PD として在籍しており、研究内容や方向性に関して度々議論を頂いておりました。本博士論文5章の棒粒子の拡散性増加がマルコフ過程でも生じることの発見は石田先生との議論が発端でした。建築科学を背景に持つ石田さんとは、博士後期課程のメインの研究とは異なる建築材料に関する共同研究 [130] を実施しています。議論の度に建築分野の新鮮な視座をご提供頂いて、筆者の研究意義や方向性について深く考えることができました。貴重な機会をご提供下さった石田先生に心より感謝致します。

早川尚男先生に心より感謝致します。早川先生には、京都大学基礎物理学研究所の談話会にご招待頂き、研究内容について議論を頂きました。特に、3章の二成分気体の揺らぐ拡散性に関して、Boltzmann 方程式に基づいて計算する方針をご教示頂きました。当該の計算は筆者の技術が足りずまだ達成できておりません。引き続き取り組んでいく所存でございます。

桂木洋光先生に感謝申し上げます。桂木先生には、セミナーにご招待頂き研究内容の議論を頂きました。特に、筆者の粒子拡散に関する研究と粉体系との関係について議論を頂き、実験サイドの視点から貴重なアドバイスを頂きました。

広井紀彦さん、福永紘平さん、大石達磨さん、榎本圭吾さんには、研究結果の解釈や解析のアイデアを度々議論して頂きました。加えて、福永さん、大石さん、榎本さんとは、The Theory of Simple Liquids [29] を輪読して統計力学の理解を深めました。

秘書の赤木静様，以前研究室に在籍していらっしゃった山本哲也先生，瀬戸亮平先生，木田拓充先生，先輩の Lixin Yang さん，夏目享治さん，久世雅大さん，嶋田耕太郎さん，草田慧さん，井上夏さん，佐々木弘至さん，後藤一真さん，久米健太さん，同期の広井紀彦さん，木津悠さん，斉藤麻亜久さん，後輩の河井俊也さん，福永紘平さん，榎本裕太さん，山本直弥さん，大石達磨さん，榎本圭吾さん，白石達也さん，北村仁哉さん，安井翔一さん，磯田龍矢さん，市川千陽さん，鈴木海渡さん，山脇悠矢さん，山崎良平さん，神谷恭汰さん，綾口修八さん，重倉健人さん，庄田琢也さん，冨田京武さん，山上隼平さん，油野瑞貴さん，櫛田浩資さん，柴田聖菜さん，晴 椏和也さん，福田悠司さんのおかげで毎日楽しく研究室生活を過ごすことができました。増淵研究室の皆様に心より感謝申し上げます。

最後に，筆者が研究に専念できるよう応援して下さった祖母，両親，兄，妹，婚約者の千明さんご家族に心から感謝を申し上げます。

References

- [1] F. Nakai, Y. Masubuchi, and T. Uneyama. Short-time dynamics of a tracer in an ideal gas. *Phys. Rev. E*, 102:032104, 2020.
- [2] F. Nakai, Y. Masubuchi, Y. Doi, T. Ishida, and T. Uneyama. Fluctuating diffusivity emerges even in binary gas mixtures. *Phys. Rev. E*, 107(1):014605, 2023.
- [3] F. Nakai and T. Uneyama. Brownian yet non-gaussian diffusion of a light particle in heavy gas: Lorentz gas based analysis. *Phys. Rev. E*, 108(4):044129, 2023.
- [4] F. Nakai, M. Kröger, T. Ishida, T. Uneyama, Y. Doi, and Y. Masubuchi. Increase in rod diffusivity emerges even in markovian nature. *Phys. Rev. E*, 107(4):044604, 2023.
- [5] R. Brown. XXVII. A brief account of microscopical observations made in the months of june, july and august 1827, on the particles contained in the pollen of plants; and on the general existence of active molecules in organic and inorganic bodies. *Philos. Mag.*, 4(21):161, 1828.
- [6] A. Einstein. On the movement of small particles suspended in stationary liquids required by the molecular-kinetic theory of heat. *Ann. Phys.*, 17:549, 1905.
- [7] A. Einstein. *Investigations on the Theory of the Brownian Movement*. Courier Corporation, 1956.
- [8] J. Perrin. *Brownian movement and molecular reality*. Taylor and Francis, London, 1910.
- [9] S. Chapman and T. G. Cowling. *The Mathematical Theory of Non-uniform Gases: an Account of the Kinetic Theory of Viscosity, Thermal Conduction and Diffusion in Gases*. Cambridge University Press, 3rd edition, 1990.
- [10] J. Jeans. *The Dynamical Theory of Gases*. Cambridge University Press, 1904.

- [11] J. R. Dorfman, H. van Beijeren, and T. R. Kirkpatrick. *Contemporary kinetic theory of matter*. Cambridge University Press, 2021.
- [12] J. A. McLennan. *Introduction to nonequilibrium statistical mechanics*. Prentice Hall, 1989.
- [13] M. Doi and S. F. Edwards. *The theory of polymer dynamics*, volume 73. Oxford University Press, 1988.
- [14] R. G. Larson. *The structure and rheology of complex fluids*. Oxford University Press, 1999.
- [15] M. Doi. *Soft Matter Physics*. Oxford University Press, 2013.
- [16] P.-G. De Gennes and J. Prost. *The physics of liquid crystals*. Number 83. Oxford University Press, 1993.
- [17] W. Kob, C. Donati, S. J. Plimpton, P. H. Poole, and S. C. Glotzer. Dynamical heterogeneities in a supercooled lennard-jones liquid. *Phys. Rev. Lett.*, 79(15):2827, 1997.
- [18] B. Wang, S. M. Anthony, S. C. Bae, and S. Granick. Anomalous yet brownian. *Proc. Nat. Acad. Sci.*, 106(36):15160, 2009.
- [19] H. Mori. Transport, collective motion, and brownian motion. *Prog. Theor. Phys.*, 33(3):423, 1965.
- [20] G. E. Uhlenbeck and L. S. Ornstein. On the theory of the brownian motion. *Phys. Rev.*, 36(5):823, 1930.
- [21] L. S. Ornstein. On the theory of the brownian motion. *Phys. Rev.*, 36:823, 1930.
- [22] T. Ge, G. S. Grest, and M. Rubinstein. Nanorheology of entangled polymer melts. *Physical review letters*, 120(5):057801, 2018.
- [23] P. Chaudhuri, L. Berthier, and W. Kob. Universal nature of particle displacements close to glass and jamming transitions. *Phys. Rev. Lett.*, 99(6):060604, 2007.
- [24] T. Uneyama, T. Miyaguchi, and T. Akimoto. Fluctuation analysis of time-averaged mean-square displacement for the langevin equation with time-dependent and fluctuating diffusivity. *Phys. Rev. E*, 92(3):032140, 2015.

- [25] T. Miyaguchi. Elucidating fluctuating diffusivity in center-of-mass motion of polymer models with time-averaged mean-square-displacement tensor. *Phys. Rev. E*, 96(4):042501, 2017.
- [26] W. He, H. Song, Y. Su, L. Geng, B. J. Ackerson, H. B. Peng, and P. Tong. Dynamic heterogeneity and non-gaussian statistics for acetylcholine receptors on live cell membrane. *Nat. Commun.*, 7(1):1, 2016.
- [27] J.-H. Jeon, M. Javanainen, H. Martinez-Seara, R. Metzler, and I. Vattulainen. Protein crowding in lipid bilayers gives rise to non-gaussian anomalous lateral diffusion of phospholipids and proteins. *Phys. Rev. X*, 6(2):021006, 2016.
- [28] D. J. Evans and G. P. Morriss. *Statistical mechanics of nonequilibrium liquids*. Cambridge University Press, 2nd edition, 2008.
- [29] J.-P. Hansen and I. R. McDonald. *Theory of Simple Liquids: with Applications to Soft Matter*. Academic Press., 4th edition, 2013.
- [30] N. N. Bogoliubov. Problems of a dynamical theory in statistical physics. *Studies in statistical mechanics*, 1, 1960.
- [31] M. Born and H. S. Green. *A general kinetic theory of liquids*. CUP Archive, 1949.
- [32] J. G. Kirkwood. The statistical mechanical theory of transport processes i. general theory. *J. Chem. Phys.*, 14(3):180, 1946.
- [33] K. Miyazaki and D. R. Reichman. Mode-coupling theory and the fluctuation–dissipation theorem for nonlinear langevin equations with multiplicative noise. *J. Phys. A Math. Theor.*, 38(20):L343, 2005.
- [34] D. Frenkel and J. F. Maguire. Molecular dynamics study of infinitely thin hard rods: scaling behavior of transport properties. *Phys. Rev. Lett.*, 47(15):1025, 1981.
- [35] D Frenkel and J. F. Maguire. Molecular dynamics study of the dynamical properties of an assembly of infinitely thin hard rods. *Mol. Phys.*, 49(3):503, 1983.
- [36] R. Zwanzig. Nonlinear generalized langevin equations. *Journal of Statistical Physics*, 9(3):215, 1973.

- [37] K. Kawasaki. Simple derivations of generalized linear and nonlinear langevin equations. *J. Phys. A Math. Theor.*, 6(9):1289, 1973.
- [38] R. F. Fox. Gaussian stochastic processes in physics. *Phys. Rep.*, 48(3):179, 1978.
- [39] R. F. Fox. The generalized langevin equation with gaussian fluctuations. *J. Math. Phys.*, 18(12):2331, 1977.
- [40] T. G. Mason and D. A. Weitz. Optical measurements of frequency-dependent linear viscoelastic moduli of complex fluids. *Phys. Rev. Lett.*, 74(7):1250, 1995.
- [41] J. Guan, B. Wang, and S. Granick. Even hard-sphere colloidal suspensions display fickian yet non-gaussian diffusion. *ACS nano*, 8(4):3331, 2014.
- [42] T. Miyaguchi, T. Akimoto, and E. Yamamoto. Langevin equation with fluctuating diffusivity: A two-state model. *Phys. Rev. E*, 94(1):012109, 2016.
- [43] F. Höfling, E. Frey, and T. Franosch. *Phys. Rev. Lett.*, 101(12):120605, 2008.
- [44] D. R. Reichman and P. Charbonneau. Mode-coupling theory. *J. Stat. Mech. Theory Exp.*, 2005(05):P05013, 2005.
- [45] L. Boltzmann. *Lectures on gas theory*. University of California Press, 2023.
- [46] W. Götze. Recent tests of the mode-coupling theory for glassy dynamics. *J. Condens. Matter Phys.*, 11(10A):A1, 1999.
- [47] T. Gaskell and S. Miller. Longitudinal modes, transverse modes and velocity correlations in liquids. i. *J. Phys. C: Solid State Phys.*, 11(18):3749, 1978.
- [48] L. Onsager. The effects of shape on the interaction of colloidal particles. *Ann. N. Y. Acad. Sci.*, 51(4):627, 1949.
- [49] D. Frenkel. Computer simulation of hard-core models for liquid crystals. *Mol. Phys.*, 60(1):1, 1987.
- [50] D. Frenkel. Statistical mechanics of liquid crystals. *les Houches*, page 689, 1991.
- [51] M. P. Allen and M. R Wilson. *Journal of computer-aided molecular design*, 3:335, 1989.

- [52] H. Löwen. Anisotropic self-diffusion in colloidal nematic phases. *Phys. Rev. E*, 59(2):1989, 1999.
- [53] M. P. Allen. Diffusion coefficient increases with density in hard ellipsoid liquid crystals. *Phys. Rev. Lett.*, 65(23):2881, 1990.
- [54] K. Kremer and G. S. Grest. Dynamics of entangled linear polymer melts: A molecular-dynamics simulation. *J. Chem. Phys.*, 92(8):5057, 1990.
- [55] A. E. Likhtman, S. K. Sukumaran, and J. Ramirez. Linear viscoelasticity from molecular dynamics simulation of entangled polymers. *Macromolecules*, 40(18):6748, 2007.
- [56] V. A. Harmandaris, V. G. Mavrantzas, D. N. Theodorou, M. Kröger, J. Ramirez, H. C. Öttinger, and D. Vlassopoulos. Crossover from the rouse to the entangled polymer melt regime: signals from long, detailed atomistic molecular dynamics simulations, supported by rheological experiments. *Macromolecules*, 36(4):1376, 2003.
- [57] M. Doi and S. F. Edwards. Dynamics of rod-like macromolecules in concentrated solution. part 1. *J. Chem. Soc., Faraday trans. II*, 74:560, 1978.
- [58] M. Doi and S. F. Edwards. Dynamics of concentrated polymer systems. part 2.—molecular motion under flow. *J. Chem. Soc., Faraday trans. II*, 74:1802, 1978.
- [59] P.-G. De Gennes. Reptation of a polymer chain in the presence of fixed obstacles. *J. Chem. Phys.*, 55(2):572, 1971.
- [60] P. E. Rouse Jr. A theory of the linear viscoelastic properties of dilute solutions of coiling polymers. *J. Chem. Phys.*, 21(7):1272, 1953.
- [61] P. G. De Gennes. Dynamics of entangled polymer solutions. i. the rouse model. *Macromolecules*, 9(4):587, 1976.
- [62] A. Ortega and J. G. de la Torre. Hydrodynamic properties of rodlike and disklike particles in dilute solution. *J. Chem. Phys.*, 119(18):9914, 2003.
- [63] R. K. Murarka, S. Bhattacharyya, and B. Bagchi. Diffusion of small light particles in a solvent of large massive molecules. *J. Chem. Phys.*, 117(23):10730, 2002.

- [64] W. Fenz, I. M. Mryglod, O. Prytula, and R. Folk. Concentration and mass dependence of transport coefficients and correlation functions in binary mixtures with high mass asymmetry. *Phys. Rev. E*, 80(2):021202, 2009.
- [65] S. Acharya, U. K. Nandi, and S. M. Bhattacharyya. Fickian yet non-gaussian behaviour: A dominant role of the intermittent dynamics. *J. Chem. Phys.*, 146(13):134504, 2017.
- [66] W. van Ketel, C. Das, and D. Frenkel. Structural arrest in an ideal gas. *Phys. Rev. Lett.*, 94(13):135703, 2005.
- [67] A. K. Tucker and R. Hernandez. Observation of a trapping transition in the diffusion of a thick needle through fixed point scatterers. *J. Phys. Chem. A*, 114(36):9628, 2010.
- [68] F. Höfling and T. Franosch. Crossover in the slow decay of dynamic correlations in the lorentz model. *Phys. Rev. Lett.*, 98(14):140601, 2007.
- [69] F. Höfling, T. Franosch, and E. Frey. Localization transition of the three-dimensional lorentz model and continuum percolation. *Phys. Rev. Lett.*, 96(16):165901, 2006.
- [70] W. Götze, E. Leutheusser, and S. Yip. Diffusion and localization in the two-dimensional lorentz model. *Phys. Rev. A*, 25(1):533, 1982.
- [71] J. Machta and R. Zwanzig. Diffusion in a periodic lorentz gas. *Phys. Rev. Lett.*, 50(25):1959, 1983.
- [72] D. W. Jepsen. Dynamics of a simple many-body system of hard rods. *J. Math. Phys.*, 6(3):405, 1965.
- [73] J. L. Lebowitz, J. K. Percus, and J. Sykes. Time evolution of the total distribution function of a one-dimensional system of hard rods. *Phys. Rev.*, 171(1):224, 1968.
- [74] J. L. Lebowitz and J. K. Percus. Kinetic equations and density expansions: Exactly solvable one-dimensional system. *Phys. Rev.*, 155(1):122, 1967.
- [75] T. E. Harris. Diffusion with “collisions” between particles. *J. Appl. Probab.*, 2(2):323, 1965.
- [76] B. J. Alder and T. E. Wainwright. Studies in molecular dynamics. I. General method. *J. Chem. Phys.*, 31(2):459, 1959.

- [77] T. Einwohner and B. J. Alder. Molecular dynamics. vi. free - path distributions and collision rates for hard - sphere and square - well molecules. *J. Chem. Phys.*, 49(4):1458, 1968.
- [78] B. J. Alder, D. M. Gass, and T. E. Wainwright. Studies in molecular dynamics. viii. the transport coefficients for a hard-sphere fluid. *J. Chem. Phys.*, 53(10):3813, 1970.
- [79] B. J. Alder, W. E. Alley, and J. H. Dymond. Studies in molecular dynamics. xiv. mass and size dependence of the binary diffusion coefficient. *J. Chem. Phys.*, 61(4):1415, 1974.
- [80] B. J. Alder and W. E. Alley. Long-time correlation effects on displacement distributions. *J. Stat. Phys.*, 19:341, 1978.
- [81] B. J. Alder and W. E. Alley. Decay of correlations in the lorentz gas. *Physica A*, 121(3):523, 1983.
- [82] B. J. Alder and T. E. Wainwright. Velocity autocorrelations for hard spheres. *Phys. Rev. Lett.*, 18(23):988, 1967.
- [83] K. Kawasaki. Long time behavior of the velocity autocorrelation function. *Phys. Lett. A*, 32(6):379, 1970.
- [84] D. Montgomery. Brownian motion from boltzmann's equation. *Phys. Fluids*, 14(10):2088, 1971.
- [85] F. Rusciano, R. Pastore, and F. Greco. Fickian non-gaussian diffusion in glass-forming liquids. *Phys. Rev. Lett.*, 128(16):168001, 2022.
- [86] Y. Meroz A. Taloni and A. Huerta. Collisional statistics and dynamics of two-dimensional hard-disk systems: From fluid to solid. *Phys. Rev. E*, 92(2):022131, 2015.
- [87] P. T. Herman and B. J. Alder. Studies in molecular dynamics. xi. correlation functions of a hard-sphere test particle. *J. Chem. Phys.*, 56(2):987, 1972.
- [88] T. Yamaguchi and Y. Kimura. Non-gaussian dynamics of a dilute hard-sphere gas. *The Journal of Chemical Physics*, 114(7):3029, 2001.
- [89] Aneesur Rahman. Correlations in the motion of atoms in liquid argon. *Physical review*, 136(2A):A405, 1964.

- [90] R. Pastore, A. Ciarlo, G. Pesce, F. Greco, and A. Sasso. Rapid fickian yet non-gaussian diffusion after subdiffusion. *Phys. Rev. Lett.*, 126(15):158003, 2021.
- [91] J. Kim, C. Kim, and B. J. Sung. Simulation study of seemingly fickian but heterogeneous dynamics of two dimensional colloids. *Phys Rev. Lett.*, 110(4):047801, 2013.
- [92] K. C. Leptos, J. S. Guasto, J. P. Gollub, A. I. Pesci, and R. E. Goldstein. Dynamics of enhanced tracer diffusion in suspensions of swimming eukaryotic microorganisms. *Phys. Rev. Lett.*, 103(19):198103, 2009.
- [93] H. Kurtuldu, J. S. Guasto, K. A. Johnson, and J. P. Gollub. Enhancement of biomixing by swimming algal cells in two-dimensional films. *Proc. Nat. Acad. Sci.*, 108(26):10391, 2011.
- [94] A. V. Chechkin, F. Seno, R. Metzler, and I. M. Sokolov. Brownian yet non-gaussian diffusion: from superstatistics to subordination of diffusing diffusivities. *Phys. Rev. X*, 7(2):021002, 2017.
- [95] M. V. Chubynsky and G. W. Slater. Diffusing diffusivity: a model for anomalous, yet brownian, diffusion. *Phys. Rev. Lett.*, 113(9):098302, 2014.
- [96] T. Uneyama, T. Miyaguchi, and T. Akimoto. Relaxation functions of the ornstein-uhlenbeck process with fluctuating diffusivity. *Phys. Rev. E*, 99(3):032127, 2019.
- [97] D. T. Gillespie. A general method for numerically simulating the stochastic time evolution of coupled chemical reactions. *J. Comput. Phys.*, 22(4):403, 1976.
- [98] A. B. Bortz, M. H. Kalos, and J. L. Lebowitz. A new algorithm for monte carlo simulation of ising spin systems. *J. Comput. Phys.*, 17(1):10, 1975.
- [99] A. Chatterjee and D. G. Vlachos. An overview of spatial microscopic and accelerated kinetic monte carlo methods. *J. Comp.-Aided Mater. Design*, 14:253, 2007.
- [100] H. A. Lorentz. The motion of electrons in metallic bodies i. *Proc. K. Ned. Akad. Wet.*, 7:438, 1905.
- [101] E. J. Saltzman and K. S. Schweizer. Large-amplitude jumps and non-gaussian dynamics in highly concentrated hard sphere fluids. *Phys. Rev. E*, 77(5):051504, 2008.

- [102] R. Yamamoto and A. Onuki. Heterogeneous diffusion in highly supercooled liquids. *Phys. Rev. Lett.*, 81(22):4915, 1998.
- [103] K. Andersen and K. E. Shuler. On the relaxation of the hard—sphere rayleigh and lorentz gas. *J. Chem. Phys.*, 40(3):633, 1964.
- [104] C. Boldrighini, L. A. Bunimovich, and Y. G. Sinai. On the boltzmann equation for the lorentz gas. *J. Stat. Phys.*, 32(3):477, 1983.
- [105] B. Moran, W. G. Hoover, and S. Bestiale. Diffusion in a periodic lorentz gas. *J. Stat. Phys.*, 48(3):709, 1987.
- [106] W. Hirst and G. E. Harrison. The diffusion of radon gas mixtures. *Proc. Math. Phys. Eng. Sci.*, 169(939):573, 1939.
- [107] Gene F. M. *Nonequilibrium Statistical Mechanics*. John Wiley & Sons inc, 2008.
- [108] J. M. Miotto, S. Pigolotti, A. V. Chechkin, and S. Roldán-Vargas. Length scales in brownian yet non-gaussian dynamics. *Phys. Rev. X*, 11(3):031002, 2021.
- [109] A. Alexandre, M. Lavaud, N. Fares, E. Millan, Y. Louyer, T. Salez, Y. Amarouchene, T. Guérin, and D. S. Dean. Non-gaussian diffusion near surfaces. *Phys. Rev. Lett.*, 130(7):077101, 2023.
- [110] J. L. Lebowitz and H. Spohn. Transport properties of the lorentz gas: Fourier’s law. *J. Stat. Phys.*, 19(6):633, 1978.
- [111] R. Klages, S. S. G. Gallegos, J. Solanpää, M. Sarvilahti, and E. Räsänen. Normal and anomalous diffusion in soft lorentz gases. *Phys. Rev. Lett.*, 122(6):064102, 2019.
- [112] M. Zeitz, K. Wolff, and H. Stark. Active brownian particles moving in a random lorentz gas. *Eur. Phys. J. E*, 40:1, 2017.
- [113] C. Bruin. A computer experiment on diffusion in the lorentz gas. *Physica*, 72(2):261, 1974.
- [114] S. Leitmann and T. Franosch. Time-dependent fluctuations and superdiffusivity in the driven lattice lorentz gas. *Phys. Rev. Lett.*, 118(1):018001, 2017.
- [115] D. R. Cox and V. Isham. *Point processes*. CRC Press, 1980.

- [116] A. V. Chechkin, F. Seno, R. Metzler, and I. M. Sokolov. Brownian yet non-gaussian diffusion: From superstatistics to subordination of diffusing diffusivities. *Phys. Rev. X*, 7(2):021002, 2017.
- [117] M. Pagitsas, J. T. Hynes, and R. Kapral. Kinetic energy relaxation of a test particle in a dense fluid. *J. Chem. Phys.*, 71(11):4492, 1979.
- [118] J. J. Magda, H. T. Davis, and M. Tirrell. The transport properties of rod-like particles via molecular dynamics. i. bulk fluid. *J. Chem. Phys.*, 85(11):6674, 1986.
- [119] J. J. Magda, M. Tirrell, and H. T. Davis. The transport properties of rod-like particles. ii. narrow slit pore. *J. Chem. Phys.*, 88(2):1207, 1988.
- [120] S. Mandal, C. Kurzthaler, T. Franosch, and H. Löwen. Crowding-enhanced diffusion: An exact theory for highly entangled self-propelled stiff filaments. *Phys. Rev. Lett.*, 125(13):138002, 2020.
- [121] L. Pournin, M. Weber, M. Tsukahara, J.-A. Ferrez, M. Ramaioli, and T. M. Liebling. Three-dimensional distinct element simulation of spherocylinder crystallization. *Granul. Matter*, 7(2):119, 2005.
- [122] L. Devroye. *Non-Uniform Random Variate Generation*. Springer, New York, 1986.
- [123] J. D. Weeks, D. Chandler, and H. C. Andersen. Role of repulsive forces in determining the equilibrium structure of simple liquids. *J. Chem. Phys.*, 54(12):5237, 1971.
- [124] A. K. Tucker and R. Hernandez. Absence of enhanced diffusion in the dynamics of a thick needle through three-dimensional fixed spherical scatterers. *J. Phys. Chem. B*, 115(15):4412, 2011.
- [125] M. Otto, T. Aspelmeier, and A. Zippelius. Microscopic dynamics of thin hard rods. *J. Chem. Phys.*, 124(15):154907, 2006.
- [126] K. A. Rose, N. Gogotsi, J. H. Galarraga, J. A. Burdick, C. B. Murray, D. Lee, and R. J. Composto. Shape anisotropy enhances nanoparticle dynamics in nearly homogeneous hydrogels. *Macromolecules*, 2022.
- [127] J. J. Erpenbeck and W. W. Wood. Self-diffusion coefficient for the hard-sphere fluid. *Phys. Rev. A*, 43(8):4254, 1991.

- [128] J. H. Dymond. Hard-sphere theories of transport properties. *Chem. Soc. Rev.*, 14(3):317, 1985.
- [129] V. J. Lumelsky. On fast computation of distance between line segments. *Inf. Process. Lett.*, 21(2):55, 1985.
- [130] F. Nakai and T. Ishida. Gas diffusion in cement pastes: An analysis using a fluctuating diffusivity model. *Constr. Build. Mater.*, 407(1):133411, 2023.